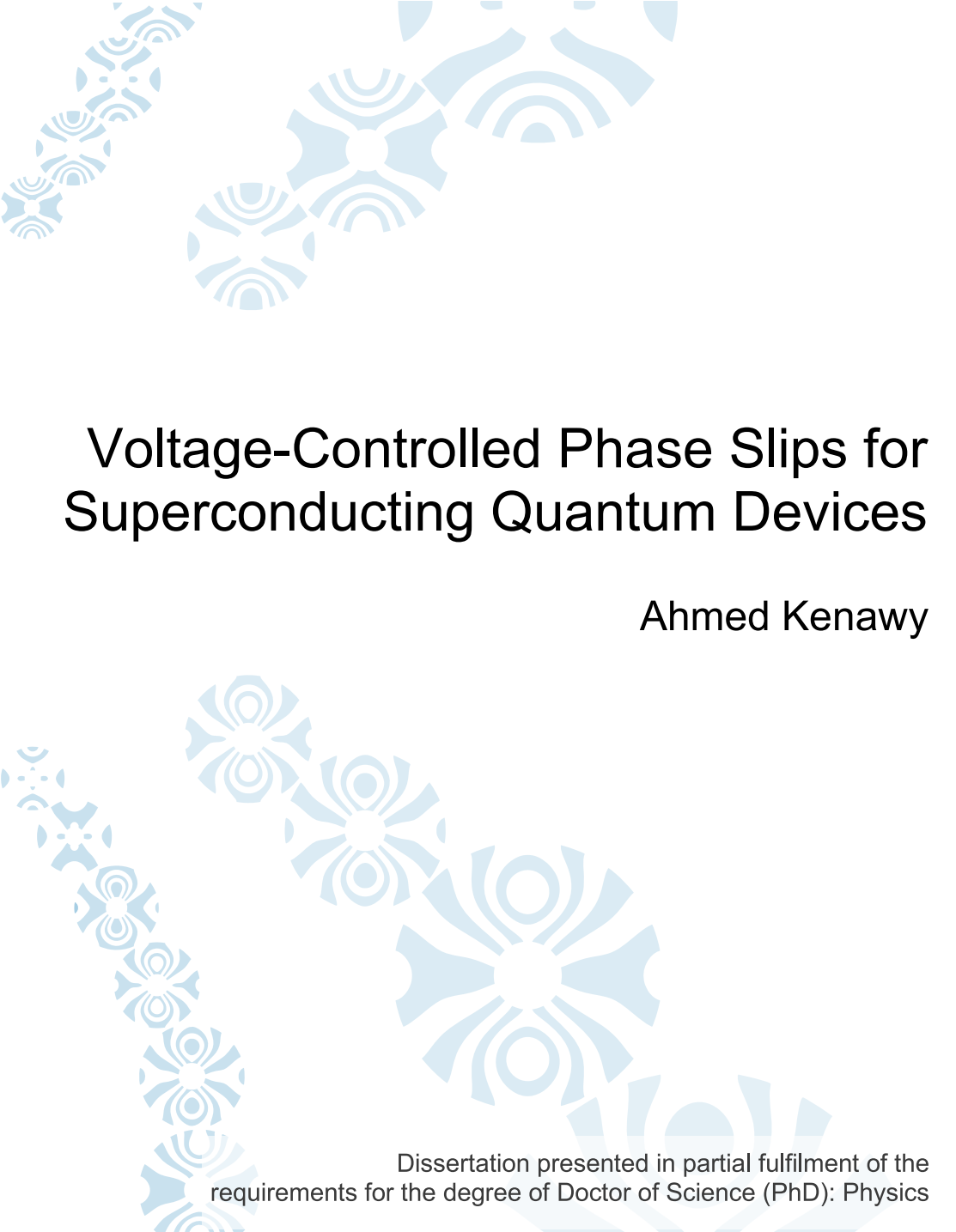


Voltage-Controlled Phase Slips for Superconducting Quantum Devices

Ahmed Kenawy



Dissertation presented in partial fulfilment of the
requirements for the degree of Doctor of Science (PhD): Physics

Voltage-Controlled Phase Slips for Superconducting Quantum Devices

Ahmed Kenawy

Promoters:

Prof. dr. Christian Maes

Prof. dr. ir. Bart Sorée

Jury:

Prof. dr. Enrico Carlon

Prof. dr. Christian Maes

Prof. dr. ir. Bart Sorée

Prof. dr. Wim Magnus

Prof. dr. Milorad Milošević

Prof. dr. Joris Van de Vondel

Prof. dr. ir. Jo De Boeck

Prof. dr. Francesco Giazotto

Dissertation presented in partial fulfillment of the requirements for the degree of Doctor of Science (PhD): Physics

©2021 KU Leuven – Faculty of Science

Uitgegeven in eigen beheer, Ahmed Kenawy, Celestijnenlaan 200D, B-3001 Leuven (Belgium)

Alle rechten voorbehouden. Niets uit deze uitgave mag worden vermenigvuldigd en/of openbaar gemaakt worden door middel van druk, fotokopie, microfilm, elektronisch of op welke andere wijze ook zonder voorafgaande schriftelijke toestemming van de uitgever.

All rights reserved. No part of the publication may be reproduced in any form by print, photoprint, microfilm, electronic or any other means without written permission from the publisher.

Acknowledgments

Part of the journey is the end. And, throughout this journey, I have received a great deal of help, support, and guidance that cannot go unacknowledged.

I would like to express my gratitude to my supervisor Dr. Bart Sorée for his mentorship during this four-year journey. I was always inspired by our daily conversations. His expertise and constructive feedback were indispensable to my research and he truly helped me become an independent researcher.

I am grateful to my supervisor Dr. Wim Magnus. His critical eye and scientific rigor were essential to my PhD journey. His door was always open for my naive questions. Even after retirement, he supported my research through the end of my PhD. I did, however, miss our coffee breaks along with Bart and Joren Vanherck in imec 4. They did make the paint seem less gray.

I am indebted to my supervisor Dr. Milorad Milošević for helping me over the past two years. I believe the completion of this project would not have been possible without his guidance. I always found my weekly trips to meet him at Antwerp University, though usually rainy, undoubtedly fruitful and insightful.

I would like to extend my sincere thanks to my promoter Dr. Christian Maes for his continuous support throughout the PhD and for the many stimulating conversations. I cannot recall an issue or a request that I brought to his attention which was not resolved immediately. Moreover, attending his class on quantum mechanics was indeed one of the pleasures of my doctoral study.

I would also like to thank the esteemed members of the examination committee for the careful reading of the manuscript and for their recommendations that helped me polish this work into its current form.

Special thanks to Dr. Raina Olsen for taking interest in my work and for all the intriguing discussions we had.

I am also grateful to Dr. Guido Groeseneken for giving me invaluable advice during my graduate studies. I appreciate how he constantly strives to better the scientific environment at imec for all PhD students.

Finally, I cannot forget to express my gratitude to all my colleagues at imec and KU Leuven with whom I have enjoyed this four-year journey. Special thanks to Joren Vanherck, Jeroen Verjauw, Mohamed Kordy, Rohit Acharya, Asser Khaled, Anton Potocnik, Olivier Bultynck, Bart Vermeulen, Myriam Janowski, Filip Sevenants, and Anneleen Marcelis.

On a personal level, I had the good fortune of marrying my lifelong partner and my best friend, Ghada. Between studying and train rides, it was not an easy task to maintain a cross-border long-distance relationship. I am grateful for your patience, love, and support during this laborious journey. You make everything possible. And I promise that the best is yet to come for us.

I am deeply grateful to my parents, Nashwa and Mohamed, for their continuous support during my graduate and undergraduate studies. I am humbled by your sacrifices and thankful for your endless love. It is a liberating feeling to know that you are proud of me regardless of what I do.

I would also like to acknowledge my sister, Maha, for always lending me a good ear and for helping me navigate the PhD journey. Your meticulous editorial skills enabled me to drastically improve this manuscript.

I also wish to thank my parents-in-law, Hanan and Hesham. I am blessed to be at the receiving end of your love, support, and prayers.

Finally, everyone is the hero of their own story and, if sci-fi movies taught me anything, every hero needs a sidekick. For this, I would like to thank Nard Dumoulin, the Samwise to my Frodo. I would not have been able to climb the PhD mountain and submit the One thesis without your fellowship.

Abstract

Quantum computers promise to execute certain tasks exponentially faster than classical computers. A fundamental challenge for upscaling quantum computers is the volatility of their building blocks—namely, qubits. For example, superconducting qubits require an external magnetic flux bias to tune their frequency, making them prone to dephasing via low-frequency flux noise. This thesis proposes an alternative platform for superconducting qubits that can be tuned electronically based on voltage-biased superconducting loops.

Today, superconducting qubits are based on Josephson junctions. Interrupting a superconducting loop with such a junction couples its discrete flux states and yields a flux qubit. Similarly, interrupting the loop with a nanowire weak link couples its flux states. This phenomenon is known as coherent quantum phase slips and has been harnessed to build phase-slip flux qubits. Nonetheless, specifying the frequency of such qubits entails complete control over the size and properties of the nanowire, which renders their fabrication challenging.

This thesis examines inducing the weak link electronically in uninterrupted superconducting rings to alleviate the strict fabrication requirements while enabling electronic tunability of the coupling of the flux states of the ring. Specifically, I evaluate the effect of the bias voltage on deterministic and quantum phase slips. Solving the time-dependent Ginzburg-Landau equations, I show that the bias voltage controls the free-energy barrier governing the dynamics of these phase slips. I accordingly propose two novel devices. First, I present a scalable superconducting memory whose state is stored and retrieved via picosecond voltage pulses. Superconducting memories are an essential ingredient for quantum computers owing to their compatibility with cryogenic working temperatures. Second, I propose a phase-slip flux qubit that is tunable by bias voltage and immune to fluctuations smaller than the coherence length of the superconductor. This design is therefore a promising candidate for scalable phase-slip flux qubits. As with other weak links, the work presented in this thesis suggests a route towards new superconducting quantum devices.

Beknopte samenvatting

Kwantumcomputers kunnen specifieke taken exponentieel sneller uitvoeren dan klassieke computers. Een fundamentele uitdaging om kwantumcomputers op te schalen is de volatiliteit van de basisbouwstenen waaruit deze is opgebouwd, met name de kwantumbits. Bijvoorbeeld, voor supergeleidende kwantumbits is een uitwendig magnetische flux nodig om de karakteristieke frequentie van deze bits aan te sturen. Hierdoor zijn deze kwantumbits ook gevoelig aan defasering via laagfrequente flux ruis. In dit doctoraat wordt een alternatief platform voorgesteld om supergeleidende kwantumbits aan te sturen op elektronische wijze met behulp van een aangelegde spanning over supergeleidende ringen.

De supergeleidende kwantumbits van vandaag zijn gebaseerd op Josephson juncties. Deze juncties zijn aangebracht in supergeleidende stroomkringen en koppelt de discrete gekwantiseerde fluxtoestanden. Op gelijkaardige wijze, door een supergeleidende kring te voorzien van zwakke link (Engels: "weak link") kunnen fluxtoestanden ook met elkaar gekoppeld worden. Dit verschijnsel is gekend als coherente kwantumfaseslips en vormt tevens een mogelijke route om zogenaamde faseslip flux kwantumbits te realiseren. Ook voor deze structuren is het nodig om de karakteristieke frequentie te bepalen via een volledige controle over de grootte en de eigenschappen van de fase slip nanodraad die de zwakke link realiseert wat een enorme uitdaging is voor de fabricatie ervan.

Deze thesis onderzoekt of een zwakke link elektronisch kan worden geïnduceerd in supergeleidende stroomkringen om de fabricatie gemakkelijker te maken en tegelijk de koppeling van de fluxtoestanden op elektrische manier te manipuleren. In het bijzonder wordt onderzocht wat het effect is van een aangelegde spanning op deterministische en kwantum faseslips. Om dit te onderzoeken worden de tijdsafhankelijke Ginzburg-Landau vergelijkingen opgelost. Dit stelt ons in staat om te tonen op welke manier de aangelegde spanning de vrije energiebarrière en bijgevolg de dynamica van deze faseslips

bepaalt. Er worden twee nieuwe componenten voorgesteld en beschreven. Eerst wordt een schaalbare supergeleidend kwantumgeheugen beschreven waarbij de kwantumtoestand wordt geschreven of gelezen door het aanleggen van picoseconde elektrische spanningspulsen. Supergeleidende kwantumgeheugens zijn een essentieel ingrediënt voor kwantumcomputers omdat deze net zoals kwantumcomputers ook op cryogene temperaturen werken. Ten tweede wordt ook een faseslip kwantumbit voorgesteld die gemanipuleerd kan worden door het aanleggen van een uitwendige spanning en niet meer gevoelig is aan fluctuaties die kleiner zijn dan de coherentielengte van de gebruikte supergeleider. Dit ontwerp vormt dan ook een interessante kandidaat voor een schaalbare faseslip kwantumbit. Het onderzoekswerk dat werd verricht tijdens dit doctoraat levert dan ook een aantal routes op om nieuwe supergeleidende kwantumcomponenten te ontwerpen.

Contents

1	Introduction	1
1.1	Quantum circuits with Josephson junctions	4
1.2	Quantum circuits with phase-slip junctions	15
1.3	Objective of the thesis	20
1.4	Outline of the thesis	22
2	Theoretical Background	25
2.1	Landau theory for phase transitions	26
2.2	Ginzburg-Landau equations	28
2.3	Model of a superconducting ring	41
3	Voltage-Biased Superconductors	47
3.1	Voltage-biased superconducting strip	48
3.2	Voltage-biased superconducting ring	53
4	Deterministic Transitions between Flux States	65
4.1	Critical flux for a deterministic phase slip	66
4.2	Reduction of critical flux by bias voltage	71
4.3	Proposal for a superconducting memory	79
5	Stochastic Transitions between Flux States	95
5.1	Stochastic versus deterministic phase slips	96
5.2	Energy barrier for a stochastic phase slip	99
5.3	Suppression of energy barrier by bias voltage	107
5.4	Proposal for a phase-slip flux qubit	112
6	Conclusions	123
6.1	Outlook	126
	Appendices	129
	Bibliography	159

1

Introduction

In the beginning of the twentieth century, there were two main competing theories of what happens to the resistivity of metals as temperature approaches absolute zero [1, 2]. The first theory, proposed by Matthiessen, predicted that the zero-temperature resistivity of metals saturates to a predetermined value, which depends on sample impurities and defects. In contrast, the second theory—defended by Lord Kelvin—predicted that the charge carriers would freeze at zero temperature, thereby preventing further flow of electric current (i.e., the resistivity diverges to infinity at absolute zero). Due to technological limitations at that time, metals could not be cooled down to temperatures close to absolute zero. Consequently, experimental evidence that would vindicate either of the two theories was still missing.

In 1908, Kamerlingh Onnes—in his renowned low-temperature physics laboratory—managed to liquefy and store Helium so that he can conduct low-temperature experiments on other materials [1]. At that point, Kamerlingh Onnes was in a position to settle the dispute regarding the resistivity of metals at very low temperatures. Hoping to circumvent the resistivity originating from impurities, Kamerlingh Onnes focused on mercury because it is a liquid metal and can be readily purified with distillation. In 1911, Kamerlingh Onnes discovered that the resistivity of mercury follows Matthiessen’s prediction down to a temperature of 4.2 K, at which it abruptly drops to zero, or more precisely to an immeasurably small value [3]. He referred to this phenomenon as *supraconductivity*, later dubbed superconductivity. The zero resistivity of a superconductor implied that a current continues to flow in the absence of a

1. Introduction

driving force, as confirmed by many experiments where the superconducting current, also called supercurrent, persists in rings for years [4].

Another fundamental step towards perceiving superconductivity as a distinct state of matter is the Meissner effect. In 1933, Walther Meissner and Robert Ochsenfeld discovered that the magnetic flux lines are expelled from the bulk of a superconductor [5]. This observation disagrees with the expected behavior of a perfect conductor—that is, when the resistivity ρ equals zero. According to Ohm's law, the electric field inside a superconductor equals zero ($\mathbf{E} = \rho \mathbf{J} = 0$, where \mathbf{J} is the current density). Accordingly, Faraday's law of induction dictates that the magnetic field inside the superconductor is time independent, which implies that the magnetic flux lines can be trapped inside the superconductor. This contraction revealed that superconductivity is a distinct state of matter defined by both perfect conductivity and perfect diamagnetism (the Meissner effect). In 1935, the London brothers, embracing the quantum zeitgeist, adapted the laws of electrodynamics to explain the Meissner effect [6]. Particularly, they related the supercurrent density to the magnetic vector potential, instead of the electric field.

Despite the progress made by the London brothers, Ginzburg, and Landau to phenomenologically describe the behavior of superconductors, a microscopic theory that explains superconductivity eluded physicists for a long time. It was not until 1957 that Bardeen, Cooper, and Schrieffer devised their masterpiece, known as the BCS theory [7, 8]. According to the BCS theory, pairs of electrons combine to form *Cooper pairs*, which act like bosonic particles and condense into a single macroscopic quantum state with a well-defined phase. In fact, the use of superconductors to build quantum circuits hinges on the phase coherence of their wave function.

Since its discovery, superconductivity has found many useful applications, ranging from large-scale superconducting magnets [9] for magnetic resonance imaging and particle accelerators to sensitive magnetic detectors [10] and fast-switching digital circuits, known as rapid-single-flux-quantum logic [11]. This thesis, however, focuses on the domain of quantum information processing, specifically the use of superconductors to build quantum bits (qubits).

The rest of this introductory chapter is organized as follows. Section 1.1 discusses the Josephson effect arising when two superconducting electrodes are brought together in proximity and the various qubits based on the Josephson effect. An analogous class of circuits, known as quantum phase-slip circuits, is examined in Section 1.2. Finally, Section 1.3 identifies the aim of the thesis, and Section 1.4 presents a detailed outline.

1.1 Quantum circuits with Josephson junctions

This section explores the concept of superconducting quantum circuits with an emphasis on quantum bits (qubits). At the heart of these qubits lies a Josephson junction, two superconducting electrodes separated by a thin insulating barrier. I start by introducing the Josephson effect. Next, I present the basic types of superconducting qubits, focusing on flux qubits because they resemble other devices proposed in this thesis.

1.1.1 The Josephson effect

To understand superconducting quantum circuits, it is not necessary to delve into the microscopic details and origin of superconductivity. Instead, we are interested in the Josephson effect occurring when two superconducting electrodes, separated by a thin insulator, are brought together [12, 13]. The two equations governing the dynamics of a Josephson junction can be derived in multiple ways—for example, using the time-dependent Schrödinger equation [14], or using the time-independent Ginzburg-Landau equation [4]. Here, I follow an intuitive tight-binding model for the Josephson junction that does not presume detailed knowledge of superconductivity [15].

We start by considering an isolated, superconducting electrode where all electrons are paired. The ground state of the electrode consists of all Cooper pairs condensed in the lowest energy level with a finite excitation gap 2Δ , denoting the energy required to break a Cooper pair. If this gap exceeds other energy scales—especially, thermal energy—then the Hilbert space of the electrode is well-approximated by a single quantum state $|N\rangle$, labeled by the number of Cooper pairs. To form a Josephson junction, we connect two identical electrodes with a thin insulating barrier. Now, the total number of pairs in the overall system equals $N_L + N_R$, with the subscripts labeling either the left or the right electrode. Because Cooper pairs can tunnel between the electrodes, the junction is characterized, in the bra-ket notation, by the state

$$|m\rangle \equiv |N_L - m, N_R + m\rangle, \quad (1.1)$$

where m is the number of Cooper pairs that tunneled from the left (L) to the right (R) electrode, starting from an initial reference state (i.e., the moment

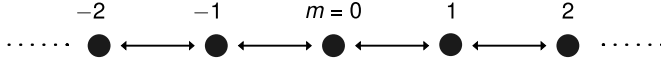


Figure 1.1 | Tight-binding model for a Josephson junction, represented here by a one-dimensional lattice with nearest-neighbor hopping. The lattice sites, labeled by m , correspond to the number of Cooper pairs that tunnel across the junction.

before connecting both electrodes). The Hilbert space of the composite system consists of a family of degenerate states $\{|m\rangle\}$.

The tunneling of Cooper pairs is described by the model Hamiltonian

$$\hat{\mathcal{H}}_{\text{tun}} = -\frac{E_J}{2} \sum_m (|m-1\rangle\langle m| + |m+1\rangle\langle m|), \quad (1.2)$$

where E_J is the Josephson coupling energy characterizing the ability of Cooper pairs to tunnel across the insulating barrier. If we choose the number of pairs m that tunnel across the junction to be the coordinate of the system, then the Hamiltonian (1.2) represents a one-dimensional tight-binding model with nearest-neighbor hopping (Figure 1.1). An increasing m corresponds to Cooper pairs tunneling from the left electrode to the right one, whereas a decreasing m corresponds to Cooper pairs tunneling in the opposite direction.

For this one-dimensional lattice, the eigenstates are the plane waves

$$|\delta\rangle \equiv \sum_m e^{im\delta} |m\rangle, \quad (1.3)$$

where the dimensionless wave number δ denotes the phase difference across the junction. Acting with the Hamiltonian (1.2) on the state $|\delta\rangle$ leads to the dispersion relation

$$\hat{\mathcal{H}}_{\text{tun}} |\delta\rangle = -E_J \cos \delta |\delta\rangle. \quad (1.4)$$

The current across the junction then takes the form

$$I = \frac{2e}{\hbar} \frac{\partial}{\partial \delta} (-E_J \cos \delta) = I_c \sin \delta, \quad (1.5)$$

where I_c denotes the maximum dissipationless current through the junction, and it is defined as $I_c \equiv 2eE_J/\hbar$, where e is the electronic charge and \hbar is the

reduced Planck's constant. The current-phase relation (1.5) is known as the first Josephson equation, or the dc Josephson effect, and it states that, even in the absence of an external force, a net current of Cooper pairs flows across the junction as a result of the phase difference between the two superconductors.

The second Josephson equation describes the dynamics of a junction subjected to a bias voltage. For a voltage difference V between the two electrodes, the potential energy term

$$\hat{U} = -2eV\hat{n}, \quad (1.6)$$

is added to the Hamiltonian, with the number operator \hat{n} defined as

$$\hat{n} \equiv \sum_m |m\rangle m \langle m|. \quad (1.7)$$

The voltage-phase relation follows from the Hamilton equation

$$\hbar \frac{\partial \delta}{\partial t} = - \frac{\partial \hat{\mathcal{H}}}{\partial \hat{n}} = 2eV, \quad (1.8)$$

which relates the coordinate \hat{n} to its conjugate momentum $\hbar\delta$. The second Josephson equation, also known as the ac Josephson effect, is conventionally written as

$$\hbar \dot{\delta} = 2eV, \quad (1.9)$$

stating that the phase difference across the junction evolves in time in the presence of a constant bias voltage.

1.1.2 Circuit model for a Josephson junction

Having introduced the celebrated Josephson equations, our next step is to define a circuit element that encapsulates the Josephson junction. In addition to Cooper pairs oscillating back and forth between the two superconductors, there is a capacitive energy involved because the junction stack forms a parallel-plate capacitor. Therefore, the circuit representation of the junction is a Josephson element in parallel with a capacitor, characterized by the Josephson energy E_J and the capacitance C_J , respectively (Figure 1.2c).

The Hamiltonian of an isolated Josephson junction comprises two energy scales: the energy stored in the Josephson element and the energy stored in the

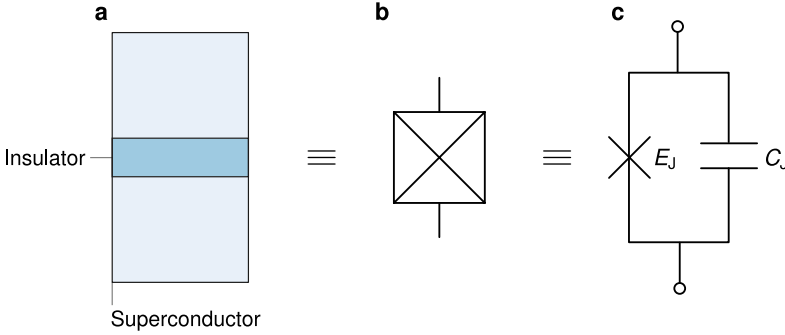


Figure 1.2 | Circuit model of a Josephson junction. a | A Josephson junction consists of two superconducting electrodes separated by a thin insulating barrier. **b** | Circuit representation of the Josephson junction. **c** | The junction consists of a Josephson element, characterized by the Josephson energy E_J , in parallel with a capacitor C_J .

capacitor. First, using the two Josephson equations, the energy stored in the Josephson element is defined as

$$E_{JJ} = \int_0^t IV dt = E_J(1 - \cos \delta). \quad (1.10)$$

Second, the energy stored in the capacitor is defined as

$$E_{C_J} = \frac{1}{2} C_J V^2. \quad (1.11)$$

Choosing the flux as the coordinate of the system leads to the Lagrangian

$$\mathcal{L} = \frac{1}{2} C_J \dot{\Phi}^2 - E_J \left[1 - \cos \left(2\pi \frac{\Phi}{\Phi_0} \right) \right], \quad (1.12)$$

where $\dot{\Phi}$ denotes the time derivative of flux, and the flux quantum Φ_0 is defined as $h/(2e) \approx 2 \times 10^{-15}$ Wb. Comparing the Lagrangian (1.12) with that of a simple harmonic oscillator reveals that the capacitive energy corresponds to kinetic energy, and that the Josephson energy corresponds to potential energy. The Josephson element can be considered a nonlinear inductor because, for a small phase difference, the current is linearly proportional to the flux, and the junction behaves as an inductor with an inductance

$$L_J \equiv \frac{1}{E_J} \left(\frac{\Phi_0}{2\pi} \right)^2. \quad (1.13)$$

1. Introduction

The momentum Q conjugate to the flux coordinate is defined as

$$Q \equiv \frac{\partial \mathcal{L}}{\partial \dot{\Phi}} = C_J \dot{\Phi}, \quad (1.14)$$

denoting the charge stored in the capacitor. The Legendre transform results in the Hamiltonian

$$\begin{aligned} \mathcal{H} &= Q\dot{\Phi} - \mathcal{L} \\ &= \frac{Q^2}{2C_J} - E_J \cos\left(2\pi \frac{\Phi}{\Phi_0}\right). \end{aligned} \quad (1.15)$$

Defining the superconducting charging energy as $E_C \equiv (2e)^2/(2C_J)$ yields

$$\mathcal{H} = E_C n^2 - E_J \cos\left(2\pi \frac{\Phi}{\Phi_0}\right), \quad (1.16)$$

where $n \equiv -Q/(2e)$ is the number of Cooper pairs stored in the capacitor C_J . So far, all the variables in the Hamiltonian (1.16) are classical. For a quantum representation, we replace the variables Φ and n by operators satisfying the canonical commutator

$$[\hat{\Phi}, \hat{n}] = -\frac{i\hbar}{2e}, \quad (1.17)$$

where the flux is the coordinate, and the particle number is its conjugate momentum. The isolated junction is thus described by the Hamiltonian

$$\hat{\mathcal{H}} = E_C \hat{n}^2 - E_J \cos 2\pi \hat{\phi}, \quad (1.18)$$

with $\hat{\phi} \equiv \hat{\Phi}/\Phi_0$ denoting the normalized magnetic flux.

The circuit model of the Josephson junction has been corroborated by many experiments [16, 17], and later by the realization of various Josephson-based qubits [18–24]. The next section discusses the categories of these qubits and explains the need for the Josephson junction.

1.1.3 Basic types of superconducting qubits

A qubit is a quantum system with two energy levels, conventionally labeled $|0\rangle$ and $|1\rangle$ to denote the ground and the excited states, respectively. In contrast to a classical bit, a qubit can exist in a superposition state

$$|\psi\rangle = \alpha |0\rangle + \beta |1\rangle, \quad (1.19)$$

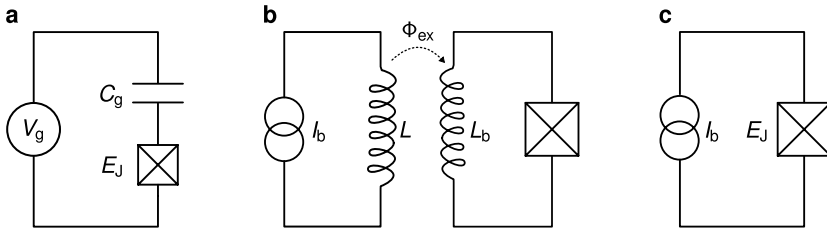


Figure 1.3 | Basic types of superconducting qubits. Based on the biasing mechanism and the computational variable, qubits with Josephson junctions are classified into three types: (a) charge, (b) flux, and (c) phase qubits.

where the complex coefficients α and β are probability amplitudes—that is, the probability to measure the qubit in the state $|0\rangle$ is $|\alpha|^2$, and the probability to measure the qubit in the state $|1\rangle$ is $|\beta|^2$.

In practice, to build a qubit out of an arbitrary quantum system, one must isolate two energy levels. This requirement cannot be achieved with passive circuit elements. Specifically, the parabolic potential energy of an LC circuit yields a harmonic energy spectrum—that is, a spectrum with equidistant energy levels. Because of the equidistant energy spectrum, one cannot induce a transition between the lowest two levels without leakage to higher levels. Conversely, the cosine potential energy of the Josephson junction yields an anharmonic energy spectrum. This anharmonicity prevents leakage to higher energy levels upon exciting the qubit. Superconducting quantum circuits based on Josephson junctions have been employed in several devices such as superconducting quantum interference devices (SQUIDs) [10], parametric amplifiers [25, 26], and superconducting qubits [18–24].

The Hamiltonian of an isolated Josephson junction includes two energy scales: the superconducting charging energy E_C and the Josephson energy E_J . Connecting the junction with an inductor L in parallel leads to an additional energy scale E_L . The relative ratios of these three energies manipulates the potential energy landscape, giving rise to a zoo of superconducting qubits such as the Cooper-pair box [27, 28], the phase qubit [29], the flux qubit [30–35], the fluxonium [36, 37], the qantronium [38], the Xmon [39, 40], and the

transmon [41, 42]. Today, transmons embedded in microwave resonators constitute the major scalable platform for superconducting qubits [43, 44], an architecture known as circuit quantum electrodynamics [42, 45–48].

Broadly speaking, superconducting qubits are classified, based on the circuit topology, into three categories: flux, charge, and phase qubits (Figure 1.3). The next section focuses on flux qubits.

1.1.4 Flux qubits

Superconducting qubits that use the magnetic flux as the computational variable come in various flavors. The three main categories are the rf SQUID qubit, the three-junction flux qubit, loosely known as the flux qubit, and the fluxonium qubit (Figure 1.4). This section focuses on the prototypical implementation of flux qubits, namely the rf SQUID qubit.

But it is instructive to first study a junctionless superconducting loop. Because the superconducting wave function is single-valued, the phase accumulated along the loop must be an integer multiple of 2π . Equivalently, the single-valuedness of the wave function entails the quantization of the magnetic flux enclosed by the loop. For example, when a superconducting ring is placed in a magnetic field, a supercurrent flows to expel the field from the bulk of the ring and to ensure that the enclosed flux is quantized and is equal to zero. As the magnetic field increases, the ring transitions between discrete flux states, characterized by the phase winding number, to minimize its energy. In other words, the ring allows an integer multiple of the flux quantum to be enclosed to reduce the circulating supercurrent. Unfortunately, these transitions are dissipative because, for the winding number to change, the phase must make a discontinuous jump at a point where the density of Cooper pairs is strongly suppressed. These events are referred to as phase slips.

In short, the discrete flux states of an uninterrupted superconducting ring are not coherently coupled because transitions require dissipative breaking of the cylindrical symmetry of the ring. One mechanism for coherent coupling is to inherently break the symmetry by interrupting the ring with an insulator,

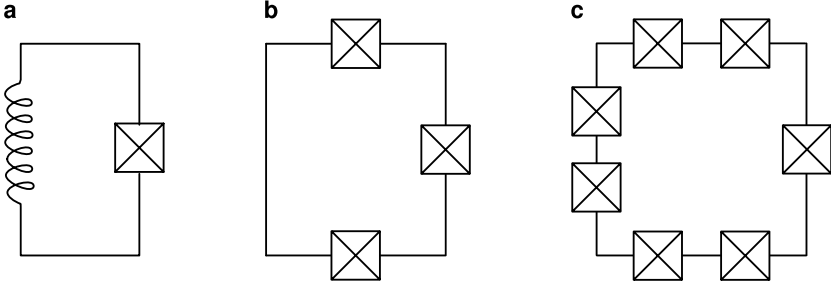


Figure 1.4 | The three main flavors of superconducting flux qubits. (a) the rf SQUID qubit, (b) the three-junction flux qubit, and (c) the fluxonium qubit.

thereby forming a Josephson junction. The inclusion of the junction gives rise to the simplest implementation of flux qubits, the rf SQUID qubit.

The rf SQUID consists of a superconducting loop incorporating a Josephson junction (Figure 1.5). Following the same quantization procedure of the isolated junction leads to the rf SQUID Hamiltonian

$$\hat{\mathcal{H}} = U_0 \left(\beta_C \hat{n}^2 + 2\pi^2 (\hat{\phi} - \phi_{\text{ex}})^2 - \beta_J \cos 2\pi \hat{\phi} \right). \quad (1.20)$$

The external flux bias is denoted by ϕ_{ex} , and the energy U_0 is defined as

$$U_0 \equiv \frac{\Phi_0^2}{4\pi^2 L}, \quad (1.21)$$

with L as the inductance of the loop. The parameter β_C is the ratio of the superconducting charging energy to U_0 . Likewise, the parameter β_J is the ratio of the Josephson energy to U_0 .

The Hamiltonian (1.20) resembles that of a particle with mass C_J moving in a parabolic potential due to the loop inductance, modulated by cosine corrugations due to the Josephson element. Biasing the rf SQUID loop with a half-integer flux quantum creates a double-well potential whose two minima correspond to two currents with equal magnitude and opposite polarity (Figure 1.6a). For example, at a flux bias $\phi_{\text{ex}} = 1/2$, the loop can be in two degenerate states, labeled $|0\rangle$ and $|1\rangle$. First, the state $|0\rangle$ denotes a clockwise current that screens the external flux, leading to zero flux quanta in the loop.

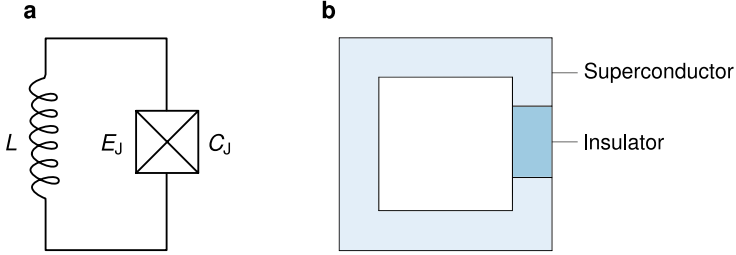


Figure 1.5 | The rf SQUID qubit consists of a superconducting loop interrupted by a Josephson junction. **a** | The equivalent circuit of the rf SQUID.

Second, the state $|1\rangle$ denotes an equal counterclockwise current that augments the external flux, leading to one flux quantum in the loop. Tunneling of Cooper pairs across the insulator, however, admixes these two states. The eigenstates of the qubit are the symmetric and antisymmetric superpositions of the macroscopic flux states $|0\rangle$ and $|1\rangle$. The coupling of the flux states manifests as an avoided crossing in the energy spectrum of the rf SQUID qubit.

The rf SQUID operates under two conditions. First, to minimize fluctuations of the flux variable, the qubit works in the phase regime $\beta_J \gg \beta_C$. In this regime, the capacitance is large, and the nonlinear inductance of the Josephson junction is small; hence, flux fluctuations are negligible, and the flux variable is a good quantum number. Second, for the potential landscape to exhibit a double well, the induction parameter $\beta_J \gtrsim 1$. For $\beta_J \ll 1$, the cosine term is negligible, and the potential energy is parabolic. In that limit, the Hamiltonian (1.20) reduces to that of an LC oscillator. On the other hand, for $\beta_J \gg 1$, the cosine modulation dominates, but the barrier forbids coupling of the flux states. In other words, for infinitely strong Josephson coupling E_J , the thickness of the insulator tends to zero, and the rf SQUID reduces to an uninterrupted loop in which the discrete flux states are not coherently coupled.

To gain an insight into the condition $\beta_J \gtrsim 1$, we could compare the geometric inductance of the superconducting loop $L = \Phi_0^2/(4\pi U_0)$ and the effective Josephson inductance $L_J = \Phi_0^2/(4\pi E_J)$. For $\beta_J \equiv E_J/U_0 = 1$, both inductances are equal. Accordingly, the double well occurs slightly above the resonance

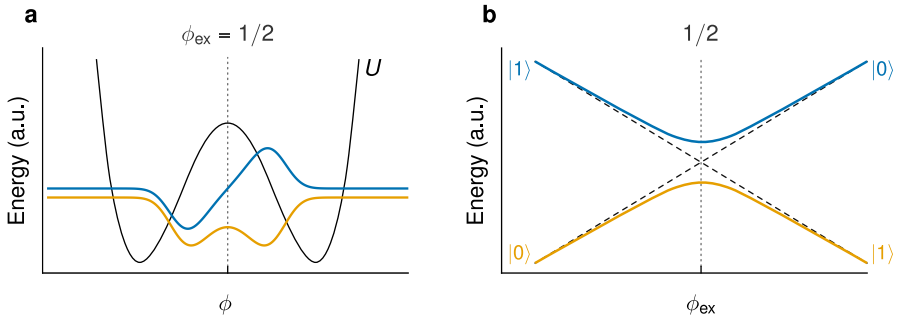


Figure 1.6 | Energy spectrum of the rf SQUID qubit. **a** | The potential energy U is plotted as a function of the flux coordinate ϕ , at an external flux bias $\phi_{\text{ex}} = 1/2$. The double-well potential corresponds to two oppositely circulating currents. The left well denotes the flux state $|0\rangle$ with a clockwise current, and the right well denotes the flux state $|1\rangle$ with a counterclockwise current. The eigenstates are the symmetric and antisymmetric superpositions of these two states, illustrated here by the probability amplitudes. **b** | The lowest two energy levels of the rf SQUID qubit as a function of ϕ_{ex} .

between the geometric and Josephson inductances. To make both inductances comparable, a large loop is required. But as its size increases, the loop can accumulate more flux noise from the environment, resulting in the low coherence times of the rf SQUID qubit [49, 50]. One variation that mitigates the noise problem is the three-junction flux qubit (Figure 1.4b). By exchanging the geometric inductance with two additional junctions, a smaller loop can be employed to reduce the accumulated flux noise.

In conclusion, the simplest flux qubit consists of a superconducting loop interrupted by a Josephson junction. The need for the Josephson weak link can be understood from three perspectives. First, from a microscopic perspective, it is the coherent tunneling of Cooper pairs across the barrier that couples the flux states of the loop. Second, from a circuit perspective, the nonlinearity of the Josephson inductance results in an anharmonic energy spectrum, a prerequisite to isolate a two-level quantum system. Third, from a mesoscopic perspective, the suppression of the Cooper-pair density in the junction predetermines the location of phase slips and eliminates the need for suppressing superconductivity elsewhere. Thus, the Josephson junction acts as a valve through which fluxons—that is, vortices—enter and leave the loop.

1. Introduction

An inherent limitation of the Josephson weak link is the fixed transition frequency of the qubit, set by the dimensions of the insulating barrier and the choice of the superconductor. Specifically, according to the Ambegaokar-Baratoff relation, the superconducting gap and the normal-state resistance of the junction determine the Josephson energy E_J [51]. The qubit transition frequency can, however, be magnetically tuned by replacing the Josephson junction with a dc SQUID, two junctions in parallel [4, 52]. The effective Josephson energy of the dc SQUID depends on the overall magnetic flux enclosed within its loop. Nevertheless, the magnetic tunability of the transition frequency renders Josephson-based qubits sensitive to flux noise or limits them to a fixed frequency operation.

1.2 Quantum circuits with phase-slip junctions

Incorporating a Josephson junction in a superconducting loop is crucial for coherent coupling of the flux states. The insulating barrier of the junction can be replaced by another form of a weak link—for example, a topological insulator [53], a van der Waals heterostructure [54], a two-dimensional electron gas [55], a semiconducting nanowire [56, 57], or a superconducting nanowire. For a superconducting nanowire or even a geometric constriction, a phenomenon dual to the Josephson effect arises, referred to as coherent quantum phase slips. This section introduces quantum phase slips and the emergence of quantum phase-slip circuits.

1.2.1 Quantum phase slips in superconducting nanowires

According to the Mermin-Wagner theorem, a one-dimensional system cannot host the long-range order of superconductivity [58]. With the purpose of investigating the scaling limit of superconductors, numerous experiments were conducted on ultra-thin superconducting wires [59–61]. The experimental setup consisted of a superconducting nanowire embedded between two superconducting leads, connected to an external current source (Figure 1.7a). The resistance of the wires was determined by measuring the voltage drop across the sample. If the normal-state resistance R_n is higher than the Cooper-pair quantum of resistance ($R_q \equiv (2e)^2/h$), the wires do not transition to the superconducting state. Moreover, as the resistance per unit length increases, the superconducting transition broadens, even for homogeneous samples.

These two observations have been justified by the Langer-Ambegaokar-McCumber-Halperin (hereafter LAMH) theory [62, 63], which attributes the resistance below the critical temperature to thermally activated phase slips. Particularly, the LAMH theory derives an expression for the rate of phase slips as a function of the energy barrier that the nanowire surmounts for a phase slip. In general, a phase slip requires the density of Cooper pairs to be locally suppressed so that the ill-defined, unrestricted phase can exhibit a 2π discontinuity [52, 64]. The suppression of the Cooper-pair density is accompanied by a voltage drop, giving rise to a measurable resistance.

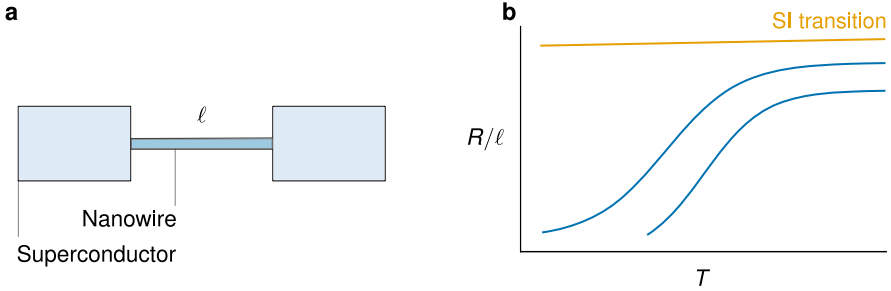


Figure 1.7 | Thermally activated phase slips in superconducting nanowires. a | The resistance due to phase slips is determined by measuring the voltage drop across a nanowire of length ℓ . **b** | Schematic of the data measured in [66]. The broadening of the superconducting transition temperature, especially for wires with higher normal-state resistance per length R_n/ℓ , is explained by thermally activated phase slips. For wires with a higher normal-state resistance, a Superconductor-Insulator (SI) transition occurs.

According to the LAMH theory, the rate of thermally activated phase slips (TAPS) follows the Arrhenius law

$$\Gamma_{\text{TAPS}} \propto e^{-\Delta F/k_B T}, \quad (1.22)$$

where $k_B T$ is the thermal energy with the Boltzmann constant k_B . The energy barrier ΔF is proportional to the product of the condensation energy per unit volume f_C and the volume of a phase slip, i.e., the barrier takes the form

$$\Delta F \propto f_C \sigma \xi, \quad (1.23)$$

where σ is the cross-sectional area of the nanowire, and ξ is the coherence length [65]. Since the normal-state resistance per unit length is inversely proportional to the cross-sectional area, the energy barrier decreases as the ratio R_n/ℓ increases. Consequently, the superconducting transition broadens up to the limit of the superconductor-insulator transition.

One problem, however, with attributing the measured resistance solely to thermal phase slips is that the resistance is predicted to be exceedingly low at a few tens of millikelvin because thermal activation is exponentially suppressed. In other words, the systematic broadening of the transition temperature with decreasing cross-sectional areas is explained by thermally activated phase slips up to a certain temperature range, below which the LAMH theory fails.

The cause of the measured resistance at low temperatures was suggested to be quantum tunneling of phase slips through the energy barrier. This additional escape mechanism is revealed by fitting the resistance to the rate equation (1.22) with an escape temperature T_{esc} [67]. For temperatures higher than $T_c/2$, the escape temperature approximately equals the measurement temperature, in agreement with the LAMH theory. But, as the temperature decreases below $T_c/2$, the escape temperature plateaus, implying an additional escape mechanism, weakly dependent on temperature. This phenomenon was later dubbed quantum phase slips [66, 68–73]. Various models were proposed to evaluate the rate of quantum phase slips [74–78], and they have been used to accurately fit the resistance of superconducting nanowires [68, 79, 80].

1.2.2 Phase-slip flux qubits

In 2005, Mooij [81, 82] proposed that if we embed a superconducting nanowire as a weak link in a superconducting loop, quantum phase slips may serve as a coherent coupling mechanism between the flux states of the loop (e.g., the flux states $|0\rangle$ and $|1\rangle$ at a half-flux-quantum bias). Specifically, he suggested that coherent quantum phase slips are dual to the Josephson effect and can be exploited to construct a phase-slip flux qubit with the two-level Hamiltonian

$$\hat{\mathcal{H}} = I\Phi_0(\phi - 1/2)\sigma_z + h\Gamma_{\text{QPS}}\sigma_x, \quad (1.24)$$

where ϕ is the normalized flux enclosed by the loop, and I is the circulating current. The operators σ_x and σ_z denote the Pauli spin matrices. The rate of quantum phase slips Γ_{QPS} determines the transition frequency of the qubit.

To illustrate the magnitude of the transition frequency, I follow the example presented by Mooij in [81]. According to Giordano [75, 76], the rate of quantum phase slips depends exponentially on the energy barrier in the form (1.22) with the thermal energy replaced by \hbar/τ , where τ is the Ginzburg-Landau relaxation time. In terms of experimentally accessible parameters, the rate of quantum phase slips (QPS) is expressed as

$$\Gamma_{\text{QPS}} = \frac{3B}{2} \frac{\ell}{2\pi\xi} \sqrt{\frac{R_q}{R_\xi} \frac{k_B T_c}{\hbar}} \exp\left(-0.3a \frac{R_q}{R_\xi}\right), \quad (1.25)$$

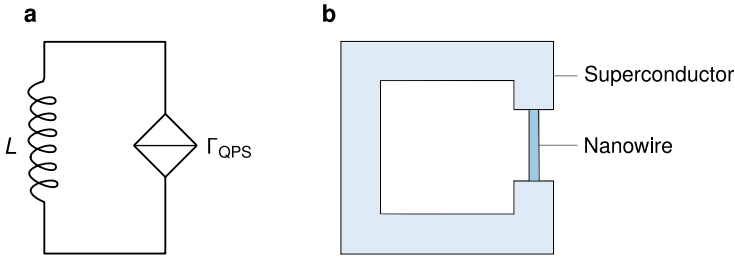


Figure 1.8 | Phase-slip flux qubit. a | In this circuit model, the phase-slip junction is characterized by the rate of quantum phase slips Γ_{QPS} , and the size of the loop by the geometric inductance L . **b** | The qubit consists of a superconducting loop interrupted by a nanowire. This geometry was first proposed by Mooij in [81, 82].

where the parameters a and B are of order unity, and R_q is the Cooper-pair quantum of resistance. The resistance R_ξ is defined as $R_\xi \equiv R_n \xi / \ell$ with R_n being the normal-state resistance.

Based on the form (1.25), the rate of quantum phase slips depends on two properties of the superconductor: the normal-state resistance and the coherence length. First, as a function of the normal-state resistance per unit length, the rate of quantum phase slips increases exponentially (Figure 1.9). Second, because the condensation energy is inversely proportional to the square of the coherence length, the energy barrier decreases as a function of the coherence length. Therefore, the longer the coherence length, the higher the rate of quantum phase slips. The coherence length and the normal-state resistance of the nanowire must be precisely controlled to realize a definite transition frequency, typically ranging from one to ten gigahertz.

In comparison with Josephson-based qubits, phase-slip qubits have three key advantages [81]. First, due to the absence of an insulating barrier, phase-slip flux qubits are insensitive to charge noise. Second, the energy barrier and the transition frequency of the qubit depend on macroscopic parameters. They are therefore immune to defects and fluctuations occurring on a scale much smaller than the coherence length. Third, the energy spectrum of the phase-slip qubit is strongly anharmonic—that is, the energy difference between the first and second levels is much smaller than the energy difference between the

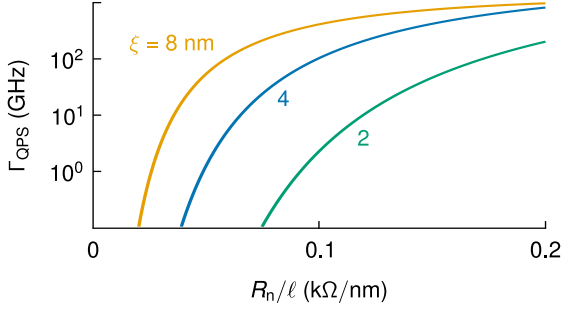


Figure 1.9 | The rate of quantum phase slips in a phase-slip flux qubit. The rate is plotted as a function of the normal-state resistance per unit length (R_n/ℓ) for three values of the coherence length ξ . The nanowire length $\ell = 50$ nm, and the critical temperature $T_c = 1.2$ K. The fitting parameters a and B are unity.

second and third levels. As a consequence, the two levels defining the qubit are isolated and can be addressed with minimal leakage to higher-energy states. Superconducting qubits with weak anharmonicity must employ pulse-shaping techniques to prevent leakage of quantum information to excited states [83].

But, similar to Josephson-based flux qubits, phase-slip qubits are sensitive to low-frequency flux noise. Specifically, deviations from the required half-flux-quantum bias alter the energy-level splitting and dephase the qubit. In addition, owing to the exponential dependence of the quantum-phase-slip rate, precise control over the dimensions of the nanowire and its superconducting properties is required to achieve a definite transition frequency.

Recent experiments demonstrated coherent quantum phase slips in InO [84], NbN [85, 86], and TiN [87, 88] nanowires. Since then, numerous quantum phase-slip circuits have been realized—for example, qubits [88], quantum interference devices [89, 90], single-charge transistors [91, 92], and even phase-slip circuits for neuromorphic computing [93].

1.3 Objective of the thesis

At the heart of superconducting qubits lies a weak link, often a Josephson junction or a superconducting nanowire. On the one hand, the Josephson junction must be replaced by a SQUID to magnetically tune the transition frequency of the qubit. The added flux-bias loop is a source of flux noise and limits the scalability of Josephson-based qubits. On the other hand, embedding a nanowire in a superconducting loop requires intricate nanostructuring to precisely control the dimensions and the superconducting properties of the nanowire. Given the inherent limitations of existing weak links, this thesis examines the possibility of electrically inducing a weak link in an uninterrupted superconducting loop to circumvent the need for advanced nanostructuring while allowing for electronic tuning of the coupling between the flux states of the loop. The results of this work establish a path towards novel superconducting quantum devices.

In this thesis, I examine the effect of a bias voltage on deterministic and quantum phase slips in continuous, metallic superconducting nanorings. Employing the time-dependent Ginzburg-Landau simulations, I rigorously demonstrate that the bias voltage induces two weak links, constituting preferential locations for nucleating phase slips in the ring. Moreover, the bias voltage provides complete control over the energy barrier governing deterministic and stochastic transitions between the discrete flux states of the ring. Based on the electronic control of the energy barrier, I present two novel quantum devices. First, I propose a scalable superconducting memory whose state is encoded by the absence or presence of a single flux quantum within the ring. The write and read operations are executed electrically via picosecond bias-voltage pulses. Scalable superconducting memories are an essential ingredient for building a large-scale superconducting quantum computer due to their compatibility with the cryogenic working temperatures of qubits. Second, I propose a phase-slip flux qubit with a broadly tunable transition frequency. In contrast to nanowire-based qubits, the proposed qubit allows for electronic tunability without the need for challenging nanostructuring beyond the fabrication of the ring itself. The operation of the proposed qubit depends on macroscopic parameters—most notably, the coherence length of the superconductor. As a consequence, it is immune to fluctuations and defects

occurring on a much smaller length scale. In addition, its energy spectrum is anharmonic. Therefore, the two levels defining the qubit are isolated and can be addressed with minimal leakage to higher levels.

1.4 Outline of the thesis

The content of this thesis is arranged in *four* chapters. Chapter 2 provides a macroscopic description of superconducting rings subject to electromagnetic fields. To begin with, Section 2.1 discusses Landau theory for second-order phase transitions. Next, Section 2.2 applies this theory in the context of superconductivity, giving rise to the celebrated Ginzburg-Landau theory of superconductivity. A time-dependent extension of the Ginzburg-Landau equations is presented in Section 2.2.4, constituting the main theoretical tool used throughout this thesis. Finally, Section 2.3 introduces the model of a superconducting ring and the numerical solution of the time-dependent Ginzburg-Landau equations.

Chapter 3 analyzes the suppression of the Cooper-pair density due to a bias voltage in two geometries: superconducting strips and superconducting rings. Section 3.1 demonstrates the reduction of the Cooper-pair density in a superconducting strip in response to a bias voltage as a function of the parameters of the superconductor and its dimensions. A similar behavior is described in Section 3.2 for a voltage-biased superconducting ring where the bias voltage induces two weak links, serving as preferential locations to nucleate phase slips in the ring.

Chapter 4 discusses the effect of a bias voltage on the deterministic transitions between the flux states of a superconducting ring. The critical flux for a deterministic transition between the flux states of a bare superconducting ring is defined in Section 4.1. Then, Section 4.2 highlights the reduction of the critical flux as a function of the bias voltage. A novel voltage-controlled superconducting memory is proposed in Section 4.3. The working principle of the memory is presented along with a thorough characterization of the memory fidelity as a function of thermal fluctuations, sample defects, and variations in the operational parameters.

Chapter 5 examines the effect of the bias voltage on the rate of quantum phase slips in a superconducting ring. To reconcile all the distinct types of phase slips, Section 5.1 qualitatively compares deterministic, thermal, and quantum

phase slips. The energy barrier governing these three escape mechanisms is defined in Section 5.2 according to the LAMH theory, in addition to a numerical estimation of the barrier in the presence of a bias voltage. Section 5.3 explores the dependence of the quantum-phase-slip rate on bias voltage, sample size, material quality, and superconductor parameters. A novel flux qubit design that harnesses the enhancement of quantum phase slips by bias voltage is proposed in Section 5.4. The electronic tunability of the qubit transition frequency is assessed, along with a detailed analysis of the sensitivity of the qubit to flux noise and device asymmetry.

Lastly, Chapter 6 concludes this thesis and suggests directions for future work.

2

Theoretical Background

Superconductivity is a distinct phase of matter existing below a characteristic temperature, known as the critical temperature. When a superconductor is heated above its critical temperature, the superconducting state is destroyed, forcing a transition to the normal state, much like ice transforms into water at zero Celsius. Seven years before the microscopic theory of Bardeen, Cooper, and Schrieffer, Ginzburg and Landau examined superconductivity from the standpoint of phase transitions. Specifically, their purpose was to describe superconductivity close to the transition temperature (i.e., the critical temperature of the superconductor). Based on the Ginzburg-Landau (GL) theory, this chapter provides a macroscopic description of superconductors subject to electromagnetic fields.

This chapter is organized as follows. Section 2.1 briefly discusses the general Landau theory for second-order phase transitions. Next, Section 2.2 applies Landau theory in the context of superconductivity, arriving at the celebrated Ginzburg-Landau equations, used extensively in this thesis. Finally, Section 2.3 presents the model of a superconducting ring, along with the numerical solution of the Ginzburg-Landau equations.

2.1 Landau theory for phase transitions

Landau theory starts with a deliberate choice to ignore the microscopic details. Instead, it focuses on a qualitative, macroscopic description near the critical temperature of a phase transition [94, 95]. Landau realized that second-order phase transitions involve the process of breaking an underlying symmetry of the system. For instance, above the Curie temperature, a magnet has no net magnetization. Below the Curie temperature, however, all the magnetic dipole moments align, and a net magnetization arises [96]. While the magnetization can point in any direction, the ferromagnet spontaneously chooses a definite one, i.e., the rotational symmetry is broken.

Moreover, one can identify a physical quantity—referred to as an order parameter—that is zero in the disordered phase above the critical temperature, and nonzero in the ordered phase below the critical temperature. For the paramagnetic-to-ferromagnetic transition, a proper order parameter is the magnetization of the material.

In a second-order phase transition, this parameter increases continuously from zero at the critical temperature and reaches its maximum at zero Kelvin. Because the order parameter tends to zero near the critical temperature, we can expand the free energy as a Taylor series

$$F = F_0 + \alpha\psi^2 + \frac{\beta}{2}\psi^4 + \dots, \quad (2.1)$$

where F_0 is the free energy of the disordered state, and ψ is the order parameter. The prefactors α and β are temperature-dependent expansion coefficients. The leading coefficient must be positive, otherwise the free energy would have no minimum. For the minimum of the free energy to be at a nonzero value of ψ , the coefficient α must be negative (Figure 2.1). Accordingly, the phase transition occurs precisely when α equals zero. Minimizing the free energy (2.1) leads to the order parameter

$$\psi^2 = \begin{cases} 0 & T > T_c \\ -\alpha/\beta & T < T_c \end{cases}, \quad (2.2)$$

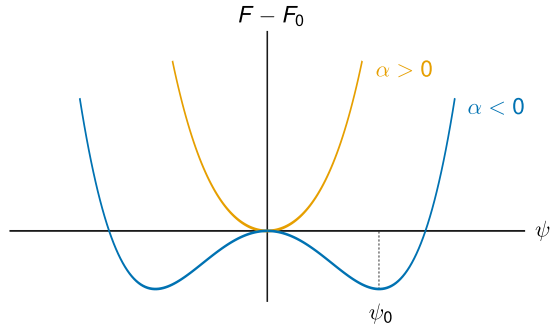


Figure 2.1 | Landau free energy as a function of the order parameter ψ . The phase transition occurs at $\alpha = 0$ since for $\alpha < 0$, the free-energy minimum is at a nonzero ψ .

where the critical temperature of the phase transition is denoted by T_c . The next section applies Landau's approach to superconductors, resulting in the celebrated Ginzburg-Landau theory of superconductivity.

2.2 Ginzburg-Landau equations

The Ginzburg-Landau theory describes superconductivity as a second-order phase transition, characterized by a complex order parameter [97]. Although meant to be phenomenological, the Ginzburg-Landau equations were derived from the microscopic BCS theory near the critical temperature by Gor'kov in 1959 [98]. Gor'kov demonstrated that the order parameter ψ represents a wave function of the center-of-mass motion of Cooper pairs, and that the squared magnitude $|\psi|^2$ corresponds to the density of Cooper pairs [98].

In powers of the magnitude of the complex order parameter, the free-energy density of the superconductor is approximated by

$$f_s = f_n + \alpha|\psi|^2 + \frac{\beta}{2}|\psi|^4, \quad (2.3)$$

where f_s and f_n represent the free-energy densities in the superconducting and normal states, respectively. If $\alpha \geq 0$, then the minimum of the energy difference $f_s - f_n$ is at $|\psi|^2 = 0$ (i.e., the material is in the normal state). In contrast, if $\alpha < 0$, then the minimum is at

$$|\psi|^2 = |\psi_0|^2 \equiv -\frac{\alpha}{\beta}, \quad (2.4)$$

where ψ_0 denotes the equilibrium value of the order parameter, deep into the bulk of the superconductor away from penetrating magnetic fields and surface currents [4]. Because ψ is complex, there exists an infinite number of degenerate minima denoting all allowed values of the phase χ of the complex order parameter

$$\psi = |\psi|e^{i\chi}. \quad (2.5)$$

In analogy to the definite direction of the magnetization of a ferromagnet, a superconductor spontaneously chooses a definite phase χ , thereby breaking the U(1) rotational symmetry [99].

Substituting with the equilibrium value (2.4) of the order parameter in the free-energy density (2.3) gives the difference

$$f_s - f_n = -\frac{\alpha^2}{2\beta}, \quad (2.6)$$

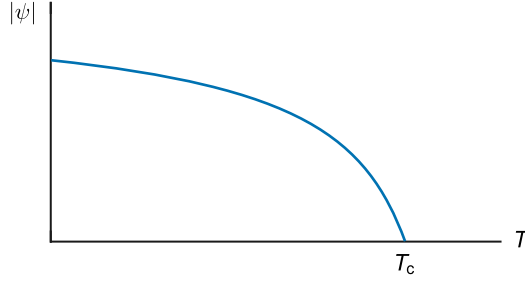


Figure 2.2 | Temperature dependence of the order parameter. The magnitude of the order parameter ψ increases continuously from zero at the critical temperature T_c .

denoting the energy gained by the transition to the superconducting state—that is, the condensation energy per unit volume f_c .

Near the critical temperature, the expansion coefficients are assumed to vary smoothly with temperature [52]. Thus, their temperature dependence follows the leading order of the Taylor expansion

$$\alpha(T) \propto \alpha(0)(T - T_c), \quad (2.7)$$

and

$$\beta \cong \text{const.} \quad (2.8)$$

The density (2.4) is thus proportional to $(T_c - T)$, as depicted in Figure 2.2.

In the presence of a magnetic field, the superconductor is described by the free-energy density

$$f_s = f_n + \alpha|\psi|^2 + \frac{\beta}{2}|\psi|^4 + \frac{|\mathbf{B}|^2}{2\mu_0} + \frac{1}{2m^*} |(-i\hbar\nabla - q\mathbf{A})\psi|^2. \quad (2.9)$$

The mass of a Cooper pair m^* equals twice the electronic mass. Likewise, the charge of a Cooper pair q equals twice the electronic charge. The penultimate term corresponds to the energy density of the magnetic field \mathbf{B} with the vacuum permeability μ_0 . The last term accounts for the spatial variations of the order parameter ψ due to supercurrent flow, where \mathbf{A} is the vector potential defined by the relation $\nabla \times \mathbf{A} = \mathbf{B}$.

2. Theoretical Background

Placing a superconductor in a magnetic field induces a supercurrent that expels the field from the bulk of the superconductor (i.e., the Meissner effect). The energy required for the flowing supercurrent is called the field expulsion energy, and it increases quadratically with the applied field. When the free-energy density of the superconducting state exceeds that of the normal state, the sample abruptly reverts to the normal state. Equating the condensation energy (2.6) to the energy density stored in the magnetic field leads to the thermodynamic critical field

$$B_{\text{cth}} = |\alpha| \sqrt{\frac{\mu_0}{\beta}}, \quad (2.10)$$

at which superconductivity is destroyed. Based on the temperature dependence of α and β , the GL theory predicts that the critical field varies linearly with temperature near the critical temperature ($B_{\text{cth}} \propto T_c - T$).

To obtain an equation that governs the spatial variation of $\psi(\mathbf{r})$, we minimize the energy functional

$$\frac{\delta F_s[\psi]}{\delta \psi^*} = 0, \quad (2.11)$$

where F_s is the overall free energy. The functional derivative yields the Ginzburg-Landau equation

$$\alpha \psi + \beta |\psi|^2 \psi + \frac{1}{2m^*} (-i\hbar \nabla - q\mathbf{A})^2 \psi = 0, \quad (2.12)$$

resembling Schrödinger equation for a wave function ψ with an additional nonlinear term. The second GL equation follows from Ampere's law

$$\nabla \times \nabla \times \mathbf{A} = \mu_0 \mathbf{J}_s, \quad (2.13)$$

with the supercurrent density \mathbf{J}_s defined as

$$\mathbf{J}_s = -\frac{q\hbar i}{2m^*} (\psi^* \nabla \psi - \psi \nabla \psi^*) - \frac{q^2 |\psi|^2}{m^*} \mathbf{A}. \quad (2.14)$$

Substituting with the complex order parameter in its polar form (2.5), we can rewrite the supercurrent density as

$$\mathbf{J}_s = \frac{q|\psi|^2}{m^*} (\hbar \nabla \chi - q\mathbf{A}). \quad (2.15)$$

The two GL equations (2.12) and (2.14) are solved self-consistently to obtain the spatial dependence of the complex order parameter and the magnetic field inside the superconductor. In the next section, I identify the characteristic length scales over which these two quantities vary.

2.2.1 Characteristic length scales of a superconductor

Two characteristic length scales arise naturally from the GL equations: the coherence length ξ and the penetration depth λ . First, to extract the coherence length, we consider a superconductor filling the half space $x > 0$, where x is the spatial coordinate (Figure 2.3). In the absence of an external magnetic field, the first GL equation (2.12) reduces to

$$\alpha\psi + \beta|\psi|^2\psi - \frac{1}{2m^*} \frac{d^2\psi}{dx^2} = 0. \quad (2.16)$$

Subject to the boundary conditions $\psi(0) = 0$ and $\psi(x \rightarrow \infty) = |\psi_0|$, this equation is satisfied by the order parameter

$$\psi(x) = |\psi_0| \tanh \frac{x}{\sqrt{2}\xi}, \quad (2.17)$$

where ξ is known as the coherence length and is defined by

$$\xi^2 \equiv \frac{\hbar^2}{2m^*|\alpha|}. \quad (2.18)$$

The coherence length specifies the distance over which the order parameter heals back to its equilibrium value. Thus, the shorter the coherence length, the lower the energy cost of a normal-superconductor interface (Figure 2.3).

Second, to extract the penetration depth, we rewrite the supercurrent (2.14) in the London limit—that is, assuming a constant magnitude of the order parameter. The supercurrent density, then, reduces to

$$\mathbf{J}_s = -\frac{q^2|\psi|^2}{m^*} \mathbf{A}, \quad (2.19)$$

as proposed by the London brothers to relate the supercurrent to the vector potential, instead of the electric field as in Ohm's law [6]. Taking the curl of

2. Theoretical Background

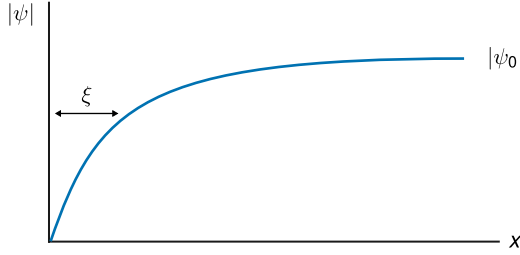


Figure 2.3 | The coherence length ξ . Starting from the surface of the superconductor at $x = 0$, the order parameter recovers its bulk value ψ_0 over a distance ξ .

the supercurrent expression (2.19) leads to

$$\nabla^2 \mathbf{B} = \frac{q^2 \mu_0 |\psi|^2}{m^*} \mathbf{B}. \quad (2.20)$$

Again, we consider a semi-infinite superconductor filling the half space $x > 0$, placed in an external magnetic field $\mathbf{B} = B_0 \hat{\mathbf{z}}$, where the z axis is parallel to the surface of the superconductor. The boundary conditions $B(x = 0) = B_0$ and $B(x \rightarrow \infty) = 0$ are satisfied by the magnetic field

$$\mathbf{B}(x) = B_0 e^{-x/\lambda} \hat{\mathbf{z}}, \quad (2.21)$$

where λ is known as the London penetration depth and is defined by

$$\lambda^2 \equiv \frac{m^*}{q^2 \mu_0 |\psi|^2}. \quad (2.22)$$

The London penetration depth characterizes the exponential decay of the magnetic field inside the superconductor (Figure 2.4). Thus, the longer the penetration depth, the lower the energy exerted by the superconductor to expel the external magnetic field.

In sum, the coherence length and the penetration depth govern the spatial variation of the complex order parameter and the magnetic field inside the superconductor, respectively. Their dimensionless ratio $\kappa = \lambda/\xi$ —known as the GL parameter—characterizes the energy cost of forming a superconductor-normal interface. For each interface, the density of Cooper pairs is suppressed over a distance ξ , resulting in an energy loss proportional to ξf_C . As for the magnetic field, it decays exponentially inside the superconductor, thereby

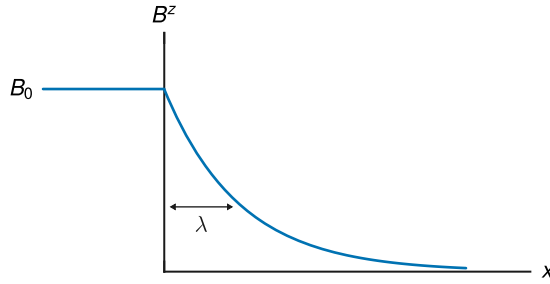


Figure 2.4 | The London penetration depth λ . Starting from the surface of the superconductor at $x = 0$, the magnetic field decays exponentially over a distance λ .

reducing the energy required for field expulsion and, thus, resulting in an energy gain λf_C . Accordingly, the net energy per unit area for a superconductor-normal interface takes the form

$$\gamma \propto (\lambda - \xi) f_C. \quad (2.23)$$

On the one hand, in the limit $\xi \gg \lambda$, superconductor-normal interfaces cost energy, and the material prefers to be either fully superconducting or fully normal. This behavior is classified as type I superconductors. On the other hand, in the limit $\lambda \gg \xi$, the superconductor gains energy by forming an interface. The favorable formation of superconductor-normal interfaces gives rise to the Abrikosov vortex lattice [100], a signature of type II superconductors. Generally, based on the ratio κ , superconductors are classified into type I with $\kappa < 1/\sqrt{2}$ and type II with $\kappa > 1/\sqrt{2}$ [4].

2.2.2 Temperature dependence of length scales

The temperature dependence of the coherence length and the penetration depth follows that of the expansion coefficients α and β . Explicitly, the coherence length can be written as

$$\xi(t) = \frac{\xi(0)}{(1-t)^{1/2}}, \quad (2.24)$$

where $t = T/T_c$ is the reduced temperature. Up to a factor of order unity, the zero-temperature coherence length $\xi(0)$ is related to the physical size of a Cooper pair, known as the Pippard coherence length. According to the BCS

2. Theoretical Background

theory, the Pippard coherence length ξ_0 is defined as

$$\xi_0 = \frac{\hbar v_F}{\pi \Delta(0)}, \quad (2.25)$$

where v_F is the Fermi velocity, and $\Delta(0)$ is the superconducting energy gap at zero temperature.

In addition to the coherence length and the penetration depth, a superconductor is characterized by a third length scale, namely the mean free path ℓ . If the mean free path is much longer than the Pippard coherence length ($\ell \gg \xi_0$), the superconductor is in the *clean* limit. If, however, the mean free path is much shorter than the Pippard coherence length ($\ell \ll \xi_0$), the superconductor is in the *dirty* limit. In the dirty limit, electrons move on average a distance ℓ between scattering events. As a consequence, the effective size of a Cooper pair reduces to $\sqrt{\xi_0 \ell}$. In the clean and dirty limits, the temperature dependence of the coherence length takes the form

$$\xi(t) = \begin{cases} 0.74 \frac{\xi_0}{(1-t)^{1/2}} & \text{clean} \\ 0.855 \frac{(\xi_0 \ell)^{1/2}}{(1-t)^{1/2}} & \text{dirty} \end{cases} . \quad (2.26)$$

Similarly, the penetration depth takes the form

$$\lambda(t) = \begin{cases} \frac{\lambda(0)}{[2(1-t)]^{1/2}} & \text{clean} \\ \frac{\lambda(0)}{[2(1-t)]^{1/2}} \left(\frac{\xi_0}{1.33\ell} \right)^{1/2} & \text{dirty} \end{cases} . \quad (2.27)$$

The shorter the mean free path, the higher the ratio κ and the lower the energy cost of a superconductor-normal interface. Therefore, dirty samples are often type II superconductors.

The temperature dependence in equations (2.26) and (2.27) is strictly valid near the critical temperature of the superconductor because it is derived from the first-order Taylor expansion of the coefficients α and β around T_c . To extend

the validity regime of the GL equations well below T_c , I follow an empirical temperature dependence of the superconducting length scales [101, 102]. The coherence length takes the form

$$\xi(t) = \begin{cases} 0.74 \frac{\xi_0}{\sqrt{p(t)}} & \text{clean} \\ 0.855 \frac{(\xi_0 \ell)^{1/2}}{\sqrt{p(t)}} & \text{dirty} \end{cases} . \quad (2.28)$$

Likewise, the penetration depth takes the form

$$\lambda(t) = \begin{cases} \frac{\lambda(0)}{\sqrt{2}} \sqrt{\frac{g(t)}{p(t)}} & \text{clean} \\ \frac{\lambda(0)}{\sqrt{2}} \sqrt{\frac{g(t)}{p(t)}} \left(\frac{\xi_0}{1.33\ell} \right)^{1/2} & \text{dirty} \end{cases} . \quad (2.29)$$

The thermal kernels $p(t)$ and $g(t)$ are defined by

$$p(t) \equiv \frac{1-t^2}{1+t^2}, \quad (2.30)$$

and

$$g(t) \equiv (1+t^2)^{-2}. \quad (2.31)$$

2.2.3 Flux states of a superconducting ring

As an illustrative example of the time-independent GL equations, I consider a superconducting ring of radius R in a uniform magnetic field, perpendicular to the plane of the ring. I assume that the thickness and the width of the ring are much smaller than the coherence length so that variations of the order parameter along the cross section are negligible, and the model is effectively one-dimensional. The free-energy density (2.9) reduces to

$$f = f_s - f_n = \frac{1}{2m^*} \left| \left(-\frac{i\hbar}{R} \frac{d}{d\theta} - qA \right) |\psi| e^{i\chi} \right|^2 - |\alpha| |\psi|^2 + \frac{\beta}{2} |\psi|^4, \quad (2.32)$$

where the magnetic field term has been dropped since it is much smaller than the kinetic energy for a ring of small cross section [4].

In a uniform magnetic field, the magnitude of the order parameter exhibits cylindrical symmetry ($d|\psi|/d\theta = 0$, where θ is the azimuthal coordinate). To satisfy the periodic boundary conditions, the phase χ increases linearly along the circumference of the ring with a slope n , denoting the phase winding number or the flux state of the ring. As a function of the phase winding number, the free-energy density takes the form

$$f = \frac{\hbar^2}{2m^*R^2} \left| \left(n - \frac{2\pi R}{\Phi_0} A \right) |\psi| e^{i\chi} \right|^2 - |\alpha| |\psi|^2 + \frac{\beta}{2} |\psi|^4, \quad (2.33)$$

where A is the azimuthal component of the vector potential. The flux enclosed within the loop can be written as

$$\Phi = \oint \mathbf{A} \cdot d\mathbf{l} = 2\pi R \times A, \quad (2.34)$$

where $d\mathbf{l}$ is along the azimuthal direction. Substituting with the normalized flux $\phi \equiv \Phi/\Phi_0$ leads to the free-energy density

$$f = \frac{\hbar^2}{2m^*R^2} \left| (n - \phi) |\psi| e^{i\chi} \right|^2 - |\alpha| |\psi|^2 + \frac{\beta}{2} |\psi|^4. \quad (2.35)$$

Defining the superfluid velocity v_s as

$$v_s \equiv \frac{\hbar}{m^*R} (n - \phi), \quad (2.36)$$

the free-energy density simplifies to

$$f = \frac{1}{2}m^*v_s^2|\psi|^2 - |\alpha||\psi|^2 + \frac{\beta}{2}|\psi|^4, \quad (2.37)$$

where the first term represents the kinetic energy. Minimizing the free-energy density with respect to the magnitude $|\psi|$ leads to the equilibrium state

$$|\psi|^2 = \frac{1}{\beta} \left(|\alpha| - \frac{1}{2}m^*v_s^2 \right), \quad (2.38)$$

and the corresponding free-energy density

$$f = -\frac{|\alpha|^2}{2\beta} \left(1 - \frac{m^*v_s^2}{2|\alpha|} \right)^2. \quad (2.39)$$

Recalling the definition of the condensation energy (2.6), we can reformulate the free-energy density into

$$f = -f_C \left[1 - \frac{\xi^2}{R^2}(n - \phi)^2 \right]^2. \quad (2.40)$$

Integrating over the volume V of the ring gives the total free energy

$$F = -F_C \left[1 - \frac{\xi^2}{R^2}(n - \phi)^2 \right]^2, \quad (2.41)$$

where $F_C = (B_{\text{cth}}^2/2\mu_0)V$ is the total condensation energy of the ring. The local minima of the free energy coincide with flux values equal to an integer multiple of the flux quantum Φ_0 (Figure 2.5).

The order parameter at the local minima of the free energy takes the form

$$\frac{\psi}{|\psi_0|} = \left[1 - \frac{\xi^2}{R^2}(n - \phi)^2 \right]^{1/2} e^{in\theta}. \quad (2.42)$$

For a transition between two states with a different winding number n , the phase of ψ must abruptly change by an integer multiple of 2π at a point where the magnitude $|\psi|$ equals zero. As an analogy, the order parameter of the ring can be perceived as a rope whose two ends are interconnected so that it forms a closed loop. The state of the rope can be described by the number of knots in it. For example, a rope with one knot is in the state $n = 1$. Because the rope

2. Theoretical Background

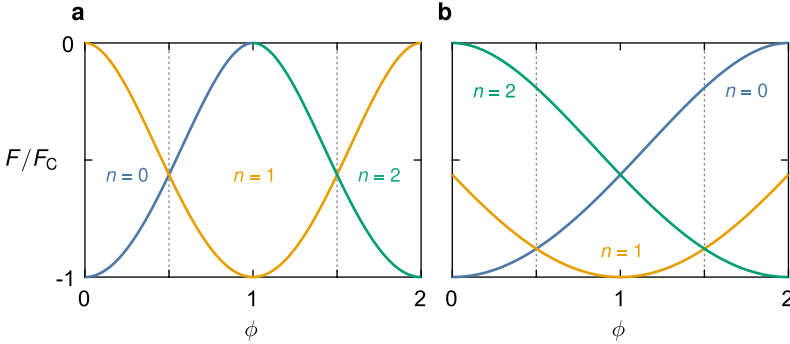


Figure 2.5 | Free energy of one-dimensional superconducting rings enclosing a magnetic flux $\Phi = \phi\Phi_0$, where Φ_0 is the flux quantum. The integer n characterizes the flux state of the ring. The free energy is normalized by the condensation energy F_C . The radii of the rings $R = \xi$ (a) and $R = 2\xi$ (b), where ξ is the GL coherence length.

forms a closed loop, one cannot untie this knot. To change the number of knots, however, one must cut the rope, untie the knot, then reconnect the two ends to recover the closed loop. Thus, the state of the rope cannot be changed without cutting it at one point. Likewise, to change the phase winding number of a superconducting ring, the density of Cooper pairs must be locally destroyed so that the phase can change by an integer multiple of 2π .

In sum, a transition between flux states entails breaking the cylindrical symmetry of the ring. In the absence of fluctuations, due to either noise or defects, the minima of the free energy are stable, and transitions between them are forbidden. In the following chapters, however, I demonstrate that transitions between different winding numbers n are possible either deterministically in the presence of fluctuations by increasing the current to a critical value, or stochastically via thermal activation over or tunneling through an energy barrier. Accordingly, states in the form (2.42) are generally referred to as metastable flux states.

2.2.4 Time-dependent Ginzburg-Landau equations

In its original time-independent form, the Ginzburg-Landau theory has successfully explained a wide range of phenomena in superconductors such as flux quantization [103, 104], superconducting fluctuations [105], and the Abrikosov vortex lattice [100]. Moreover, the GL approach is more general than the microscopic BCS theory since it applies to exotic superconductors where the pairing mechanism is not fully understood (e.g., high-temperature cuprate superconductors [106, 107]).

The Ginzburg-Landau equations are, however, stationary. Therefore, they cannot capture the dynamics and the temporal evolution of the complex order parameter in response to time-varying electromagnetic fields. In 1966, Schmid proposed an extension of the GL equations [108], referred to as the time-dependent Ginzburg-Landau (TDGL) equations. Although Schmid's proposal was only phenomenological, Gor'kov and Éliashberg provided a microscopic justification in the limit of gapless superconductors or materials with magnetic impurities [109]. To extend the validity of Schmid's proposal, Kramer and Watts-Tobin introduced the generalized time-dependent Ginzburg-Landau equations, accounting for the presence of an energy gap [110, 111]. Yet, the TDGL equations remain a versatile, widely used tool for studying various dynamic processes in superconductors, and their predictions agree well with experiments even for gapped superconductors [112–114]. Based on their success in describing vortex dynamics and phase-slip phenomena [102, 115–123], I use the TDGL equations to study the effect of a bias voltage on deterministic and stochastic transitions between metastable flux states of superconducting rings.

The time-dependent Ginzburg-Landau equation takes the form

$$\frac{\hbar^2}{2m^*D} \left(\frac{\partial}{\partial t} + \frac{iq}{\hbar} V \right) \psi + \frac{1}{2m^*} (-i\hbar\nabla - q\mathbf{A})^2 \psi - |\alpha|\psi + \beta|\psi|^2 \psi = 0, \quad (2.43)$$

where D is the diffusion coefficient ($D = \ell v_F/3$), and V is the electrostatic potential [124]. To include the contribution of the normal electrons, Ampere's law is rewritten as

$$\frac{1}{\mu_0} \nabla \times \nabla \times \mathbf{A} = \mathbf{J}_s + \mathbf{J}_n, \quad (2.44)$$

2. Theoretical Background

where the normal-current density \mathbf{J}_n is given by

$$\mathbf{J}_n = -\sigma_n \left(\nabla V + \frac{\partial \mathbf{A}}{\partial t} \right), \quad (2.45)$$

with σ_n as the conductivity of the normal state. The supercurrent density \mathbf{J}_s is defined in equation (2.15).

For convenience, I cast the TDGL equations in a dimensionless form. The order parameter is scaled by its equilibrium value $|\psi_0|$, the space coordinate by the penetration depth λ , and the time coordinate by the ratio ξ^2/D . This transformation is detailed in Appendix A. Substituting with the normalized quantities results in the TDGL equations

$$\left(\frac{\partial}{\partial t} + i\kappa V \right) \psi = - \left(\frac{i}{\kappa} \nabla + \mathbf{A} \right)^2 \psi + (1 - |\psi|^2) \psi, \quad (2.46)$$

and

$$\nabla \times \nabla \times \mathbf{A} = \frac{1}{2i\kappa} (\psi^* \nabla \psi - \psi \nabla \psi^*) - |\psi|^2 \mathbf{A} - \sigma \left(\nabla V + \frac{\partial \mathbf{A}}{\partial t} \right). \quad (2.47)$$

In this form, a superconductor is characterized by two quantities: the GL parameter $\kappa = \lambda/\xi$ and the dimensionless conductivity σ , given by

$$\sigma = \mu_0 D \kappa^2 \sigma_n. \quad (2.48)$$

2.3 Model of a superconducting ring

This section presents the model of a superconducting ring placed in an external magnetic field. The magnetic field comes in two flavors: a uniform field covering all space and a local field confined to a solenoid core piercing the ring. The difference between these two configurations is extensively discussed in Appendix B. The details of the numerical solution of the time-dependent Ginzburg-Landau equations are given in Appendix C. This section, however, highlights the main elements of the numerical solution and presents an example of an unbiased superconducting ring.

In general, I consider a superconducting ring of radius R , width w , and thickness d (Figure 2.6). For a thin-film superconductor, the thickness is much smaller than the coherence length and the penetration depth ($d \ll \xi, \lambda$). As a consequence, the order parameter can be assumed constant along the thickness of the ring, and the supercurrent has no z -component [4, 125]. Thus, the model reduces to a two-dimensional superconductor.

To study the time evolution of the Cooper-pair density in the ring in response to an external magnetic field, I numerically solve the TDGL equations. These equations are commonly solved in two different gauges. First, in the zero-scalar-potential gauge ($V = 0$), I solve the second GL equation

$$\sigma \frac{\partial \mathbf{A}}{\partial t} = \frac{1}{2i\kappa} (\psi^* \nabla \psi - \psi \nabla \psi^*) - |\psi|^2 \mathbf{A} - \nabla \times \nabla \times \mathbf{A}, \quad (2.49)$$

self-consistently with the first GL equation (2.46) for the vector potential \mathbf{A} and the complex order parameter ψ , respectively. An example of this gauge choice is discussed in Appendix C.3.

Second, in the Coulomb gauge ($\nabla \cdot \mathbf{A} = 0$), I solve the first GL equation (2.46) with the continuity equation of the total current density ($\nabla \cdot \mathbf{J} = 0$). This gauge choice is more convenient in the presence of a bias voltage that specifies the scalar potential along the outer perimeter of the ring. The TDGL equations in the Coulomb gauge have been used extensively in literature to study vortex dynamics and phase slips in thin, superconducting films [102, 116–119, 126, 127]. Accordingly, it is the main gauge of choice in this thesis.

2. Theoretical Background

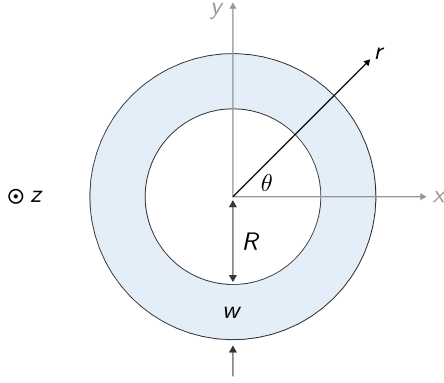


Figure 2.6 | Schematic of a superconducting ring of radius R and width w . Due to the summery of the ring, cylindrical coordinates (r, θ, z) are used.

In short, I solve the two equations

$$\frac{\partial \psi}{\partial t} = -i\kappa V \psi - \left(\frac{i}{\kappa} \nabla + \mathbf{A} \right)^2 \psi + (1 - |\psi|^2) \psi, \quad (2.50)$$

and

$$\sigma \nabla^2 V = \nabla \cdot \mathbf{J}_s = \nabla \cdot \left[\frac{1}{2i\kappa} (\psi^* \nabla \psi - \psi \nabla \psi^*) - |\psi|^2 \mathbf{A} \right], \quad (2.51)$$

for the order parameter ψ and the scalar potential V , with two boundary conditions. First, along the azimuthal direction, the two variables must be periodic. Second, the supercurrent, stemming from the order parameter, must satisfy the Neumann boundary condition at all sample boundaries. In other words, the supercurrent cannot have a component perpendicular to the surface at the boundary. This condition translates to

$$\hat{\mathbf{n}} \cdot \left(\frac{i}{\kappa} \nabla + \mathbf{A} \right) \psi \Big|_{\text{boundary}} = 0, \quad (2.52)$$

where $\hat{\mathbf{n}}$ is a unit vector normal to the sample boundary. Similarly, the normal current cannot leak through the interface; hence,

$$\hat{\mathbf{n}} \cdot \nabla V \Big|_{\text{boundary}} = 0. \quad (2.53)$$

Owing to the symmetry of the ring, I adopt cylindrical coordinates (r, θ, z) . Explicitly, the first GL equation (2.46) reads

$$\frac{\partial \psi}{\partial t} = -i\kappa V\psi - \frac{1}{\kappa^2} \left(\frac{1}{r} \frac{\partial \psi}{\partial r} + \frac{\partial^2 \psi}{\partial r^2} + \frac{1}{r^2} \frac{\partial^2 \psi}{\partial \theta^2} \right) - A^2 \psi - \frac{2iA}{\kappa r} \frac{\partial \psi}{\partial \theta} + (1 - |\psi|^2) \psi, \quad (2.54)$$

where A is the azimuthal component of the vector potential, and the magnetic field is parallel to the z axis. Likewise, the continuity equation (2.51) becomes

$$\left(\frac{1}{r} \frac{\partial}{\partial r} + \frac{\partial^2}{\partial r^2} + \frac{1}{r^2} \frac{\partial^2}{\partial \theta^2} \right) V = \frac{1}{\sigma r} \left[\frac{\partial}{\partial r} (r J_s^r) + \frac{\partial J_s^\theta}{\partial \theta} \right], \quad (2.55)$$

with the azimuthal component of the supercurrent density

$$J_s^\theta = \frac{1}{2i\kappa r} \left(\psi^* \frac{\partial \psi}{\partial \theta} - \psi \frac{\partial \psi^*}{\partial \theta} \right) - |\psi|^2 A, \quad (2.56)$$

and the radial component

$$J_s^r = \frac{1}{2i\kappa} \left(\psi^* \frac{\partial \psi}{\partial r} - \psi \frac{\partial \psi^*}{\partial r} \right). \quad (2.57)$$

The time evolution of the order parameter (2.54) and the Laplacian of the scalar potential (2.55) are solved self-consistently on a numerical grid. I compute the spatial derivative using the finite-difference method and the time evolution using the fourth-order Runge-Kutta method. The numerical solution and the algorithm are detailed in Appendix C. The rest of this chapter discusses an illustrative example of a superconducting ring in a uniform magnetic field.

2.3.1 Example of a one-dimensional superconducting ring

In this example, I examine a superconducting ring in a uniform magnetic field, perpendicular to the plane of the ring. I make a further simplification by assuming the width of the ring to be much smaller than the characteristic length scales (i.e., $w \ll \xi, \lambda$). Consequently, the variation of the order parameter along the radial direction is negligible, and all the vector quantities are along the azimuthal direction. The first TDGL equation (2.54), then, reduces to

$$\frac{\partial \psi}{\partial t} = -i\kappa V\psi - \frac{1}{\kappa^2 R^2} \left(i \frac{\partial}{\partial \theta} + \phi \right)^2 \psi + (1 - |\psi|^2) \psi, \quad (2.58)$$

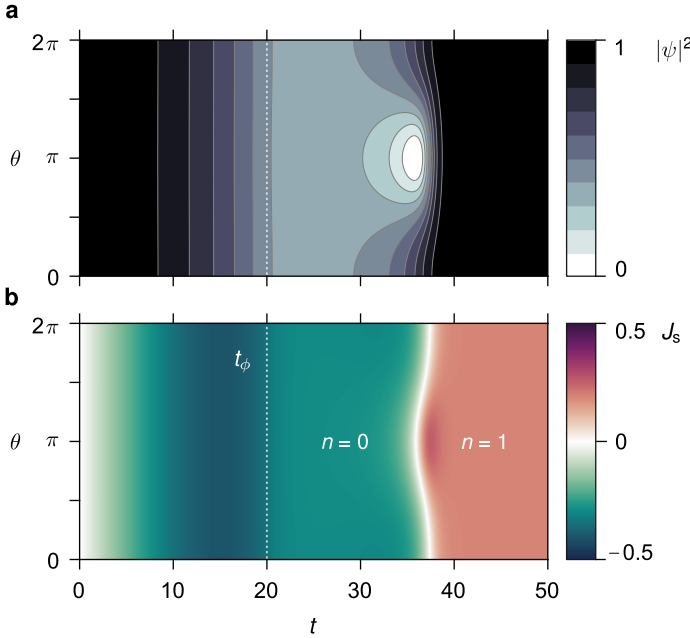


Figure 2.7 | Phase slip in a flux-biased superconducting ring. **a** | Time evolution of the density of Cooper pairs $|\psi|^2$ along the azimuthal direction θ . The density is locally suppressed, and the ring transitions from the flux state $n = 0$ to $n = 1$. **b** | The direction of the supercurrent density J_s changes after the phase slip to complement the external flux. The applied flux is ramped up to $\phi = 4/5$ with a rise time $t_\phi = 20$. Parameters used: $R = \xi = \lambda$ and $\sigma = 1$. All quantities are normalized according to Appendix A.

where the azimuthal component of the vector potential is replaced by the normalized flux enclosed within the loop ($A = \phi/\kappa R$). Likewise, the Laplacian of the scalar potential (2.55) reduces to

$$\frac{\partial^2 V}{\partial \theta^2} = \frac{1}{\sigma \kappa} \frac{\partial}{\partial \theta} \left[\frac{1}{2i} \left(\psi^* \frac{\partial \psi}{\partial \theta} - \psi \frac{\partial \psi^*}{\partial \theta} \right) - \phi |\psi|^2 \right]. \quad (2.59)$$

The numerical solution of these two equations is detailed in Appendix C.2.

I consider a ring of radius $R = \xi = \lambda$, enclosing a magnetic flux $\phi = 4/5$. The ring minimizes its free energy by transitioning from an initial flux state $n = 0$ to $n = 1$. This transition is permitted in the presence of fluctuations, simulated here by incorporating an additive noise term into the right-hand side of the

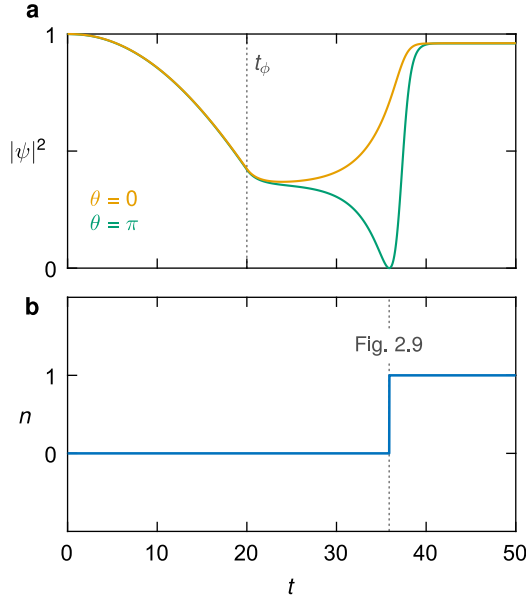


Figure 2.8 | Suppression of the density of Cooper pairs during a phase slip. **a** | Time evolution of the normalized density $|\psi|^2$ along $\theta = 0$ and $\theta = \pi$. **b** | The phase winding number n makes a discontinuous jump when the magnitude $|\psi|$ equals zero. Parameters used: $R = \xi$, $\kappa = 1$, $\sigma = 1$, and the applied flux $\phi = 4/5$ with a rise time $t_\phi = 20$.

first GL equation (2.58). As discussed in Chapter 3, the critical instability point for the transition is $\phi = 1/\sqrt{2}$. Because the applied flux exceeds that value, a phase slip occurs, and the ring transitions to the state $n = 1$ (Figure 2.8b).

This transition occurs in three stages. First, before the external magnetic flux reaches its critical value, a supercurrent is induced owing to the flux quantization requirement. In particular, a clockwise supercurrent flows to produce a magnetic field in the negative z direction, opposing the applied flux (Figure 2.7b). Therefore, the density of Cooper pairs is uniformly reduced in the ring (Figure 2.7a). Second, to change the phase winding number, the magnitude of the order parameter must be locally suppressed so that the phase is ill-defined and can abruptly change by 2π (Figure 2.9). The winding number

$$n = \frac{1}{2\pi} \oint \nabla \chi \cdot d\mathbf{l}, \quad (2.60)$$

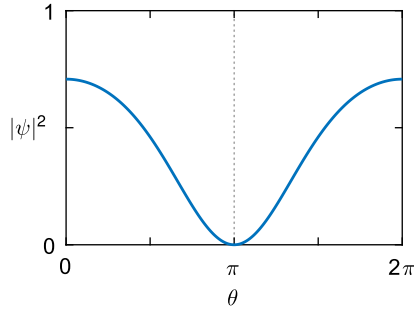


Figure 2.9 | Vortex profile in a superconducting ring. The density of Cooper pairs is plotted along the azimuthal direction θ at the phase slip moment (Figure 2.8).

where $d\mathbf{l}$ is along the azimuthal direction, is therefore incremented by unity. Finally, the Cooper-pair density recovers. But, since the applied flux is a fraction of the flux quantum, the density does not retrieve its equilibrium value, and a counterclockwise supercurrent flows to induce a magnetic field in the positive z direction that augments the applied flux (Figure 2.7b).

The spatial variation of the order parameter for a phase slip incurs energy cost. Consequently, transitions between the flux states $n = 0$ and $n = 1$ are not triggered once the applied flux crosses the degeneracy point $\phi = 1/2$. Particularly, for a transition from the state $n = 0$ to $n = 1$, the external flux must be larger than half a flux quantum ($\phi > 1/2$). For the reverse transition, the external flux must be smaller than half a flux quantum ($\phi < 1/2$). This asymmetry implies the presence of an energy barrier for a phase slip. The next chapter discusses the effect of a bias voltage on a superconducting ring, as a means for electrically modulating this energy barrier.

3

Voltage-Biased Superconductors

The building block of superconducting quantum devices is a link that weakly couples two superconductors. The foremost form of this weak link is the insulating barrier of the Josephson junction. Other forms include a topological insulator [53], a van der Waals heterostructure [54], a two-dimensional electron gas [55], a semiconducting nanowire [56, 57], and a superconducting nanowire [84–86]. In this work, however, I examine the possibility of inducing a weak link electrically in an uninterrupted superconductor to circumvent the need for nanostructuring a weak link. To that end, this chapter assesses the effect of a bias voltage on the density of Cooper pairs in two geometries: superconducting strips and superconducting rings.

This chapter is organized as follows. Section 3.1 analyzes the suppression of the Cooper-pair density in a voltage-biased superconducting strip as a function of the strip length and the parameters of the superconductor using the time-dependent Ginzburg-Landau equations. Next, Section 3.2 focuses on superconducting rings and demonstrates that the bias voltage introduces two weak links, which serve as preferential locations to nucleate phase slips.

3.1 Voltage-biased superconducting strip

Although the primary focus of this chapter is the relation between the bias voltage and the Cooper-pair density in a superconducting ring, this section starts with a simpler configuration, namely a voltage-biased superconducting strip. The conclusions drawn in this section apply to the ring geometry as a ring can be constructed by interconnecting two curved strips. Indeed, the connected geometry of the ring exhibits additional features owing to the quantization of magnetic flux in closed superconducting loops.

I consider a strip of length L and width w , voltage-biased at its two ends, as depicted in Figure 3.1a. The thickness of the strip is assumed much smaller than the coherence length ξ . Therefore, the order parameter does not vary along the z direction, perpendicular to the plane of the strip—that is, the model is two dimensional. To calculate the density of Cooper pairs in a voltage-biased strip, I solve the time-dependent Ginzburg-Landau equation

$$\frac{\partial \psi}{\partial t} = -i\kappa V \psi - \left(\frac{i}{\kappa} \nabla + \mathbf{A} \right)^2 \psi + (1 - |\psi|^2) \psi, \quad (3.1)$$

in the absence of an external magnetic field for the complex order parameter ψ and the scalar potential V self-consistently with the continuity equation

$$\nabla \cdot \mathbf{J}_n = -\nabla \cdot \mathbf{J}_s, \quad (3.2)$$

where \mathbf{J}_n is the normal-current density and \mathbf{J}_s is the supercurrent density. These two equations are solved numerically on a Cartesian grid where the spatial derivatives are computed with the finite-difference method and the time evolution with the fourth-order Runge-Kutta method.

The bias voltage is applied by contacting the strip with two normal-metal electrodes at $x = 0$ and $x = L$ (Figure 3.1a). This setup corresponds to specifying the electrostatic potential V at the two ends (i.e., $V(0) = V_b$ and to $V(L) = 0$). At the normal-superconductor interface, the normal current can convert into supercurrent via two mechanisms. If an incident electron has an energy higher than the superconducting gap $\Delta(T)$, it penetrates the superconductor as a quasiparticle [128]. If, however, its energy is lower than $\Delta(T)$, then there are

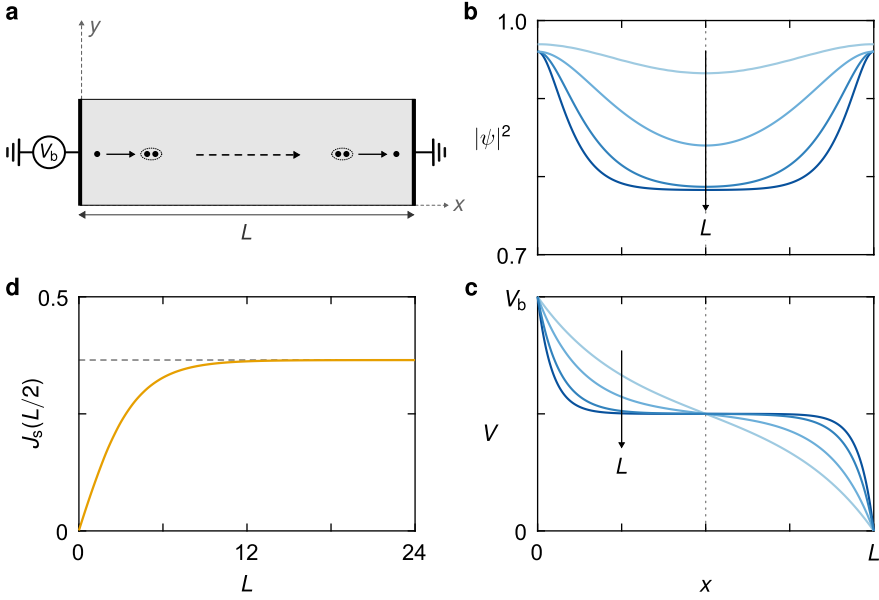


Figure 3.1 | Voltage-biased superconducting strip. **a** | Schematic of a strip of length L subject to a bias voltage V_b applied at the two ends $x = 0$ and $x = L$. The injected normal current at $x = 0$ converts into a supercurrent that flows along the strip. The reverse process occurs at the other electrode. **b** | The density of Cooper pairs $|\psi|^2$ for lengths $L = 4, 8, 16$, and 24 . The arrow indicates the direction of increasing L . **c** | The scalar potential V for various lengths L . **d** | The supercurrent density J_s at the center of the strip as a function of L . Parameters used: $\kappa = 1$, $\sigma = 1$, $V_b = 3/4$, and the strip width $w = 2$. All quantities are cast into a dimensionless form according to Appendix A.

no available electronic states, and the electron must combine with another to form a Cooper pair. Therefore, a total charge of $2e$ is transferred to the superconductor [128]. This process is known as Andreev reflection. These two mechanisms can be modeled within the Ginzburg-Landau framework by imposing the appropriate boundary condition on the order parameter [129]. As the temperature decreases, the gap $\Delta(T)$ increases, and the conversion of normal current into supercurrent via Andreev reflection dominates. In that limit, the order parameter is fixed to its equilibrium value at the interface, and a constant phase difference between the two ends of the strip is imposed according to the bias voltage [129–131]. Close to the critical temperature, however, electrons are injected as quasiparticles inside the superconductor.

3. Voltage-Biased Superconductors

Correspondingly, no supercurrent flows through the interface [129]. This requirement may be achieved either by imposing the Neumann boundary condition at the interface, or by requiring the magnitude of the order parameter to be zero. Both boundary conditions yield a similar behavior, except close to the electrodes where the magnitude of the order parameter recovers over a distance ξ for the latter boundary condition. In practice, however, the density of Cooper pairs does not decay to zero at the interface, but rather penetrates a distance that depends on the metal—for example, if the normal metal is a ferromagnet, then this distance is zero [4]. In the model under consideration, the order parameter satisfies the Neumann boundary condition at all boundaries to ensure that no supercurrent leaks through the interface.

The bias voltage imposes a potential difference between the two ends of the strip, which causes a supercurrent to flow along the y direction. In particular, normal current is injected inside the superconductor via the bias electrode at $x = 0$. The normal electrons, then, convert into Cooper pairs that flow along the longitudinal direction of the strip. The conversion of normal electrons into Cooper pairs is consistent with the incompressibility of the total current density ($\nabla \cdot \mathbf{J} = 0$), which guarantees that the net charge at any point along the strip must be the same and equal in magnitude to the local charge of the positive ionic background [128]. Because the reverse process occurs at the other electrode at $x = L$, the supercurrent reaches its maximum at the center of the strip. In other words, the conversion of supercurrent into normal current at the right electrode inhibits further increase of the supercurrent.

As an example, I consider a strip of length $L = 8$ and width $w = 2$, with the spatial coordinate in units of the penetration depth λ . Because the bias voltage is applied uniformly along the transverse edges of the strip, the supercurrent and the scalar potential exhibit translational symmetry along the y direction. The gradient of the potential equals zero at the center of the strip, implying that the electric field ($\mathbf{E} = -\nabla V$) decays from the interface and reaches zero halfway between the two electrodes (Figure 3.2a). In contrast, the supercurrent is zero at the interface and increases as more normal electrons convert into Cooper pairs. Because the electric field decays to zero, the supercurrent reaches a steady state and does not accelerate to arbitrarily large values.

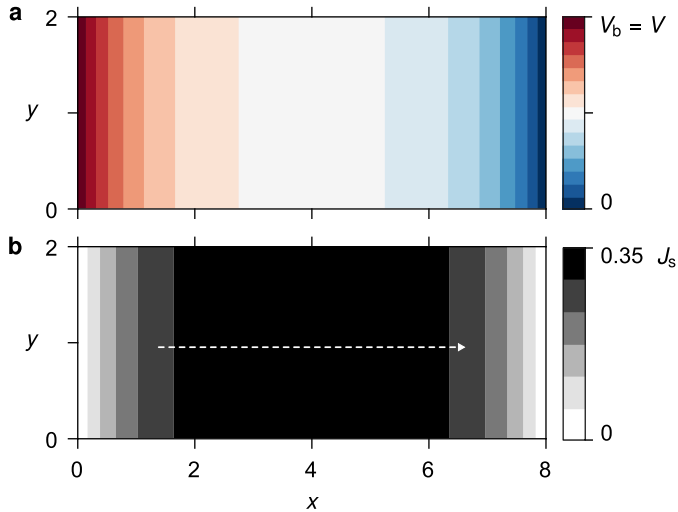


Figure 3.2 | Supercurrent in a voltage-biased strip. **a** | The scalar potential V as a function of the coordinates x and y . The bias voltage fixes the scalar potential to $V = V_b$ at $x = 0$ and to $V = 0$ at $x = L$, where L is the length of the strip (Figure 3.1a). **b** | The supercurrent density J_s as a function of x and y . The arrow indicates the direction of the supercurrent. Parameters used: $\kappa = 1$, $\sigma = 1$, $V_b = 3/4$, $L = 8$, and the strip width $w = 2$. All quantities are normalized according to Appendix A.

The supercurrent density depends on two length scales: the coherence length of the superconductor and the penetration distance of the electric field inside the strip. Specifically, the ratio of these two distances to the length L determines the profile of the supercurrent density. Although the overall current injected in the strip is unchanged for a specific bias voltage, the maximum of the supercurrent increases as a function of L and saturates for a strip much longer than both the coherence length and the penetration distance of the electric field (Figure 3.1d). For a relatively short strip, the layer where normal current converts into supercurrent is not fully developed because the reverse process starts at the other electrode before the normal current decays to zero. Therefore, the supercurrent exhibits a single maximum at the center of the strip. Conversely, for a relatively long strip, the conversion layer is fully developed, and the entire injected current converts into a supercurrent. Furthermore, the electric field decays to zero inside the superconductor and, hence, the supercurrent density flattens halfway between the two bias electrodes (Figure 3.1b).

3. Voltage-Biased Superconductors

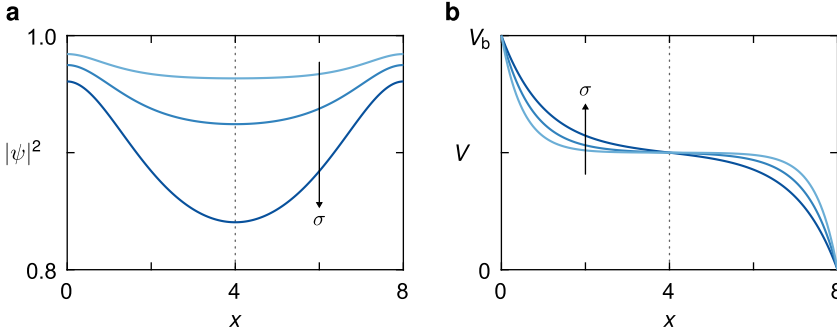


Figure 3.3 | Electric field penetration scales with the normal-state conductivity. **a** | The density of Cooper pairs $|\psi|^2$ along the strip for $\sigma = 1/4, 1/2,$ and 1 , where σ is the normalized conductivity. The arrow indicates the direction of increasing σ . **b** | The scalar potential V as a function of x . Parameters used: $\kappa = 1, V_b = 3/4, L = 8,$ and $w = 2$. All quantities are normalized according to Appendix A.

The penetration of the electric field inside the strip relates to the decay of the quasiparticle charge inside the superconductor, and it depends on the normal-state conductivity σ_n [108], represented here by the normalized conductivity

$$\sigma \equiv \mu_0 \mathcal{D} \kappa^2 \sigma_n. \quad (3.3)$$

The higher the conductivity σ , the deeper the electric field penetrates the superconductor starting from the interfaces at $x = 0$ and $x = L$, in agreement with the microscopic theory predicting that the conversion layer scales with the diffusion coefficient \mathcal{D} [128]. The relation between the normalized conductivity and the penetration of the electric field is better represented by recasting the continuity equation (3.2) in the form

$$\nabla^2 V = -\frac{1}{\sigma} \nabla \cdot \mathbf{J}_s. \quad (3.4)$$

The higher the conductivity σ , the lower the curvature of the electrostatic potential V and, hence, the electric field penetrates deeper inside the superconductor (Figure 3.3b). For arbitrarily large σ , the Laplacian (3.4) is approximately zero, implying that the potential descends linearly between the two electrodes, and that the electric field is uniform inside the strip.

3.2 Voltage-biased superconducting ring

This section examines the temporal and spatial evolution of the Cooper-pair density in a superconducting ring in response to a bias voltage. The following discussion is divided into two parts. First, I consider rings of widths much smaller than the coherence length (i.e., one-dimensional superconducting rings). Second, I consider rings of arbitrary widths, for which the order parameter varies along both the azimuthal and the radial directions.

3.2.1 One-dimensional superconducting rings

This section explores the effect of a bias voltage on a superconducting ring of width $w \ll \xi$. The radial variation of the order parameter is negligible, and all the vector quantities only have an azimuthal component. Nevertheless, the conclusions drawn in this section are valid for the general model depicted in Figure 3.4, as detailed in Section 3.2.2.

The bias voltage is applied along the outer perimeter of the ring. The relative orientation of the two bias electrodes is characterized by the angle α and the arc length of each electrode by the angle γ . This section considers a symmetric configuration for which the bias electrodes fix the electrostatic potential in a one-dimensional ring to $V = 0$ at $\theta = 0$ and to $V = V_b$ at $\theta = \pi$, where θ is the azimuthal angle. Similar to the voltage-biased strip, the imposed potential difference drives two opposite currents along the upper and lower arms of the ring and suppresses the density of Cooper pairs along the circumference of the ring. To determine the supercurrent and the normal-current densities, I numerically solve the time-dependent Ginzburg-Landau equation (2.54) and the continuity equation (2.55) for the complex order parameter ψ and for the scalar potential V , respectively.

For a one-dimensional ring, these two equations can be solved analytically. As usual, the starting point is the time-dependent Ginzburg-Landau (TDGL) equation in its dimensionless form

$$\frac{\partial \psi}{\partial t} = -i\kappa V \psi - \left(\frac{i}{\kappa} \nabla + \mathbf{A} \right)^2 \psi + (1 - |\psi|^2) \psi. \quad (3.5)$$

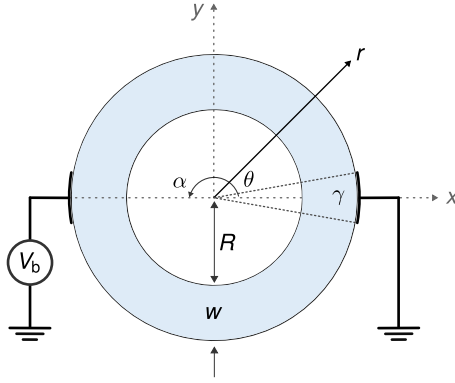


Figure 3.4 | Schematic of a voltage-biased superconducting ring of radius R and width w . The angle between the bias electrodes is denoted by α . The arc length of the electrodes is characterized by the angle γ . Because of the symmetry of the ring, cylindrical coordinates (r, θ, z) are used.

Invoking the polar form

$$\psi = f e^{i\chi}, \quad (3.6)$$

allows to separate the time evolution of ψ into real and imaginary parts, corresponding to the time evolution of the magnitude f and the phase χ , respectively. In the absence of an external magnetic field ($\mathbf{A} = 0$), the real part simplifies to

$$\frac{\partial f}{\partial t} = \frac{1}{\kappa^2} \left[f'' - (\chi')^2 f \right] + f - f^3, \quad (3.7)$$

where $f' \equiv \partial f / \partial x$, and $x \equiv R\theta$ with R denoting the radius of the ring. Likewise, the imaginary part simplifies to

$$\frac{\partial \chi}{\partial t} = -\kappa V + \frac{1}{\kappa^2 f} (2\chi' f' + \chi'' f). \quad (3.8)$$

In the steady state $\partial f / \partial t = 0$, the time evolution of the magnitude reduces to

$$\frac{1}{\kappa^2} f'' - v_s^2 f + f - f^3 = 0, \quad (3.9)$$

where the superfluid velocity is defined as

$$v_s \equiv \frac{\chi'}{\kappa}. \quad (3.10)$$

In the presence of a bias voltage, the phase constantly evolves in time, and its time derivative cannot be set to zero. The superfluid velocity, however, reaches a steady state (i.e., $\partial v_s / \partial t = 0$). Differentiating the time derivative of the phase along x leads to

$$\frac{\partial}{\partial x} \frac{\partial \chi}{\partial t} = \kappa \frac{\partial v_s}{\partial t} = \frac{\partial}{\partial x} \left[-\kappa V + \frac{1}{\kappa^2 f} (2\chi' f' + \chi'' f) \right]. \quad (3.11)$$

Equating the time derivative of the superfluid velocity to zero gives

$$\frac{\partial}{\partial x} \left[-\kappa V + \frac{1}{\kappa f} (2v_s f' + v_s' f) \right] = 0, \quad (3.12)$$

or simply

$$-\kappa V + \frac{1}{\kappa f} (2v_s f' + v_s' f) = C, \quad (3.13)$$

where C is constant along x .

The first TDGL equation is solved self-consistently with the continuity equation of the total current density ($\nabla \cdot \mathbf{J} = 0$). In the one-dimensional model, the continuity equation takes the form

$$\frac{\partial}{\partial x} (v_s f^2) = \sigma \frac{\partial^2 V}{\partial x^2}, \quad (3.14)$$

where σ is the normalized conductivity. Now, the problem reduces to solving the three equations (3.9), (3.13), and (3.14).

For a ring of radius comparable to the coherence length, the magnitude of the order parameter does not vary considerably along the circumference of the ring. Consequently, the derivative of f is negligible, and the derivative of the superfluid velocity simplifies to

$$\frac{\partial v_s}{\partial x} = \kappa C + \kappa^2 V. \quad (3.15)$$

Likewise, dropping the derivative of f in the continuity equation (3.14) gives

$$\frac{\partial v_s}{\partial x} = \sigma \frac{\partial^2 V}{\partial x^2}. \quad (3.16)$$

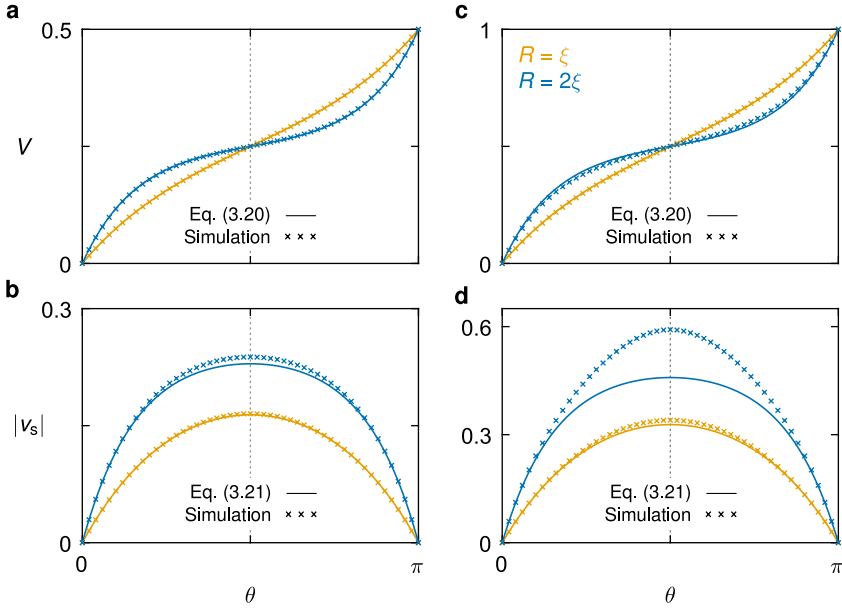


Figure 3.5 | Comparison of analytical and numerical solutions. The analytical (*solid line*) and the numerical (*crosses*) solutions of the scalar potential V and the superfluid velocity v_s as a function of the azimuthal angle θ for a voltage-biased superconducting ring of radius $R = \xi$ and $R = 2\xi$. Parameters used: $\kappa = 1$, $\sigma = 1$, and $V_b = 1/2$ in (a) and (b); $V_b = 1$ in (c) and (d). All quantities are normalized according to Appendix A.

The two equations (3.15) and (3.16) must be solved self-consistently for the electrostatic potential and the superfluid velocity. To evaluate the constant C , I impose the boundary condition

$$v_s'(\theta = 0) = -v_s'(\theta = \pi), \quad (3.17)$$

stemming from the symmetry of the bias voltage. This condition leads to

$$C = -\frac{\kappa}{2} V_b, \quad (3.18)$$

where V_b is the magnitude of the bias voltage (Figure 3.4). Next, substituting with the derivative of the superfluid velocity (3.15) into the continuity equation (3.16) results in

$$\frac{\sigma}{\kappa^2} \frac{\partial^2 V}{\partial x^2} = V - \frac{V_b}{2}. \quad (3.19)$$

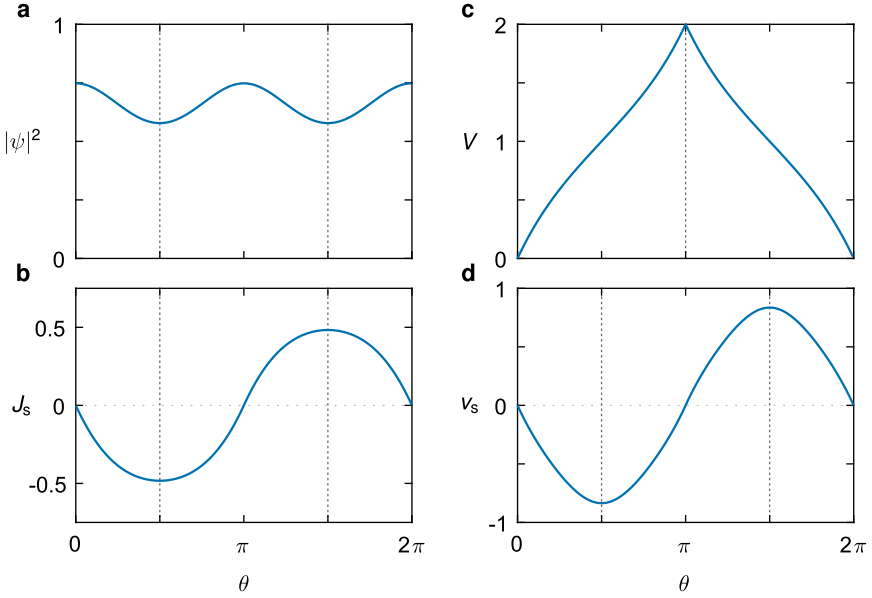


Figure 3.6 | Effect of bias voltage on a superconducting ring. The density of Cooper pairs $|\psi|^2$ (a), the supercurrent density J_s (b), the electrostatic potential V (c), and the superfluid velocity v_s (d) as a function of the azimuth θ . Parameters used: $R = \xi = \lambda$, $\sigma = 1$, and $V_b = 2$. Variables are normalized according to Appendix A.

Because the electrostatic potential is bound by the value of bias defined between the two electrodes, I impose the boundary conditions $V(0) = 0$ and $V(\pi) = V_b$. These two conditions are satisfied by the potential

$$V = \frac{V_b}{2} \left[1 + \frac{e^{\beta\theta} - e^{\beta(\pi-\theta)}}{e^{\beta\pi} - 1} \right], \quad (3.20)$$

where the coefficient $\beta \equiv \kappa R / \sqrt{\sigma}$. Substituting with the potential (3.20) into the continuity equation (3.16) leads to the superfluid velocity

$$v_s = \kappa \sqrt{\sigma} \frac{V_b}{2} \left[\frac{e^{\beta\theta} + e^{\beta(\pi-\theta)}}{e^{\beta\pi} - 1} - \coth\left(\frac{\beta\pi}{2}\right) \right], \quad (3.21)$$

which has a maximum at $\theta = \pi/2$ in the form

$$|v_s(\pi/2)| = \kappa \sqrt{\sigma} \frac{V_b}{2} \tanh\left(\frac{\beta\pi}{4}\right). \quad (3.22)$$

3. Voltage-Biased Superconductors

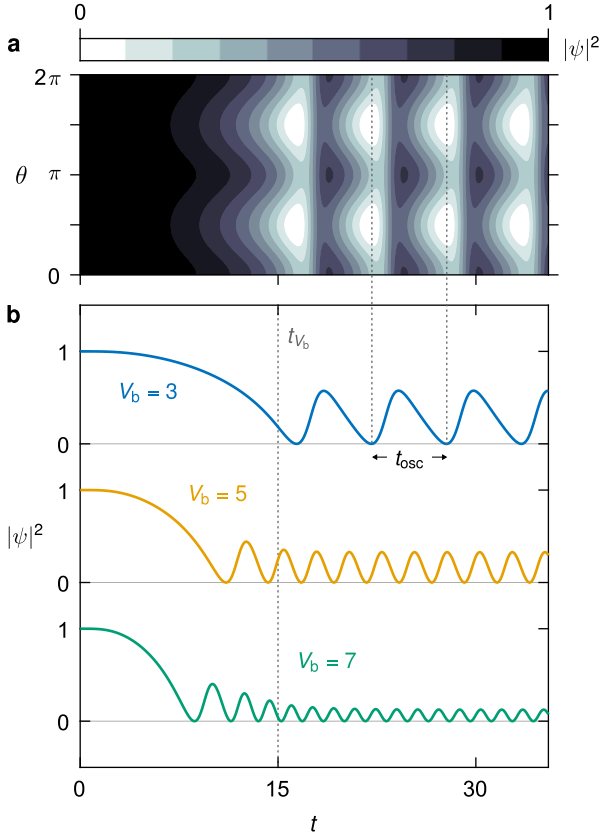


Figure 3.7 | Phase slips in a voltage-biased superconducting ring. a | The Cooper pair density $|\psi|^2$ as a function of time along the azimuthal angle θ for $V_b = 3$. Two phase slips occur at the weak points $\theta = \pi/2$ and $3\pi/2$. **b** | Time evolution of $|\psi|^2$ at $\theta = \pi/2$ for $V_b = 3, 5$, and 7 . The oscillation period t_{osc} decreases as a function of V_b . Parameters used: $R = \xi$, $\kappa = 1$, and $\sigma = 1$. The bias voltage is ramped up to V_b with a rise time $t_{V_b} = 15$. All quantities are normalized according to Appendix A.

To verify the analytical solution, I compare it with the numerical solution for rings of radii $R = \xi$ and $R = 2\xi$ (Figure 3.5). The analytical and the numerical solutions agree for $R = \xi$. But as the bias voltage increases or as the radius increases compared to the coherence length ξ , the derivative of the magnitude f is no longer negligible. Thus, the analytical and the numerical solutions deviate, especially at the maximum of the superfluid velocity.

In general, the bias voltage induces oppositely circulating supercurrents along the upper and lower arms of the ring. The supercurrent density is nonuniform and reaches its maximum at $\theta = \pi/2$ and $\theta = 3\pi/2$ (Figure 3.6b). These two maxima coincide with the minima of the magnitude $|\psi|$ since Cooper pairs are broken due to the acquired kinetic energy (Figure 3.6a).

More important, the minima of the Cooper-pair density serve as phase-slip centers—namely, preferential locations to nucleate phase slips. Specifically, as the bias voltage increases, the density of Cooper pairs is locally suppressed, thereby enforcing two simultaneous phase slips. The phase slips occur momentarily because the superfluid velocity is ill-defined for a vanishing magnitude $|\psi|$ and thus superconductivity nucleates again. Because the bias voltage accelerates Cooper pairs again, another two phase slips occur, and the Cooper-pair density oscillates in time (Figure 3.7a). The oscillation period decreases as a function of the bias voltage (Figure 3.7b). If the bias voltage is high enough to enforce a phase slip in a time shorter than that required to recover the Cooper-pair density, the ring transitions to the normal state. The two simultaneous phase slips at $\theta = \pi/2$ and $\theta = 3\pi/2$ correspond to a vortex–antivortex pair. Therefore, the phase winding number n remains zero at all times, i.e., the initial flux state of the ring is preserved.

3.2.2 Two-dimensional superconducting rings

This section expands the one-dimensional model by considering superconducting rings of arbitrary widths, for which the order parameter varies along the radial and azimuthal directions. The bias electrodes are now along the outer perimeter of the ring (Figure 3.4). Similar to the superconducting strip, the order parameter satisfies the Neumann boundary condition at all boundaries.

For two-dimensional voltage-biased rings, the location of the Cooper-pair density minima depends on the relative ratios of the radius R , the width w , and the coherence length ξ . On the one hand, for a ring of width $w \gg \xi$ and R , most of the supercurrent density is pushed along the radial direction (Figure 3.8c). The minima of the Cooper-pair density are therefore adjacent to the electrodes of the bias voltage. On the other hand, for a ring of radius $R \gg \xi$ and w , the

3. Voltage-Biased Superconductors

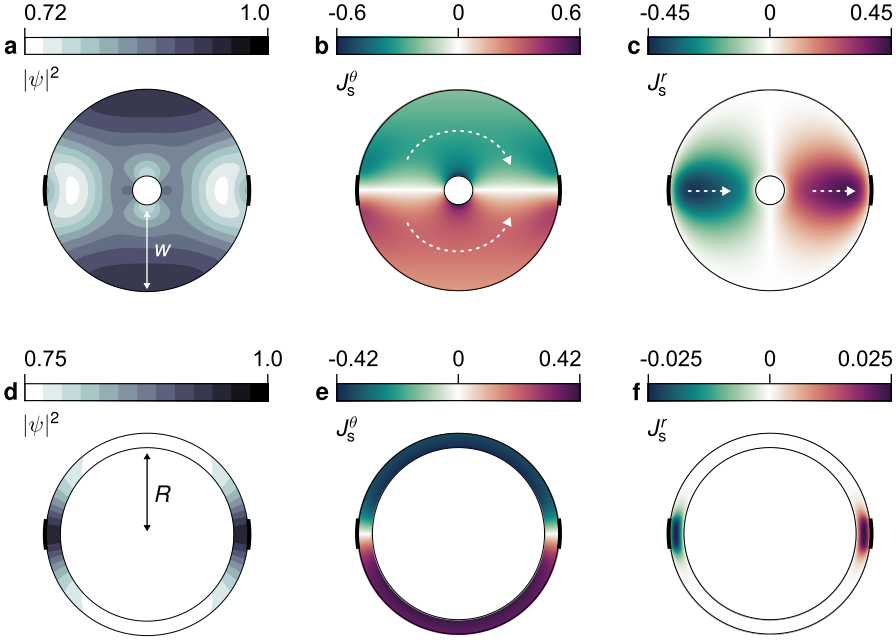


Figure 3.8 | Voltage-biased superconducting rings. The Cooper-pair density (a, d), and the supercurrent density along the azimuthal (b, e) and the radial (c, f) directions for two rings of $R = \xi$ and $w = 6\xi$ (top), and $R = 6\xi$ and $w = \xi$ (bottom). The dashed arrows denote the direction of current. The thick arcs along the outer perimeters represent the bias electrodes. Parameters used: $\kappa = 1$, $\sigma = 1$, and $V_b = 5/2$ (top) and $V_b = 1$ (bottom). All quantities are cast into a dimensionless form according to Appendix A.

radial current density is negligible, and most of the supercurrent is pushed along the azimuthal direction (Figure 3.8e). Because the ring's circumference is much longer than the coherence length, the Cooper-pair density plateaus along the azimuthal direction, resulting in numerous viable phase-slip locations.

To localize two weak points, the radius and the width of the ring must be comparable to the coherence length ξ . For instance, for $R = \xi$ and $w = 3\xi$, the maxima of the azimuthal component of the supercurrent density, or equivalently the minima of the density of Cooper pairs, are along the inner boundary of the ring at $\theta = \pi/2$ and $\theta = 3\pi/2$ (Figure 3.9a), in agreement with the one-dimensional model in Figure 3.6.

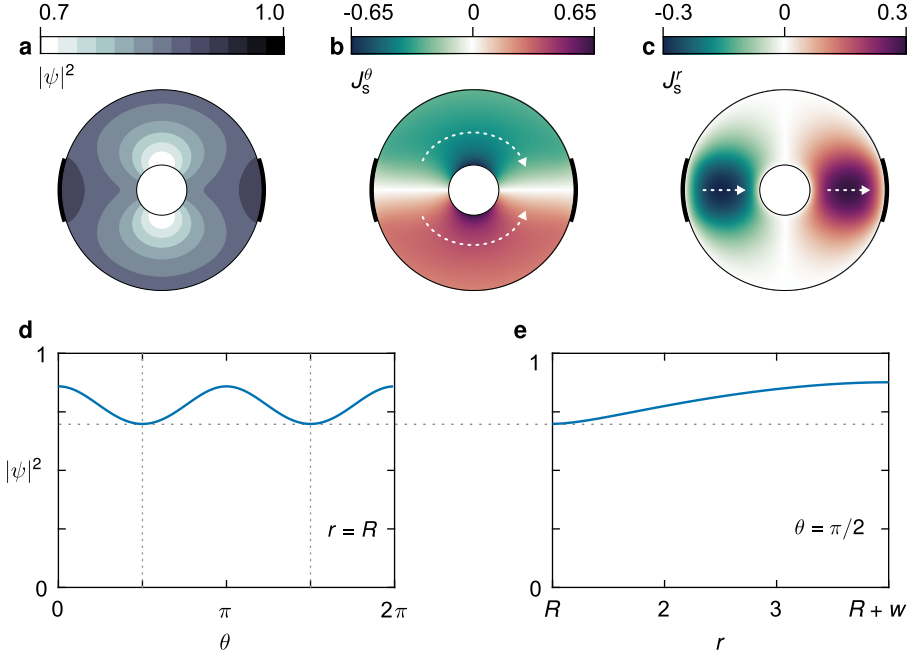


Figure 3.9 | Bias voltage induces two weak points in a superconducting ring of radius $R = \xi$ and width $w = 3\xi$. **a** | The density of Cooper pairs exhibits two minima at $\theta = \pi/2$ and $3\pi/2$ along the inner boundary of the ring. **b, c** | The azimuthal and radial components of the supercurrent density. The dashed arrows serve as a guide for the direction of current. The thick arcs denote the bias electrodes. **d** | The Cooper-pair density along $r = R$ as a function of the azimuthal angle θ . **e** | The Cooper-pair density along $\theta = \pi/2$ as a function of the radial distance r . Parameters used: $\kappa = 1$, $\sigma = 1$, and $V_b = 3/2$. All quantities are cast into a dimensionless form (see Appendix A).

If the bias voltage is high enough to completely suppress the Cooper-pair density at the weak points, two simultaneous phase slips occur in the form of vortices. These vortices nucleate at the minima of the Cooper-pair density at $\theta = \pi/2$ and $\theta = 3\pi/2$ along the inner rim of the ring. The circulating supercurrent exerts a Lorentz force on the nucleated vortices perpendicular to both the axis of the vortices and the direction of the current. As a consequence, the vortices are dragged along the radial direction and ejected from the ring (Figure 3.10b). Once the vortices depart the ring, the whole process repeats again, and the Cooper-pair density oscillates in time.

3. Voltage-Biased Superconductors

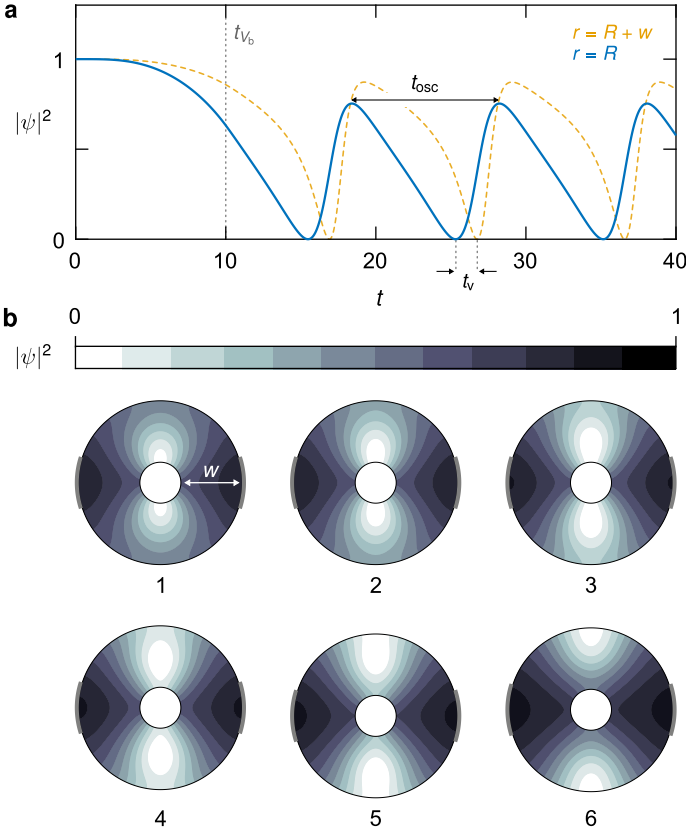


Figure 3.10 | Phase slips in a voltage-biased superconducting ring. a | The density of Cooper pairs $|\psi|^2$ as a function of time at $\theta = \pi/2$ along the inner ($r = R$) and the outer ($r = R + w$) rims of the ring. **b** | The numbers (1-6) denote the sequential evolution of $|\psi|^2$, where two vortices nucleate at the inner rim, then depart the ring. Parameters used: $R = \xi$, $w = 3\xi$, $\kappa = 1$, $\sigma = 1$, $V_b = 5/2$, and $t_{V_b} = 10$. The density $|\psi|^2$ is normalized by its equilibrium value ψ_0 in the absence of bias voltage.

The oscillating density is characterized by two time scales: the period t_{osc} and the vortex-transit time t_v . As its name suggests, the latter denotes the time it takes the vortex to travel from the inner to the outer rim of the ring. Numerically, it is the time difference between two consecutive minima of $|\psi|^2$ at $r = R$ and $r = R + w$ (Figure 3.10a). Similarly, the oscillation period denotes the time difference between two consecutive minima of $|\psi|^2$ at the same

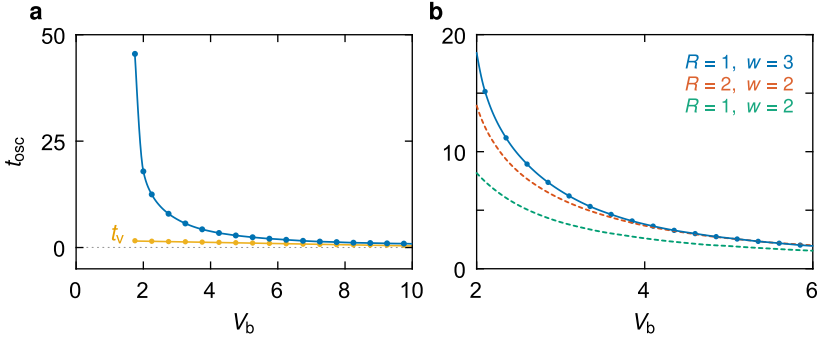


Figure 3.11 | Oscillation period of phase slips as a function of the bias voltage. **a** | The oscillation period t_{osc} and the vortex-transit time t_v are plotted as a function of bias voltage V_b for a ring of $R = \xi$ and $w = 3\xi$. **b** | The oscillation period for various superconducting rings of radii R and widths w . The angle characterizing the arc length of the bias electrode is kept constant for all three rings, consistent with Figure 3.10. All quantities are cast into a dimensionless form (see Appendix A).

location (e.g., at $r = R$). As the bias voltage increases, the oscillation period decreases asymptotically towards the vortex-transit time (Figure 3.11). In the limit $t_{\text{osc}} \approx t_v$, a vortex is nucleated at the inner rim of the ring immediately as the previous one departs through the outer rim. For a ring of width no more than a few multiples of the coherence length, exceeding this limit corresponds to permanently destroying superconductivity in the ring along the vortex path.

To scrutinize the impact of varying the width, I compare two superconducting rings of widths $w = 2\xi$ and 3ξ (Figure 3.11), while fixing the angle γ characterizing the arc length of the bias electrodes. The onset of the oscillations shifts to a lower bias voltage as the width of the ring decreases. To decouple the effect of the inconsistent arc length of the electrodes, an additional superconducting ring of width $w = 2\xi$ and radius $R = 2\xi$ is considered. For a given bias voltage, the oscillation frequency is higher for the smaller width. The effect of varying the width of the ring and the arc length of the bias electrodes is discussed in more detail in Chapter 5.

Despite the oscillations of the Cooper-pair density, the flux state of the ring is preserved because the two simultaneous phase slips correspond to a vortex-

3. Voltage-Biased Superconductors

antivortex pair. In other words, the phase slip in the upper arm of the ring increments the phase winding number n by one, whereas the phase slip in the lower arm decrements n by one. Therefore, the phase winding number

$$n = \frac{1}{2\pi} \oint \nabla\chi \cdot d\mathbf{l}, \quad (3.23)$$

where $d\mathbf{l}$ is a differential length along the outer circumference of the ring, does not change, and the ring remains in the flux state $n = 0$. In the following chapters, I break the symmetry between the vortex and the antivortex by including an external magnetic field that threads the superconducting ring. This asymmetry enables the ring to trigger deterministic transitions to subsequent flux states. The next chapter explores how the bias voltage affects the dynamics of those deterministic transitions.

4

Deterministic Transitions between Flux States

The pioneering work of Doll and Näbauer, and Deaver and Fairbank revealed that the magnetic flux enclosed by a superconducting ring is quantized [103, 104]. When a superconducting ring is placed in an increasing magnetic field, it transitions between discrete flux states to minimize its energy. Using the time-dependent Ginzburg-Landau equations, this chapter explores the effect of a bias voltage on the dynamics of these transitions. The central finding of this chapter is that the bias voltage modulates the critical flux at which a deterministic transition to the subsequent flux state occurs, or equivalently it modulates the free-energy barrier separating the discrete flux states of the ring. To demonstrate the practicality of this result, I propose a voltage-controlled superconducting memory whose state is encoded by the absence or presence of a single flux quantum within the ring.

This chapter is organized as follows. Section 4.1 identifies the critical magnetic flux for deterministic phase slips in an unbiased superconducting ring. The reduction of the critical flux due to a bias voltage is examined in Section 4.2, demonstrating monotonic decrease of the critical flux as the bias voltage increases. Based on the electronic manipulation of deterministic phase slips, in Section 4.3, I propose a superconducting memory whose state is read and written via bias-voltage pulses in the order of picoseconds.

4.1 Critical flux for a deterministic phase slip

For a superconducting ring to transition between its discrete flux states, the phase of the complex order parameter changes by an integer multiple of 2π at a point where the magnitude is suppressed, an event known as a phase slip. If an ideal ring is placed in a uniform magnetic field, the magnitude of the order parameter is also uniform, and a phase slip cannot nucleate. Initiating a phase slip, therefore, requires a nonuniform perturbation (e.g., a bias voltage). In practice, small fluctuations—due to noise or inhomogeneities in the ring—can initiate the change of the order parameter along the azimuthal direction. If the ring is in a stable flux state, these fluctuations average out to zero, and no transition occurs. Conversely, if the flux state is unstable, then fluctuations grow and trigger a phase slip (i.e., a transition to an adjacent flux state). This section defines the instability criteria required for a such deterministic transition, known as the Eckhaus instability [132–134].

4.1.1 Critical current for a one-dimensional superconductor

The normalized magnitude of the complex order parameter of a uniform one-dimensional superconductor is expressed as

$$|\psi|^2 = 1 - v_s^2, \quad (4.1)$$

where v_s is the superfluid velocity. The supercurrent density takes the form

$$J_s = v_s |\psi|^2 = v_s (1 - v_s^2). \quad (4.2)$$

At small velocities, the supercurrent density increases linearly as a function of v_s . The velocity increase is accompanied by a reduction of the density of Cooper pairs, which inhibits further increase of the supercurrent (Figure 4.1a). Maximizing the supercurrent density (4.2) leads to

$$\frac{\partial J_s}{\partial v_s} = 0 = 1 - 3v_s^2. \quad (4.3)$$

The critical superfluid velocity v_s^c equals $1/\sqrt{3}$, and the critical supercurrent density J_s^c equals $2/\sqrt{27}$, known as the pair-breaking or depairing current, imposed by the breaking of Cooper pairs with the acquired kinetic energy.

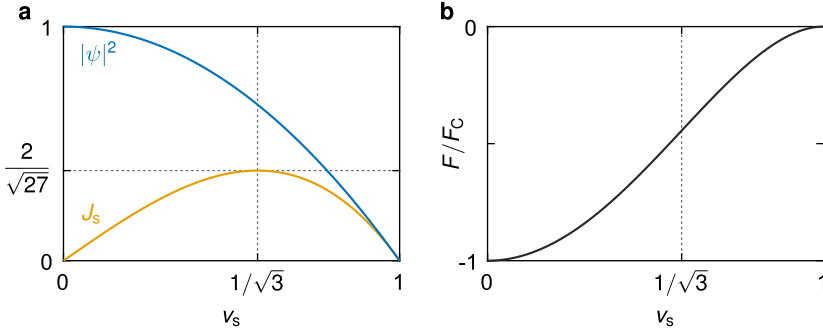


Figure 4.1 | Depairing critical current density. **a** | The squared magnitude of the order parameter $|\psi|^2$ (blue) and the supercurrent density (orange) are plotted as a function of the superfluid velocity v_s . The horizontal dotted line denotes the depairing critical current density. **b** | Free energy, normalized by the condensation energy F_C , for a one-dimensional superconductor as a function of v_s .

The free energy of the superconductor has an inflection point at the critical superfluid velocity (Figure 4.1b), which implies that further increase in the velocity results in a relatively lower increase in the free energy. The next section determines this critical superfluid velocity for a one-dimensional superconducting ring in the presence of fluctuations.

4.1.2 Eckhaus instability

In the presence of a uniform external magnetic field, the time-independent Ginzburg-Landau equation is satisfied by the plane waves

$$\psi_n = |\psi| e^{i\chi} = \sqrt{1 - v_s^2} e^{in\theta}. \quad (4.4)$$

These states are the local minima of the free energy and are metastable because transitions to states with different winding numbers n can occur via either deterministic or stochastic phase slips. The purpose of this section is to specify the point at which a metastable state becomes unstable in the presence of fluctuations. The derivation of the instability criterion is presented in detail in Appendix D. Here, however, I outline the stability analysis through an instructive example. To that end, I consider the time-evolution equation

$$\frac{dx}{dt} = x - x^2, \quad (4.5)$$

4. Deterministic Transitions between Flux States

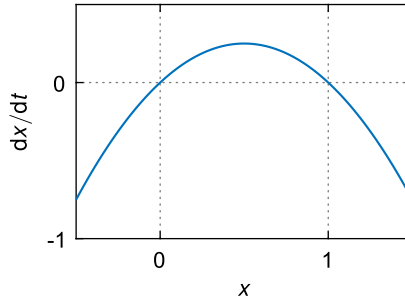


Figure 4.2 | Example of linear stability analysis. The vertical lines correspond to the two stationary solutions of the time-evolution equation (4.5).

which has two stationary solutions—namely, $x_s = 0$ and $x_s = 1$ —analogous to the stationary metastable states that satisfy the time-independent GL equation. To assess the stability of a stationary solution in the presence of fluctuations δ , we expand the variable x as

$$x = x_s + \delta, \quad (4.6)$$

up to first order in the fluctuations δ . The time evolution of x , then, reads

$$\frac{dx}{dt} = \frac{d\delta}{dt} = (x_s + \delta) - (x_s + \delta)^2. \quad (4.7)$$

To judge the stability of a solution, we cast the equation in the form

$$\frac{d\delta}{dt} = \frac{de^{\epsilon t}}{dt} = \epsilon\delta, \quad (4.8)$$

and solve for the eigenvalue ϵ . If the eigenvalue ϵ is positive, fluctuations grow in time, implying an unstable solution. If it is negative, fluctuations decay, implying a stable solution. For the solution $x_s = 0$ and ignoring nonlinear terms in the limit of weak fluctuations, the time evolution (4.7) reduces to

$$\frac{d\delta}{dt} = \delta. \quad (4.9)$$

The eigenvalue ϵ is equal to 1, and the system is linearly unstable. In contrast, for the stationary solution $x_s = 1$, the time evolution reduces to

$$\frac{d\delta}{dt} = -\delta. \quad (4.10)$$

The eigenvalue ϵ is equal to -1 , and the system is linearly stable.

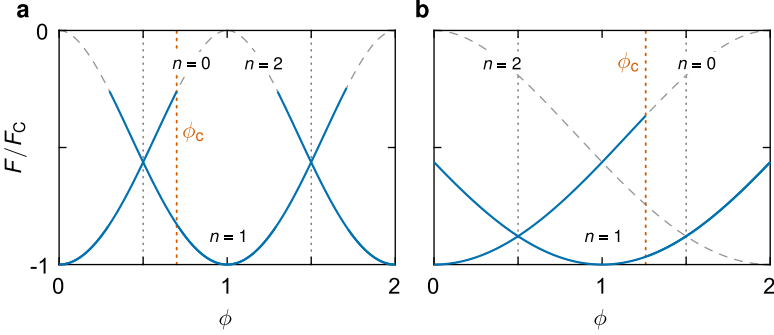


Figure 4.3 | Critical flux for a deterministic phase slip. The free energy, normalized by the condensation energy F_C , as a function of the flux ϕ for rings of radii $R = \xi$ (a) and $R = 2\xi$ (b). The analytical expression (4.11) of the critical flux ϕ_c agrees with the numerical solution of the TDGL equations. The dashed lines correspond to the solution of the time-independent GL equation in Figure 2.5. Parameters used: $\kappa = 1$ and $\sigma = 1$.

The stability of the two solutions can be verified by plotting the derivative (4.5) as a function of x (Figure 4.2). Close to the solution $x_s = 1$, if fluctuations slightly increase x , the time derivative becomes negative, and x evolves back to the stationary point x_s . Likewise, if fluctuations slightly decrease x , the time derivative becomes positive, and x evolves back to x_s . Accordingly, this solution is characterized as linearly stable. Conversely, close to the solution $x_s = 0$, if x is increased, its time derivative becomes positive, and it continues to increase—that is, fluctuations grow, and the solution is linearly unstable.

Following the linear-stability analysis, the point at which fluctuations of the order parameter ψ , due to noise or sample defects, grow to nucleate a phase slip is derived in Appendix D. For a ring of radius R whose width and thickness are much smaller than the coherence length ξ , the critical flux for a deterministic transition from the flux state $n = 0$ to $n = 1$ is given by [132–134]

$$\phi_c = \frac{1}{\sqrt{3}} \frac{R}{\xi} \sqrt{1 + \frac{\xi^2}{2R^2}}. \quad (4.11)$$

For instance, for a radius $R = 1$, the critical flux ϕ_c equals $1/\sqrt{2}$, in agreement with the numerical solution of the time-dependent GL equations (Figure 4.3a). In the absence of a nonuniform perturbation, such as a bias voltage, the superfluid velocity and the magnitude of the order parameter are uniform

4. Deterministic Transitions between Flux States

along the circumference of the ring, apart from infinitesimal wiggles due to the numerically imposed noise. Consequently, the location of the phase slip is random and occurs at a point where the imposed random noise is strongest, corresponding to the minimum of the magnitude $|\psi|$. In terms of the superfluid velocity, the instability takes the form

$$v_s^c = \frac{1}{\sqrt{3}} \sqrt{1 + \frac{\xi^2}{2R^2}}. \quad (4.12)$$

For an infinitely large ring, the critical superfluid velocity reduces to that of an infinite one-dimensional wire, namely $v_s^c = 1/\sqrt{3}$. The next section discusses how the bias voltage modulates the critical flux ϕ_c .

4.2 Reduction of critical flux by bias voltage

This section evaluates the critical flux for deterministic transitions between the flux states of a voltage-biased superconducting ring. For a ring enclosing a half-integer multiple of the flux quantum, the bias voltage reduces critical flux to the degeneracy point $\phi = n + 1/2$, implying that the free-energy barrier separating the two states n and $n + 1$ is completely suppressed. In that limit, the ring reaches a dynamic equilibrium oscillating between these two states.

4.2.1 Instability criterion in the presence of bias voltage

The bias voltage induces two weak links in the superconducting ring, serving as preferential locations to nucleate phase slips. In the presence of a flux bias ϕ , the location of phase slips depends on the sum of the current driven by the bias voltage and the current driven by the flux ϕ . For example, at $\phi = 1/2$ and in the flux state $n = 0$, a clockwise current flows to oppose the external flux. As a consequence, the current driven by the bias voltage and the current driven by the external flux interfere constructively in the upper arm of the ring and destructively in the lower one. Accordingly, the Cooper-pair density has a single global minimum at the maximum of the supercurrent—that is, at $\theta = \pi/2$. This minimum determines the location of the phase slip. Conversely, in the flux state $n = 1$, the persistent current changes direction, and the constructive interference occurs in the lower arm of the ring, which shifts the location of the phase slip to $\theta = 3\pi/2$. To sum up, the location of phase slips alternates based on the flux state n because the minimum of the Cooper-pair density depends on the sum of the current induced by the bias voltage and the current induced by the flux bias enclosed within the ring (Figure 4.7).

What's more, because of the current induced by bias voltage, deterministic phase slips require a lower flux. Put differently, the hysteresis of the free-energy spectrum is reduced (Figure 4.4a). To inspect the reduction of the critical flux as a function of the bias voltage, I assume that the linear-instability analysis holds for a voltage-biased ring. Next, I decompose the superfluid velocity into

$$v_s = v_s^b + v_s^\phi, \quad (4.13)$$

4. Deterministic Transitions between Flux States

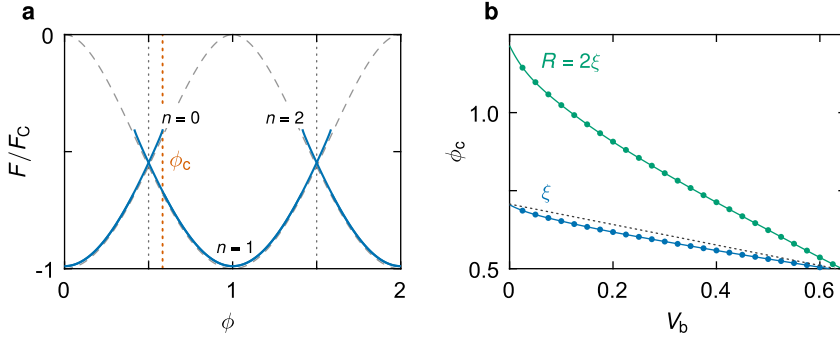


Figure 4.4 | Reduction of critical flux as a function of bias voltage. **a** | Free energy, normalized by the condensation energy F_C , for a voltage-biased superconducting ring of radius $R = \xi$. The bias voltage $V_b = 3/10$. **b** | The critical flux ϕ_c for a deterministic transition from the flux state $n = 0$ to $n = 1$ as a function of V_b for various radii R of the ring. The dashed grey line corresponds to the critical flux (4.15).

where v_s^b corresponds to the current driven by the bias voltage, and v_s^ϕ to the persistent current driven by the flux bias. The latter takes the form

$$v_s^\phi = \frac{1}{\kappa R}(n - \phi). \quad (4.14)$$

Variations of the magnitude of the order parameter—owing to the bias voltage—are treated as fluctuations in the instability analysis. For a small bias voltage, these variations are indeed minimal and fit within the weak-fluctuation limit; hence, the linearization of the TDGL around a metastable flux state is valid. Accordingly, the overall superfluid velocity obeys the instability criterion (4.12). Substituting with the analytical expression (3.22) of the maximum superfluid velocity yields the critical flux

$$\phi_c = \frac{\kappa R}{\sqrt{3}} \sqrt{1 + \frac{\xi^2}{2R^2}} - \frac{\kappa R}{\xi} \frac{V_b}{2} \tanh\left(\frac{\pi R}{4\xi}\right), \quad (4.15)$$

which depends on the value of the voltage V_b specified by the bias electrodes.

The critical flux (4.15) is in sound agreement with the numerical solution of the TDGL equations for a ring of radius $R = 1$ (Figure 4.4b). But the larger the radius, the larger the variations of the order parameter along the ring, which renders the analytical expression (3.22) of the maximum superfluid velocity

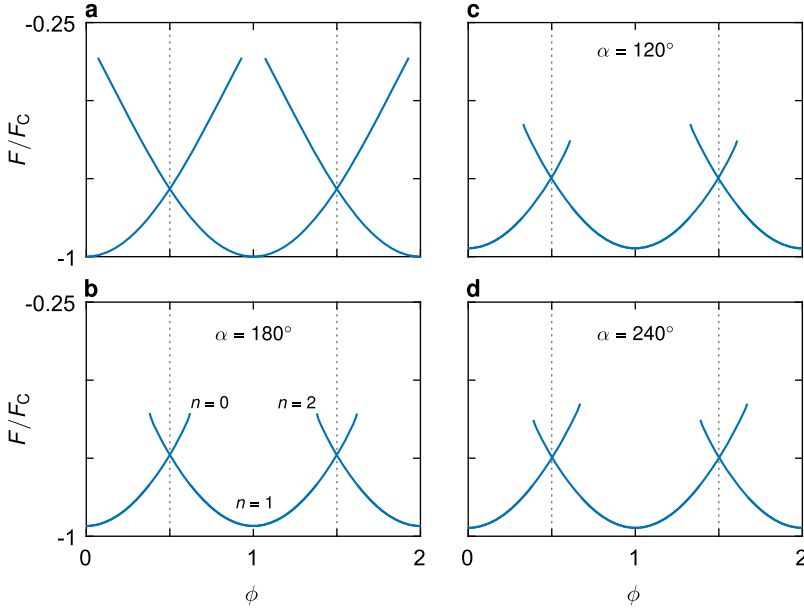


Figure 4.5 | Voltage-biased superconducting rings threaded by a solenoid field. The free energy F , normalized by the condensation energy F_C , as a function of the flux ϕ enclosed by the ring. The unbiased case is depicted in (a), whereas a bias voltage $V_b = 4/5$ is used for (b-d). The angle α between the bias electrodes is varied (see the model in Figure 3.4). Parameters used: $R = w = \xi$, $\kappa = 1$, $\gamma = 7^\circ$, and $\sigma = 1$.

imprecise. Moreover, because the stability analysis hinges on the linearization of the TDGL equation in the limit of weak fluctuations, the instability criterion is less accurate for larger variations in the order parameter. That is to say, treating a small bias voltage as a fluctuation becomes less accurate as the radius increases compared to the coherence length. Consequently, the criterion (4.15) is only valid in the limit $R \sim \xi$. In general, I evaluate the critical flux using the numerical solution of the TDGL equations. As a function of the bias voltage, the critical flux for a transition between two flux states n and $n + 1$ tends to the degeneracy point $\phi = n + 1/2$ (Figure 4.4b). Equivalently, as detailed in Chapter 5, the free-energy barrier separating these two states tends to zero.

To further examine the relation between the bias voltage and the critical flux, I expand the discussion to rings of finite widths, for which the magnetic field

4. Deterministic Transitions between Flux States

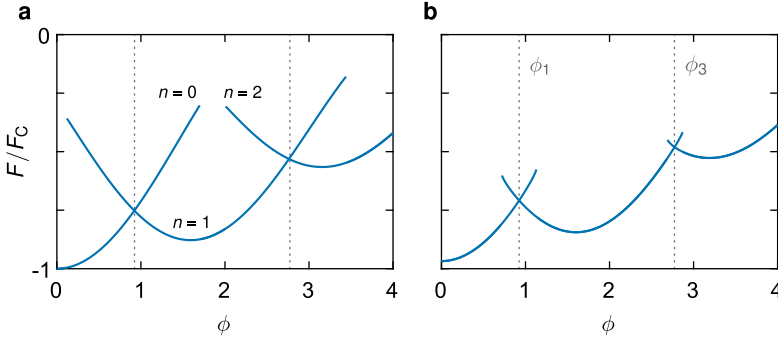


Figure 4.6 | Voltage-biased superconducting rings in a uniform magnetic field. The free energy F , normalized by the condensation energy F_C , is given as a function of the flux ϕ enclosed by the outer rims of both unbiased (a) and biased (b) rings. The dotted lines represent the degeneracy points given in Equation (4.16). Parameters used: $R = w = \xi$, $\kappa = 1$, $\alpha = 180^\circ$, $\gamma = 7^\circ$, $V_b = 4/5$, and $\sigma = 1$.

can be either localized within the ring or uniform throughout the space. First, for the localized configuration, the magnetic field is only nonzero within the ring, which can be achieved using a solenoid core that pierces the ring (see Figure B.1 in Appendix B). Because the bulk of the ring is not exposed to any external magnetic field, all the minima of the free energy are degenerate and occur at integer multiples of the flux quantum (Figure 4.5a). The degeneracy point between two states n and $n + 1$ is exactly at $\phi = n + 1/2$, where ϕ is the normalized flux enclosed by the inner boundary of the ring.

In agreement with Figure 4.4, upon biasing the ring, the critical flux for a deterministic phase slip tends to the degeneracy point at half-integer flux quanta. The choice of the angle α between the bias electrodes selectively favors transitions that increment or decrement the phase winding number of the ring. For example, if the angle $\alpha = 180^\circ$, then the bias voltage divides the ring into two symmetric arms. Consequently, the sum of the current induced by bias voltage and the circulating current induced by the enclosed magnetic flux is identical for the states n and $n + 1$, and the symmetry of the free-energy spectrum is preserved (Figure 4.5b). In contrast, for $\alpha = 120^\circ$, the clockwise current induced by the bias voltage in the upper shorter arm of the ring is higher than the counterclockwise current in the longer arm. As a consequence,

a lower magnetic flux is required for phase slips in the upper arm; hence, this geometry favors transitions that increment the phase winding number (Figure 4.5c). A mirror reflection of this energy spectrum is obtained for the complementary angle $\alpha = 360 - 120 = 240^\circ$, for which transitions that decrement the phase winding number are favored.

Second, for the uniform configuration, the magnetic field directly impinges on the ring and must be screened. Therefore, transitions between the flux states are not governed only by the quantization of magnetic flux but also by the Meissner effect. The minima of the free energy deviate from the integer flux quanta (Figure 4.6a). In terms of the flux ϕ enclosed by the outer boundary of the ring, the degeneracy points between flux states are given by [135]

$$\phi_m = m \frac{\ln \varepsilon}{\varepsilon^2 - 1}, \quad (4.16)$$

where m is an integer, and the ratio ε is defined as $\varepsilon \equiv R/(R + w)$. Analogous to the solenoid configuration, the bias voltage reduces the critical flux for a deterministic transition to the subsequent flux state. Incidentally, the uniform configuration tends to the solenoid one as the width of the ring decreases in comparison to the coherence length. The magnetic field profiles in the uniform and the localized configurations are discussed in Appendix B.

To sum up, the bias voltage controls the dynamics of deterministic phase slips in superconducting rings. Specifically, it reduces the critical flux ϕ_c to the degeneracy points between the discrete flux states of the ring, or equivalently it reduces the free-energy barrier to zero. To symmetrically reduce the barrier between two states n and $n+1$, the ring must be *locally* flux biased by $\phi = n+1/2$ and the angle between the bias electrodes must be equal to π . The next section analyzes the regime of a vanishing free-energy barrier, while Chapter 5 explores stochastic transitions between flux states for a very small but nonzero barrier.

4.2.2 Voltage-controlled coupling of flux states

This section inspects the regime where the critical flux for a deterministic phase slip decreases to the degeneracy point between two subsequent flux states. In that limit, the energy barrier separating these two states vanishes,

4. Deterministic Transitions between Flux States

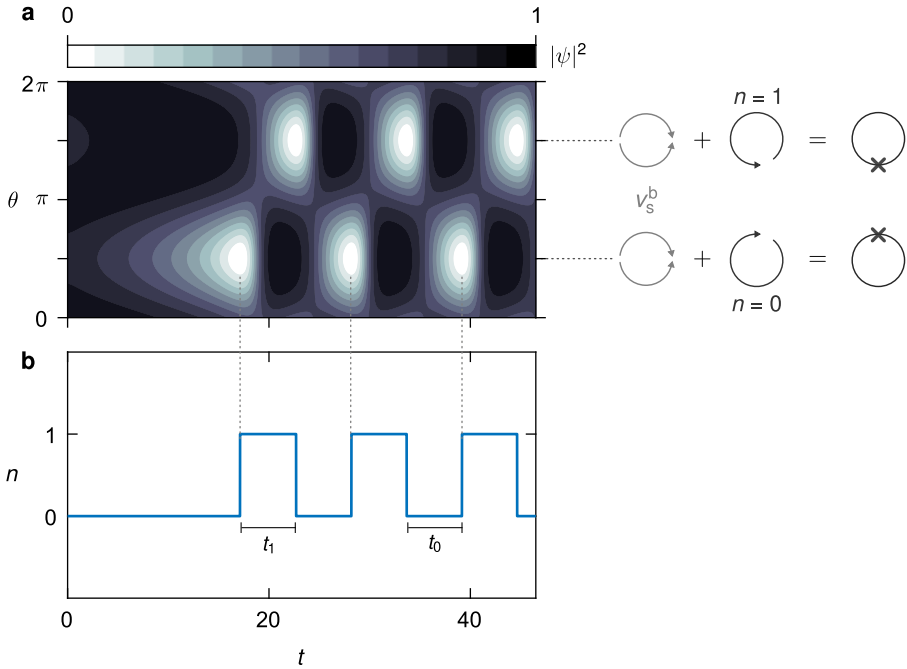


Figure 4.7 | Coupling of flux states n in a voltage-biased superconducting ring. **a** | Time evolution of the density of Cooper pairs $|\psi|^2$ along the azimuthal angle θ . The location of phase slips depends on the phase winding number n (see the schematic on the right where the cross denotes the phase-slip location). **b** | Time evolution of the flux state n . Parameters used: $R = \xi$, $\kappa = 1$, $\sigma = 1$, and $V_b = 3/2$. At $t = 0$, the ring is voltage biased, and the flux bias is ramped up to $\phi = 1/2$ with a rise time $t_\phi = 20$.

and the free-energy spectrum is no longer hysteric. Consequently, for a flux bias $\phi = n + 1/2$, the ring oscillates between the two adjacent states n and $n + 1$.

To capture this behavior, I consider a ring enclosing half a flux quantum. Subject to a bias voltage that reduces the critical flux below $\phi = 1/2$, the phase winding number n oscillates between $n = 0$ and $n = 1$ (Figure 4.7b). In contrast to the zero-magnetic-field example in Figure 3.7a, only a single phase slip occurs at any given moment (Figure 4.7a), and phase slips alternate between the two arms of the ring depending on the flux state n . The breaking of the reflection symmetry of the Cooper-pair density along the x axis is caused by the interference of the current driven by the bias voltage and the persistent current

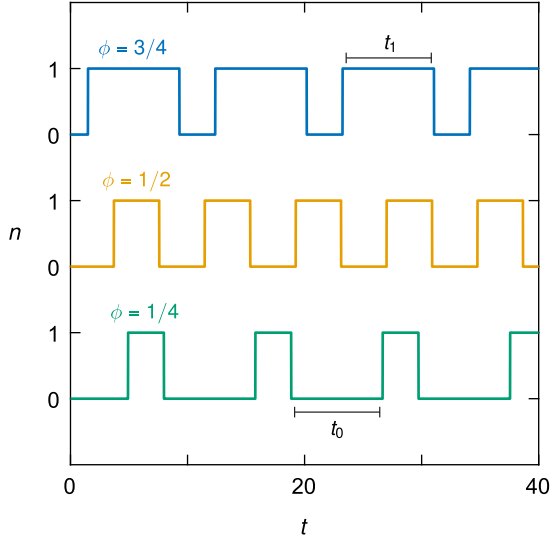


Figure 4.8 | Asymmetric coupling of the flux states of a superconducting ring. The phase winding number n is plotted as a function of time. The applied flux ϕ is varied from a quarter to three quarters of the flux quantum, altering the time spent in each flux state n . Parameters used: $R = \xi$, $\kappa = 1$, $\sigma = 1$, and the bias voltage $V_b = 3/2$.

driven by the enclosed flux. In the flux state $n = 0$, a clockwise current circulates to screen the applied flux. In the upper arm of the ring, this screening current adds to the current driven by the bias voltage. Thus, the critical superfluid velocity required for a phase slip is attained at $\theta = \pi/2$. Conversely, in the flux state $n = 1$, instead of a screening current, a counterclockwise current circulates to complement the applied flux. Thus, the phase slip occurs at $\theta = 3\pi/2$, and the ring transitions to the state $n = 0$.

Because the applied flux is precisely halfway between zero and one flux quantum, the two flux states are symmetrically coupled (i.e., the ring spends equal durations in $n = 0$ and $n = 1$). Modifying the applied flux skews the coupling towards either state (Figure 4.8). For instance, at a quarter of the flux quantum, the ring stays a longer time in $n = 0$ and a shorter time in $n = 1$. The complementary coupling is attained for $\phi = 3/4$. Although this discussion focuses on the coupling between the two states $n = 0$ and $n = 1$, the analysis applies to higher flux states provided that the flux bias is increased.

4. Deterministic Transitions between Flux States

So far, I have examined the behavior of a voltage-biased superconducting ring. I have demonstrated that the bias voltage can tune the free-energy barrier to zero, resulting in coupling of adjacent flux states. In the next section, I explore how this coupling can be utilized to build a superconducting memory whose state is written via deterministic phase slips, triggered by a voltage-induced reduction of the energy barrier. Specifically, a bias-voltage pulse temporarily lowers the barrier to permit a single transition from a flux state n to $n + 1$, denoting logic '0' and '1', respectively. The duration and amplitude of the pulse must be controlled so that the free-energy barrier is restored before the ring flips back to its initial state n .

4.3 Proposal for a superconducting memory

Since the discovery of superconductivity, numerous superconducting devices have emerged such as qubits [18, 19, 21–24], SQUIDs [10], and parametric amplifiers [25, 26]. One domain, however, where superconductivity falls short is information storage. Scalable superconducting memories have long been sought to complement the single-flux-quantum (SFQ) superconducting logic. Moreover, motivated by the race towards building scalable quantum computers, superconducting memories are crucial owing to their compatibility with the cryogenic working temperatures of quantum computers.

The simplest form of a superconducting memory is an isolated superconducting loop (e.g., a ring). The state of the memory is stored in the absence or presence of a single flux quantum within the loop, denoting logic ‘0’ and ‘1’, respectively. This state is manipulated inductively by varying the magnetic flux threading the loop using an external current loop. For instance, to write ‘1’ starting from an initial state of zero flux quanta, the flux is increased to trigger a transition to the subsequent flux state (Figure 4.3). Likewise, to write ‘0’, the flux is decreased to trigger the reverse transition. The memory state is read by sensing the overall flux enclosed within the loop. One possibility is to measure the current induced in a nearby readout loop (Figure 4.9). To minimize crosstalk between the write and readout loops, the three loops can be interconnected via ferromagnetic cores with high magnetic permeability in a transformer-like arrangement [136]. Because of the inductive read and write operations, this implementation is limited in both scalability and performance. Additionally, even in the presence of the ferromagnetic cores, crosstalk between the write and readout loops is inevitable.

In this section, I present a novel superconducting memory whose state is read and written electrically. This memory harnesses the magnetic bistability of a voltage-biased ring, as depicted by the oscillating winding number n in Figure 4.7. Instead of a constant bias, however, a time-dependent bias voltage temporarily lowers the free-energy barrier to trigger a single phase slip, constituting a write operation. The state is read nondestructively by measuring the voltage drop across the ring in response to a shorter voltage pulse.

4. Deterministic Transitions between Flux States

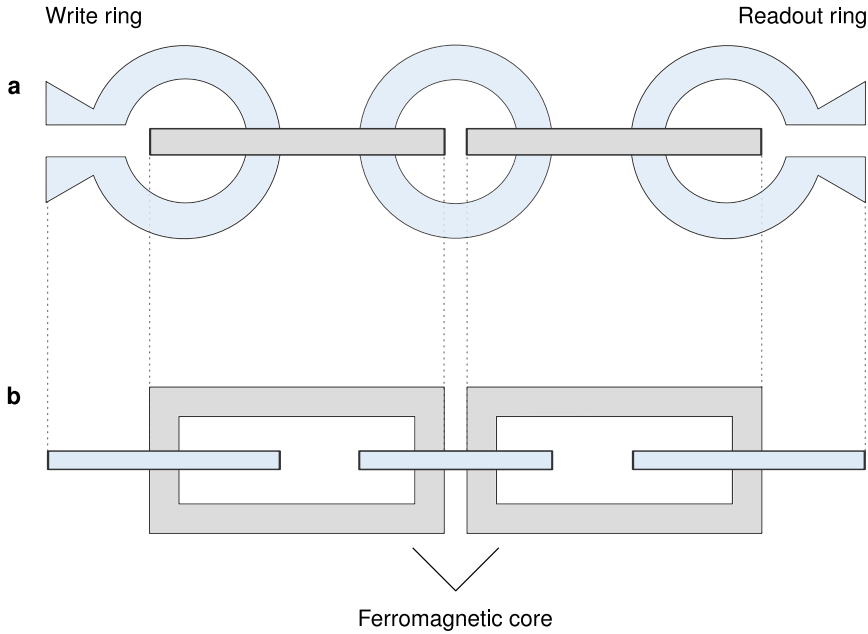


Figure 4.9 | Superconducting memory. Top (a) and side (b) views of a memory element consisting of three superconducting rings interconnected via ferromagnetic cores in a transformer-like arrangement. The two cores pierce the central bit ring, coupling it to a write (*left*) ring and a readout (*right*) ring.

Analogous to SQUID-based memories [11, 137–140], the proposed memory element is nonvolatile, and its state is preserved as long as the ring is in the superconducting state. Regarding the speed of the read and write operations, this memory compares to standard Rapid Single-Flux-Quantum (RSFQ) memories [11, 137–140]. Its main advantage is the scalability and ease of fabrication of an uninterrupted superconducting ring. In fact, one of the bottlenecks impeding the scalability of RSFQ memories is the Josephson junction, which cannot be aggressively scaled without causing variability and degrading the performance of the memory [141]. Moreover, to create a bistable system, the inductance of the superconducting loop must be comparable to that of the Josephson junction, which precludes reducing the footprint of RSFQ memories [142]. In contrast, the proposed memory allows for electronic read and write operations without the junction, which enables a high-density superconducting memory. Its main drawback, however, is the difficulty to

fabricate nanorings with minimal defects and to produce the required half-flux-quantum bias within a nanosized ring. This drawback can be overcome by calibrating each bit separately to accommodate the presence of defects and deviations from the desired flux bias.

The rest of this section examines the working principle of the proposed memory, focusing on the required pulse width for the read and write operations. The performance of the memory is analyzed in terms of its insensitivity to thermal fluctuations, sample defects, and variations in the control parameters. Finally, a practical example using aluminum nanorings is discussed.

4.3.1 Working principle

The memory element comprises a voltage-biased superconducting ring, in addition to two readout electrodes to measure the voltage drop across the ring (Figure 4.10). The ring is also flux biased by a time-invariant magnetic field, generated either by using an external current loop or by placing a permanent magnet within the ring (e.g., a multilayer stack of cobalt–platinum [143]).

Subject to a time-independent bias voltage that suppresses the free-energy barrier, the flux state of the ring oscillates between n and $n + 1$, provided a flux bias $\phi = n + 1/2$. To selectively control the state, the bias voltage is pulsed to permit one phase slip at a time. The pulse width must be longer than the time required to enforce a phase slip in one arm of the ring, but shorter than the time required to enforce a second phase slip in the other arm. To determine the proper pulse width, the memory must be calibrated for a specified amplitude of the bias voltage (Figure 4.10). Starting with a flux-biased ring in the state $n = 0$, the bias voltage is ramped up to a predetermined amplitude that is large enough to tune the free-energy barrier to zero, or equivalently the critical flux to the half-flux-quantum degeneracy point. A viable pulse width must be longer than the time required for the first phase slip and shorter than that required for the second phase slip. In practice, the pulse width (PW) can be chosen as the time difference between the moment the bias voltage is switched on and the first peak in the voltage difference V_{12} (see the inset of Figure 4.10).

4. Deterministic Transitions between Flux States

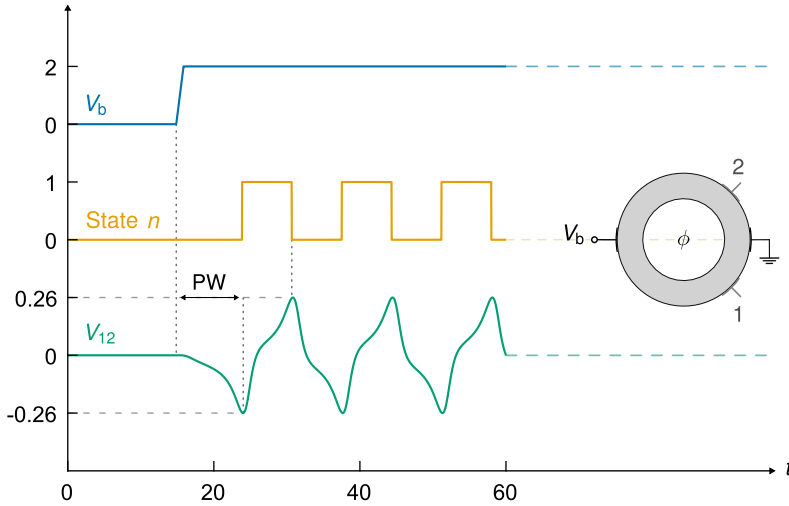


Figure 4.10 | Pulse width for the write operation. The bias voltage V_b and the phase winding number n are plotted as a function of time. The ring is flux biased by $\phi = 1/2$. The voltage V_{12} oscillates as vortices alternate between the two arms of the ring (see the *inset* for electrodes 1 and 2). The calibrated pulse width is denoted by PW . Parameters used are in line with Figure 3.10. All quantities are normalized as in Appendix A.

The pulse width for the write operation depends on the choice of the superconductor, seeing that the time t is normalized by the ratio of the coherence length to the diffusion coefficient. In addition, as demonstrated by Figure 3.11, the size of the ring relative to the coherence length governs the time needed to nucleate a phase slip. Specifically, altering the distance a vortex travels to escape from the ring—that is, the width w —modifies the pulse width required for triggering a single phase slip. The pulse width can also be controlled in situ by varying the amplitude of the bias voltage or the operating temperature, which modifies the effective dimensions of the ring since the coherence length is a function of temperature.

Using the calibrated pulse width, the write operation proceeds as follows. First, the ring starts in an initial flux state $n = 0$, in which a clockwise supercurrent opposes the external flux (i.e., the memory state is ‘0’). To write ‘1’, a bias-voltage pulse is applied to enforce a single phase slip, and the phase winding number n is incremented by one (Figure 4.11). This transition corresponds to

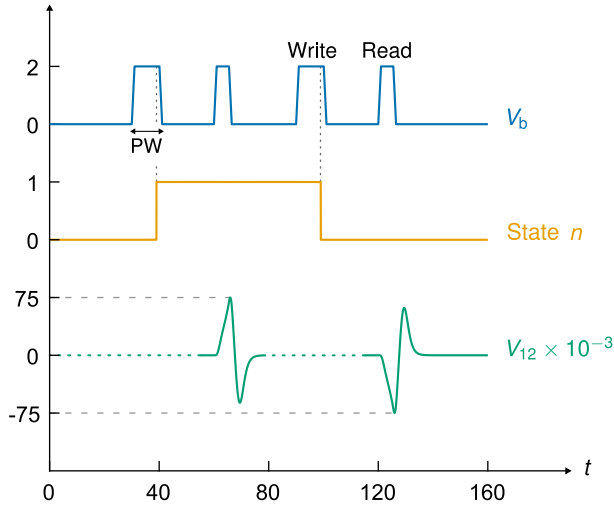


Figure 4.11 | Working principle of a voltage-controlled superconducting memory. The write and nondestructive read operations are executed using bias-voltage pulses of widths PW and $PW/2$, respectively. The vortex motion during the write operation is captured in Figure 4.12. The phase winding number n encodes the memory state. The horizontal dotted line implies that the voltage V_{12} is not recorded until the readout pulse is applied. Parameters used are in line with the calibration in Figure 4.10.

an antivortex departing the ring (Figure 4.12a). Because the ring is flux biased midway between the two relevant flux states, the coupling is symmetric. As a consequence, repeating the same pulse triggers the reverse transition to the state $n = 0$, corresponding to a vortex departing the ring (Figure 4.12b).

Because the location of the nucleated vortex depends on the winding number n , the memory state can be retrieved by applying a pulse and measuring the voltage drop across the ring. The sign of the voltage difference between the two electrodes 1 and 2 determines the state n , as depicted in Figure 4.10. If the voltage difference $V_2 - V_1$ is negative, then the phase slip occurs at the upper arm of the ring, implying that the ring was in the state $n = 0$. If the voltage difference is positive, then the ring was in the state $n = 1$. Accordingly, the state of the memory is read destructively by applying the same voltage pulse. If the controlling circuitry permit a pulse width shorter than that of the write pulse, then a nondestructive readout is also feasible. Similar

4. Deterministic Transitions between Flux States

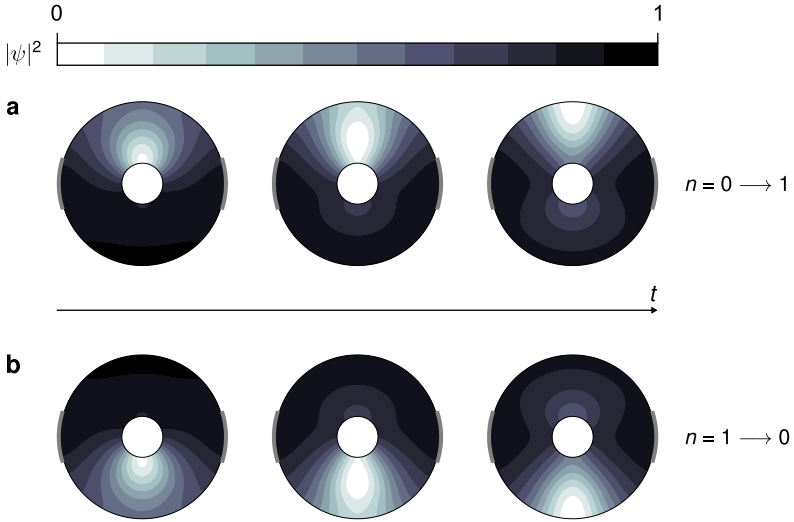


Figure 4.12 | Phase slips during the write operation. The normalized Cooper-pair density $|\psi|^2$ during the write ‘1’ (a) and ‘0’ (b) operations in Figure 4.11.

to the destructive readout, the sign of the voltage difference V_{12} reflects the memory state (Figure 4.11). The profile of the voltage drop resembles a full cycle of a sinusoidal function owing to the relation between the supercurrent density and the superfluid velocity (i.e., $J_s \propto v_s - v_s^3$). Once the bias voltage is switched on, the superfluid velocity increases in one arm of the ring up to its critical depairing value, beyond which the supercurrent density decreases as the cubic term of v_s dominates. Due to the incompressibility of the total current density ($\nabla \cdot \mathbf{J} = 0$), the normal-current density increases in the same arm, and the voltage difference between the two arms peaks. Once the bias voltage is switched off, the superfluid velocity decreases. But, as depicted in Figure 4.2, the supercurrent density must first increase before decreasing to its equilibrium value—that is, the value corresponding to a flux bias $\phi = 1/2$. Therefore, the relation of the supercurrent density and the superfluid velocity results in the sinusoidal signature of the voltage difference V_{12} (Figure 4.11).

Evidently, writing and reading the memory state demand precise control of the flux bias and the duration of the voltage pulses. The next section analyzes the fidelity of the memory under asymmetric flux bias and a varying pulse width.

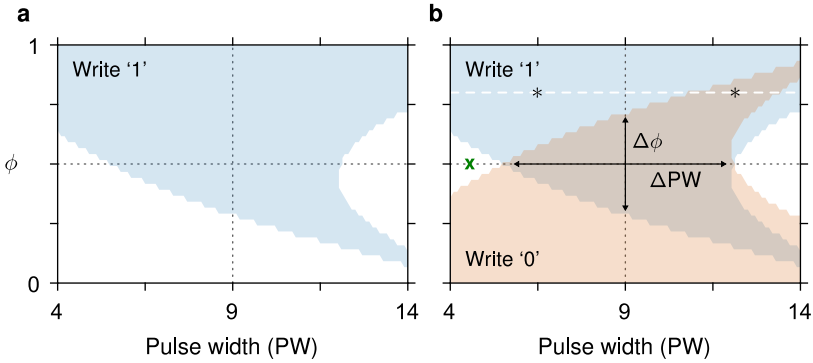


Figure 4.13 | Fidelity of the write operation in response to variations in the control parameters. **a** | Successful write ‘1’ operation as a function of the normalized flux ϕ and the voltage pulse width, varied by 50% of a calibrated value of 9. **b** | Overlaid write ‘1’ (blue) and ‘0’ (red) operations. The green cross indicates the pulse width for the nondestructive readout in Figure 4.11. The asterisks denote the pulse width for the asymmetric bias $\phi = 4/5$ in Figure 4.14. Other parameters are identical to Figure 4.11.

4.3.2 Tolerance to noise and device variability

This section assesses the functionality of the proposed memory in response to variations in the control parameters, namely the flux bias and the pulse width of the bias voltage. In addition, the functionality is evaluated in the presence of random noise, which models defects and thermal fluctuations. The figure of merit is the fidelity of the write operation.

a) Tolerance to variations in the control parameters

The write operation entails permitting a single phase slip at a time, which demands precise control over the pulse width of the bias voltage. The same pulse is used to write both ‘0’ and ‘1’ by ensuring that the flux bias is precisely halfway between the two relevant flux states (i.e., $\phi = 1/2$). But, in practice, the pulse width can deviate from its calibrated value due to variations in the controlling circuitry. Likewise, the presence of magnetic impurities can shift the desired half flux quantum towards either zero or one flux quantum. To assess the tolerance of the memory to these variations, I calculate the fidelity of the write operation while varying both the pulse width and the flux bias.

4. Deterministic Transitions between Flux States

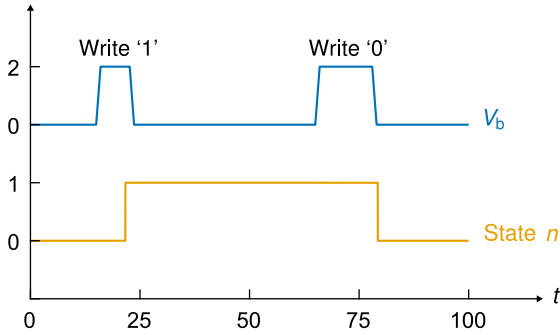


Figure 4.14 | Write operation under asymmetric flux bias. The bias voltage V_b and the memory state n are plotted as a function of time. Unlike the symmetric operation in Figure 4.11, the memory is flux biased by $\phi = 4/5$. The chosen pulse widths are marked by asterisks in Figure 4.13. All other parameters are consistent with Figure 4.11.

The write '1' operation in Figure 4.11 is repeated while varying the flux bias from zero to one flux quantum and the pulse width by 50% of its calibrated value. For a fixed flux bias $\phi = 1/2$, the pulse width can safely fluctuate around its calibrated value between two limits (Figure 4.13a). If the pulse width is too short, the ring does not transition to the other flux state (i.e., the write operation fails). Conversely, if the width is too long, two transitions occur. Thus, the memory state is overwritten, and the ring reverts to its initial state $n = 0$.

As for variations in the magnetic flux bias, the closer it is to an integer multiple of the flux quantum, the shorter the pulse width needed to write the corresponding state. For example, if the flux ϕ is smaller than half a flux quantum, then a duration longer than the calibrated value is required to write '1', and the tolerance of the write operation to variations in the pulse width decreases (Figure 4.13a). In contrast, if the flux is larger than half a flux quantum, the tolerance increases. Unfortunately, this gain is accompanied by a reduced window of viable pulse widths for a nondestructive readout. In that limit, the read operation must be executed destructively.

The fidelity of the write '0' operation is the mirror reflection of the write '1' operation along the half-flux-quantum line (Figure 4.13a). Its tolerance to variations in the pulse width changes as the flux bias deviates from $\phi = 1/2$. If

the flux shifts closer to zero flux quanta, more variability is tolerated in writing ‘0’. More important, to guarantee that both write operations can function simultaneously, the parameters PW and ϕ must fall within the overlap of the two write operations. If the flux bias is intentionally selected outside this range, each write operation must be calibrated separately. For example, assuming a flux bias $\phi = 4/5$, a shorter duration can be employed for writing ‘1’, whereas a longer duration is required for writing ‘0’ (Figure 4.14). These two pulse widths are denoted by asterisks in Figure 4.13b.

b) Tolerance to defects and thermal fluctuations

This section focuses on the fidelity of the write operation in the presence of random noise, representing defects and thermal fluctuations. The noise can be modeled by a Langevin-type dynamics using a variant of the time-dependent GL equation that incorporates an additive noise term in the form

$$\left(\frac{\partial}{\partial t} + i\kappa V\right)\psi = -\left(\frac{i}{\kappa}\nabla + \mathbf{A}\right)^2\psi + (1 - |\psi|^2)\psi + \eta, \quad (4.17)$$

where η is a random, complex-valued field in space and time. Following the discretization scheme of Appendix C, the noise at each grid point in space and time is sampled from a normal distribution with zero mean.

The noise term η depends on the size of the defects in the ring. If defects occur on a scale much smaller than the coherence length, then η can be assumed independent in space. Conversely, if they occur on the scale of the coherence length, then η must have a commensurate length scale. For thermal fluctuations, η is not restricted to a specific spatial distribution. Its variance, however, depends on temperature and is proportional to $p(T/T_c)(1 - T/T_c)$, where p is approximately 1/80 [144, 145]. At the critical temperature, the variance diverges to infinity, implying substantial thermal fluctuations close to the superconducting phase transition.

I consider two types of noise: correlated and uncorrelated. The latter represents thermal fluctuations and defects occurring on a scale much smaller than the coherence length ξ . In contrast, the former represents defects occurring on

4. Deterministic Transitions between Flux States

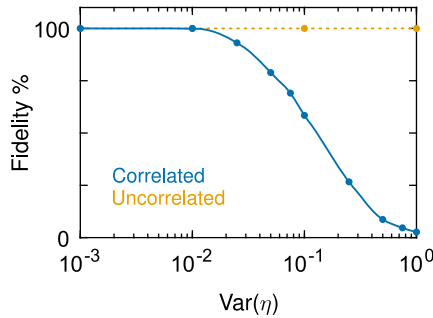


Figure 4.15 | The fidelity of the write operation in the presence of random noise. The fidelity is estimated by repeating the write operation in Figure 4.11 500 times in the presence of additive noise η , sampled from a Gaussian distribution with zero mean and variance ranging from 10^{-3} to 10^0 . The uncorrelated noise models thermal fluctuations and is sampled on the same finite-difference grid for the TDGL equations. The correlated noise is sampled on a coarser grid that is commensurate with the coherence length ξ . Thus, it represents defects occurring on the scale of ξ .

the scale of the length ξ . For the uncorrelated noise, η is sampled on the same spatial and temporal grid of the superconductor. At each node, it is evaluated as an independent random variable with a Gaussian distribution with zero mean. The variance is varied from 10^{-3} to 10^0 to cover the range of thermal fluctuations. To estimate the fidelity, the write ‘1’ operation in Figure 4.11 is repeated 500 times for each value of the variance. A successful write operation dictates that the memory state changes only once to the final state. If the state changes an odd number of times ending up in the desired state, the write operation is considered faulty. Predictably, because the functionality of the memory depends on macroscopic parameters—notably, the coherence length ξ —it is immune to defects that are much smaller than ξ (Figure 4.15).

For the correlated noise, the term η is assumed time independent—as sample defects would be—and spatially correlated on the scale of the coherence length. Numerically, the noise is sampled on a coarse grid commensurate with the coherence length, then interpolated to the fine grid over which the finite-difference derivatives of the time-dependent GL equations are computed. At each node of the coarse grid, the noise is sampled from a Gaussian distribution with zero mean and variance ranging from 10^{-3} to 10^0 .

The fidelity of the write operation deteriorates in the presence of defects that are comparable in size to the coherence length and drops to almost zero when the variance of η is equal to one (Figure 4.15). In general, defects drastically alter the phase-slip dynamics in the ring, thereby impairing the write operation. On the one hand, defects can aid the bias voltage in suppressing the Cooper-pair density in the ring and, hence, expedite the nucleation of phase slips. Therefore, a shorter pulse width is needed to ensure that only one phase slip occurs. On the other hand, if defects are strong enough to locally destroy superconductivity in the ring, they can cause vortex pinning. Consequently, a higher bias voltage is needed to eject a vortex during the write operation, so that the ring can transition to the subsequent flux state.

Nevertheless, the fidelity can be recovered by calibrating the pulse width in the presence of defects. For instance, if defects break the cylindrical symmetry of the ring, the energies required for a vortex to escape through the upper and lower arms are not equal. Consequently, two distinct pulses must be chosen for writing '0' and '1'. In other words, the memory must be calibrated twice to determine the pulse width required to overcome any inadvertent behavior caused by defects. As an alternative, one can keep the pulse width unchanged and, instead, tune the amplitude of the bias voltage.

c) Effect of Joule heating

The electronic control of the memory hinges on ejecting one vortex at a time to flip the flux state of the ring. Due to the normal electrons in the core of a vortex, its motion is accompanied by Joule heating. Additionally, for a voltage-biased superconducting ring, heating occurs close to the bias electrodes owing to the injection of normal electrons, indicated by the penetration of the electric field inside the superconductor (Figure 3.1c). This section qualitatively discusses the effect of Joule heating in superconductors and highlights several practical considerations for the proposed memory.

In general, heating can cause diverse effects in superconductors. On the one hand, it can drastically change the dynamics of phase slips and be used to manipulate vortices down to the level of a single vortex [146–151]. On the other

hand, it can raise a superconductor's temperature above the critical one and destroy superconductivity altogether [152]. This behavior is the basis of single-photon detectors, in which an incident photon creates a hotspot that diffuses and results in a measurable resistance across the superconductor [153–155].

The proposed memory can tolerate heat-induced variations of vortex velocities, as corroborated by Figure 4.13 where the write operation succeeds even when the pulse width deviates by 50% from its calibrated value. Nonetheless, a detailed analysis of the effect of Joule heating during a complete write and readout cycle is still necessary, seeing that it may impose an upper limit on the operation frequency and on the amplitude of the bias voltage. While this analysis is beyond the scope of this thesis, I discuss the theoretical framework typically employed to study heat diffusion in superconductors with the purpose of underlining the factors governing the thermal behavior of a superconducting film. The time-dependent Ginzburg-Landau equations are solved self-consistently with the heat diffusion equation [156–158]

$$C \frac{\partial T}{\partial t} = k \nabla^2 T - \frac{h}{d} (T - T_0) + \frac{1}{\sigma_n} J_n^2, \quad (4.18)$$

where C is the heat capacity, k is the heat conductivity, h is the heat transfer coefficient, and d is the thickness of the superconductor. The heat equation describes the temporal and spatial evolution of a local temperature $T(\mathbf{r}, t)$ for a superconducting film kept at a bath temperature T_0 . The heat is redistributed by thermal conduction within the superconductor and by heat transfer to the substrate [152]. The last term accounts for Joule heating and connects the heat equation to the time-dependent GL equations. Specifically, it couples to the continuity equation (3.2) via the normal-current density J_n . For a voltage-biased ring, the gradient of the scalar potential and, in turn, the normal-current density are nonzero only near the bias electrodes and upon the nucleation of vortices in the write and readout operations of the proposed memory.

The thermal behavior of a superconducting device depends on the operating temperature and on the material choice of the superconductor, as captured by the parameters C and k in the heat equation (4.18). What's more, because the substrate is the primary heat sink, it determines the overall rate of heat removal from the superconductor [159]. For example, the choice of the substrate is

crucial in superconducting single-photon detectors because the count rate of photons depends on how fast a hotspot relaxes [155]. To maximize the count rate, the hotspot relaxation time should be minimized by increasing the rate of heat transfer to the substrate (e.g., the lowest hotspot relaxation time for NbN detectors is obtained using MgO substrates [155]). Similarly, for the proposed memory, heat must be removed sufficiently fast from the superconducting ring to avoid unintended transitions to neighboring flux states.

Importantly, two characteristic scales govern the thermal behavior of the proposed memory. First, the thermal healing length $\Lambda_T = \sqrt{\kappa d / \hbar}$ describes the distance over which temperature varies in the ring—that is, the spatial extent of the heat generated by a passing vortex. The ratio of the healing length to the size of the ring is therefore essential for the success of the write operation because it determines whether the heat generated by a passing vortex along one arm of the ring spreads to the phase-slip center in other arm. The spread heat and the associated depletion of the order parameter may trigger the nucleation of an additional vortex (i.e., the write operation fails). Second, the time scale Cd/\hbar describes how fast temperature changes inside the superconducting ring. The rate of change of the local temperature determines whether the heat generated by a crossing vortex along one arm of the ring affects the subsequent vortex along the same arm. It accordingly establishes the minimum allowed time between consecutive write operations such that the heat-induced depletion of the order parameter produced by a vortex does not alter the dynamics of the next. Evidently, both characteristic scales can be minimized by maximizing heat transfer to the substrate. In sum, solving the heat diffusion equation with the time-dependent Ginzburg Landau equations would yield several practical insights regarding the proper choice of the superconductor and the substrate. In addition, this analysis would set an upper limit on the frequency of the write operation of the proposed memory.

4.3.3 Memory example using aluminum nanorings

This section presents an example of the proposed memory using aluminum rings. Contrary to previous discussions, all physical quantities are represented in SI units to demonstrate the order of magnitude of the pulse width and the

4. Deterministic Transitions between Flux States

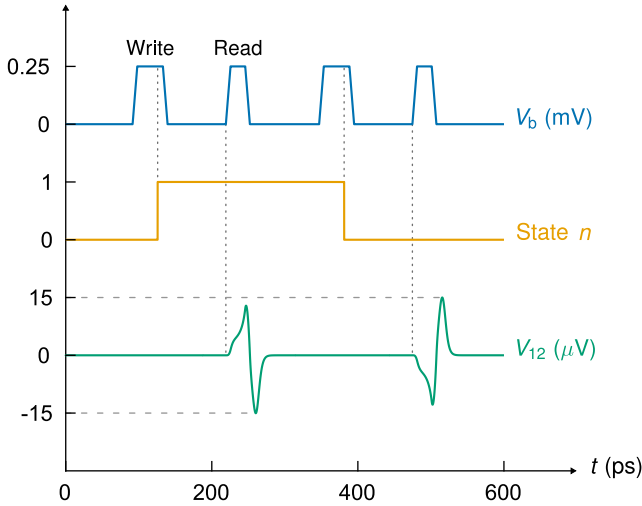


Figure 4.16 | Working principle of a voltage-controlled superconducting memory. The read and write operations are executed by pulsing the bias voltage V_b . The state of the memory n is read via the voltage difference V_{12} (see the inset of Figure 4.10). The aluminum ring is of radius $R = 200$ nm and width $w = 200$ nm. Parameters used: $T = 1$ K, $T_c = 1.32$ K, $\gamma = 18^\circ$, and the mean free path $\ell = 6$ nm.

amplitude of the bias voltage. The superconducting parameters of aluminum thin films are extracted from [80]. The critical temperature equals 1.32 K. The mean free path $\ell = 6$ nm, and the normal-state resistivity ρ is obtained from the relation $\rho\ell = 4 \times 10^{-6} \mu\Omega \cdot \text{cm}^2$ for aluminum films [160]. The coherence length and the penetration depth are calculated at an operating temperature $T = 1$ K using the empirical relations (2.28) and (2.29).

The read and write operations are executed electronically via a bias voltage in the order of hundreds of microvolts. For instance, at a bias voltage of 0.25 mV, the pulse width is about 35 picoseconds (Figure 4.16). A picosecond pulse duration might require specialized circuitry to generate (e.g., RSFQ logic [161]). To use a longer pulse width, the amplitude of the bias voltage must be lowered, as illustrated by the oscillation period in Figure 4.17. Additionally, as discussed in Section 4.3.1, the pulse width for the write and read operations can be modified by varying the operating temperature, which changes the coherence length of the superconductor, and the dimensions of the ring.

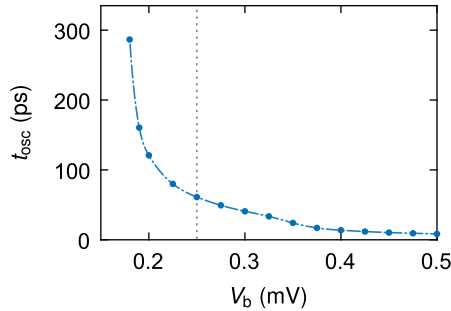


Figure 4.17 | Oscillation period of phase slips as a function of the bias voltage. The period t_{osc} is plotted as a function of the bias voltage V_b for a ring of $R = w = 200$ nm. The dotted line corresponds to the voltage used in Figure 4.16.

To sum up, the bias voltage locally suppresses the density of Cooper pairs, forming two weak links that serve as preferential locations to nucleate phase slips in a superconducting ring. This suppression causes a reduction of the critical flux that triggers deterministic transitions between the discrete flux states of the ring. The electronic control of the critical flux implies that the bias voltage modulates the free-energy barrier separating the flux states. For a vanishing barrier, the ring reaches a dynamic equilibrium, oscillating between two subsequent flux states. The practicality of the electronic control of the barrier is exemplified by a superconducting memory whose state is encoded by the absence or presence of a single flux quantum within the ring. The state of the memory is read and written via picosecond bias-voltage pulses.

The next chapter explores the preceding regime where the free-energy barrier separating the flux states is infinitesimal but nonzero. For a nonzero barrier, a stochastic phase slip, either via thermal activation over or via tunneling through the barrier, can occur. The rate of these phase slips depends on the height of the energy barrier. The next chapter formally introduces the concept of the free-energy barrier and delineates its dependence on the bias voltage, the parameters of the superconductor, and the geometry of the ring.

5

Stochastic Transitions between Flux States

For a superconducting ring to transition between its discrete flux states, the flux enclosed by the ring must be increased to the critical instability point for a *deterministic* phase slip. But as the flux increases, the energy barrier separating the flux states decreases, and the probability for a *stochastic* phase slip increases. At nonzero temperatures, thermal activation over the barrier can trigger a transition well before the critical flux. Likewise, tunneling through the barrier can trigger a transition, referred to as a quantum phase slip. This chapter presents the effect of a bias voltage on quantum phase slips in uninterrupted superconducting rings. I show that the bias voltage amplifies the rate of quantum phase slips up to the gigahertz range. The electronic control of this rate yields a phase-slip flux qubit with a broadly tunable transition frequency.

This chapter is organized as follows. In Section 5.1, deterministic, thermal, and quantum phase slips are compared qualitatively based on the free energy of an unbiased superconducting ring. Section 5.2 defines the free-energy barrier according to the Langer–Ambegaokar–McCumber–Halperin theory and numerically estimates the barrier height in the presence of a bias voltage. Next, Section 5.3 evaluates the rate of quantum phase slips as a function of the bias voltage and the geometry of the ring. Finally, in Section 5.4, I propose a novel phase-slip flux qubit whose transition frequency is tunable by the bias voltage and examine the sensitivity of the qubit to flux noise and device asymmetry.

5.1 Stochastic versus deterministic phase slips

The single-valuedness of the superconducting wave function dictates that the magnetic flux enclosed by a superconducting ring must be quantized; hence, the state of the ring can be characterized by the phase winding number n . To transition between these discrete states, the ring must surmount a finite energy barrier. This barrier originates from the need to locally suppress the Cooper-pair density to permit a jump in the phase winding number. The ring can overcome the energy barrier either deterministically or stochastically. The latter occurs via thermal activation over or tunneling through the energy barrier. This section reconciles the three mechanisms to escape a metastable flux state, namely deterministic, thermal, and quantum phase slips.

To that end, I qualitatively examine the free-energy spectrum of an isolated one-dimensional ring placed in a uniform magnetic field perpendicular to the plane of the ring. Starting from an initial flux state $n = 0$, the free energy of the ring rises as a function of the external flux. Beyond the degeneracy point $\phi = 1/2$, there exists a lower-current state $n = 1$. Nevertheless, the ring lingers in its initial state because there is a finite energy barrier for the transition [162]. If, however, the applied flux exceeds the critical value (4.11), fluctuations of the order parameter grow to nucleate a deterministic phase slip, and the ring transitions to the state $n = 1$ (Figure 5.1).

Close to the critical temperature of the superconductor, the initial flux state does not persist beyond the degeneracy point because thermal fluctuations supply the activation energy required to surmount the barrier to adjacent flux states. Therefore, thermally activated phase slips permit the ring to follow the state with the lowest free energy (Figure 5.1). The corresponding supercurrent exhibits a sawtooth form as a function of the flux and changes direction at half-integer flux quanta. The rate of thermally activated phase slips determines the lifetime of the metastable flux states.

In addition to thermal activation, a superconducting ring can escape from a metastable minimum of the free energy by tunneling through the energy barrier—that is, by quantum phase slips [163]. Quantum phase slips couple

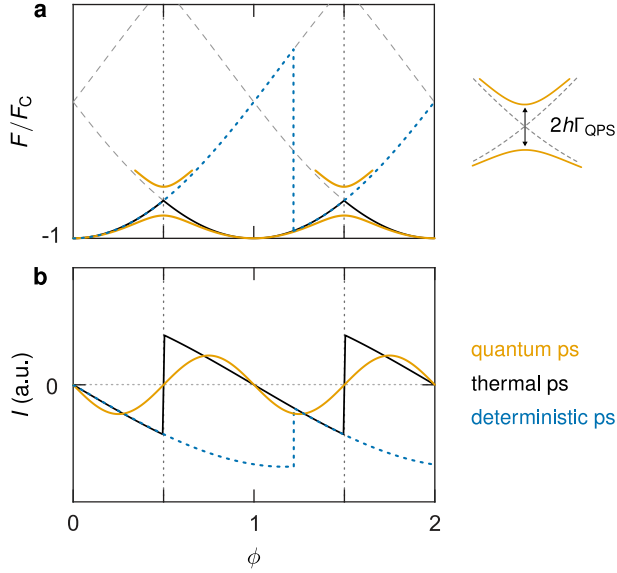


Figure 5.1 | Deterministic, thermal, and quantum phase slips. Free energy F (a) and persistent current (b) as a function of the normalized flux ϕ enclosed by a one-dimensional superconducting ring. The *blue* curve demonstrates a deterministic transition from the state $n = 0$ to $n = 1$ at the critical flux ϕ_c . The *black* curve corresponds to a ring at a temperature close to T_c , where thermally activated phase slips trigger transitions between the flux states. The *orange* curve accounts for coherent quantum phase slips, which result in level splitting at the degeneracy points $\phi = n + 1/2$.

the discrete flux states of a superconducting ring. This coupling is most prominent at the half-integer flux quanta because it results in an avoided crossing, as depicted in Figure 5.1 [69, 164]. For example, at $\phi = 1/2$, the two-level approximation of the Hamiltonian takes the form

$$\hat{\mathcal{H}} = I\Phi_0(\phi - 1/2)\sigma_z + h\Gamma_{\text{QPS}}\sigma_x, \quad (5.1)$$

where I is the persistent current and Φ_0 is the flux quantum. The Pauli spin matrices are denoted by σ_x and σ_z . The transition frequency of this two-level system depends on the rate Γ_{QPS} of quantum phase slips. Consequently, resolving this level splitting entails two constraints. First, the temperature must be low enough such that the rate of thermal phase slips is minimal, and quantum phase slips dominate. Second, the energy barrier must be suppressed to exponentially amplify the rate of quantum phase slips. In modern quantum

5. Stochastic Transitions between Flux States

phase-slip circuits, the barrier is reduced geometrically by interrupting the superconducting ring with a nanowire, which serves as a phase-slip center. In this work, however, the barrier is reduced electrically by voltage-biasing an uninterrupted superconducting ring.

5.2 Energy barrier for a stochastic phase slip

The theory of Langer, Ambegaokar, McCumber, and Halperin (hereafter LAMH) derives an expression for the free-energy barrier that a superconductor surmounts to escape a metastable local minimum of the free energy. This section highlights the main results of the LAMH theory, focusing on the passages between metastable flux states and the corresponding free-energy barrier. Moreover, it discusses how the energy barrier is extracted from the numerical solution of the time-dependent Ginzburg-Landau (GL) equations in the presence of a bias voltage.

5.2.1 LAMH Theory

The current-carrying states of a superconducting ring in a uniform magnetic field are the local minima of the GL free energy. These states are metastable because fluctuations of the order parameter can trigger interstate transitions to minimize the circulating supercurrent as the magnetic field increases. The barrier protecting against a current-decreasing transition is lower than that protecting against a current-increasing transition [65]. For instance, for a one-dimensional ring in the state $n = 0$ enclosing a flux $\phi = 1/2$, the barrier for the transition to the state $n = 1$ is lower than that to the state $n = -1$.

The minima of the free energy obey the time-independent GL equation

$$\left(\frac{i}{\kappa}\nabla + A\right)^2\psi - \psi + |\psi|^2\psi = 0. \quad (5.2)$$

Expressing the complex order parameter ψ in terms of a magnitude f and a phase χ leads to the imaginary part

$$2\chi'f' + \chi''f - 2\kappa Af' = 0, \quad (5.3)$$

where $\chi' \equiv d\chi/dx$ and $x \equiv R\theta$ with θ as the azimuthal angle. In a differential form, Equation (5.3) simplifies to

$$\frac{d}{dx}\left[f^2(\chi' - \kappa A)\right] = 0. \quad (5.4)$$

5. Stochastic Transitions between Flux States

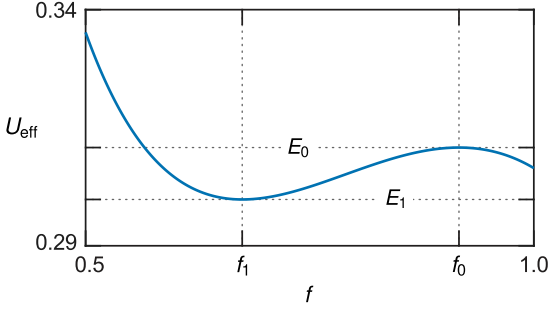


Figure 5.2 | Stationary metastable flux states. The effective potential U_{eff} , in the form (5.9), as a function of the magnitude f of the order parameter of a one-dimensional superconducting ring enclosing a magnetic flux $\phi = 2/5$. The metastable flux states are analogous to the circular orbits of a particle in an effective potential. The radii f_0 and f_1 represent circular orbits denoting the states $n = 0$ and $n = 1$, respectively.

Substituting with the supercurrent density

$$J_s = f^2 \left(\frac{\chi'}{\kappa} - A \right), \quad (5.5)$$

yields the stationarity condition

$$\frac{dJ_s}{dx} = 0, \quad (5.6)$$

which expresses that, for a state obeying the time-independent GL equation, the supercurrent density is uniform.

On the other hand, the real part of the GL equation (5.2) is written as

$$-f + f^3 + \frac{J_s^2}{f^3} - \frac{f''}{\kappa^2} = 0, \quad (5.7)$$

which can be cast in the differential form

$$\frac{1}{\kappa^2} \frac{d^2 f}{dx^2} = -\frac{\partial U_{\text{eff}}}{\partial f}, \quad (5.8)$$

where

$$U_{\text{eff}} \equiv \frac{f^2}{2} + \frac{J_s^2}{2f^2} - \frac{f^4}{4}. \quad (5.9)$$

The term U_{eff} is analogous to the effective potential regulating the orbital motion of a particle with a radial coordinate f and time x . For a metastable state, the order parameter is constant along the ring and, hence, the derivative

$$\frac{d^2 f}{dx^2} = 0, \quad (5.10)$$

which represents a particle whose radial coordinate is independent of time, i.e., a particle in a circular orbit (Figure 5.2). In other words, the metastable states denote the orbits for which the force on the particle is zero. Taking the analogy further, the conservation of the mechanical energy E of the particle takes the form

$$\frac{dE}{dx} \equiv \frac{d}{dx} \left[U_{\text{eff}} + \frac{(f')^2}{2\kappa^2} \right] = 0. \quad (5.11)$$

For a flux bias $\phi < 1/2$, there are two relevant circular orbits denoting two metastable states (Figure 5.2). The higher orbit—that is, the orbit with a higher magnitude f —corresponds to the state $n = 0$, while the lower orbit corresponds to the state $n = 1$. The mechanical energy, however, is not equivalent to the free energy since the smaller the radius, the lower the mechanical energy. Conversely, the lower the magnitude f , the higher the free energy.

According to the LAMH theory, the free-energy barrier separating two metastable states depends on the trajectory the ring traverses from one local minimum to the other [165]. These trajectories constitute the path of the lowest free energy connecting the two relevant minima. To complete a transition, the ring acquires activation energy to arrive at a saddle point in the free-energy landscape. Next, it slides downhill towards a configuration with a locally vanishing magnitude to permit a phase slip. Finally, it arrives at an adjacent local minimum with a different phase winding number. The LAMH theory characterizes these transitions by the saddle points, also referred to as saddle states, which obey the time-independent GL equation. In contrast to metastable states, the order parameter of a saddle state is not uniform along the circumference of the ring (Figure 5.3).

In the mechanical analogy, the particle transfers between two circular orbits by passing through an elliptical orbit for which the radial coordinate f is not

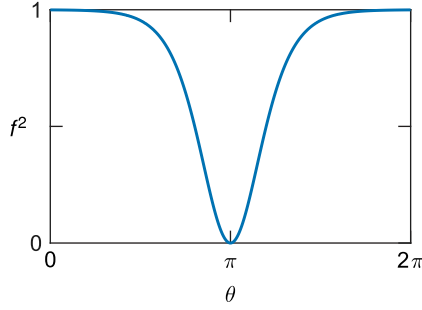


Figure 5.3 | Stationary saddle states. The squared magnitude of the order parameter of a saddle state along the circumference of a superconducting ring of radius $R = 2\xi$ and $\kappa = 1$, flux biased by $\phi = 1/2$. At the degeneracy points $\phi = n + 1/2$, the expression of the saddle-state density reduces to $\tanh^2(\kappa R\theta/\sqrt{2})$, as derived in Appendix E.

constant. This elliptical orbit satisfies the stationarity condition

$$\frac{dE_s}{dx} = 0, \quad (5.12)$$

where E_s is the mechanical energy. The mechanical energy of the elliptical orbit is lower than that of the initial circular one. Thus, the free energy of the saddle state is higher than the initial metastable state, which explains the need for thermal activation over or tunneling through a finite energy barrier.

The energy barrier ΔF is defined as the difference between the free energy of the saddle state and the free energy of the initial metastable flux state, i.e.,

$$\Delta F \equiv F_s - F_n, \quad (5.13)$$

where the free energy F_n is labeled by the flux state n and depends on the magnetic flux enclosed by the ring. The free energy of the saddle state is derived through the stationarity condition (5.11). The details of the derivation are presented in Appendix E. Here, however, I highlight the main results based on [62, 166–170]. For a ring whose circumference $L \gg \xi$, the free energy of the saddle state takes the form

$$F_s = -F_C \left[\frac{(2 + \nu)^2}{9} - \frac{8}{3} \frac{\xi}{L} \sqrt{2\nu} \right], \quad (5.14)$$

where ν is a parameter denoting the difference between the maximum and the minimum of the magnitude of saddle-state order parameter. The parameter ν

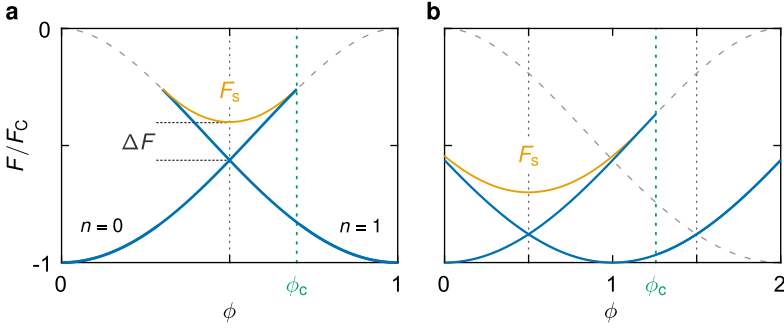


Figure 5.4 | Free energy of the saddle state. Free energy F , normalized by the condensation energy F_C , of a superconducting ring of radius $R = \xi$ (a) and $R = 2\xi$ (b) as a function of the enclosed magnetic flux ϕ . The blue curve is obtained by the numerical solution of the time-dependent GL equations, where a deterministic phase slip occurs at ϕ_c . The saddle-state free energy F_s is based on Equation (5.14). The free-energy barrier for a stochastic phase slip is denoted by ΔF .

can be determined by the transcendental equation

$$2\pi n = 2\pi\phi + \frac{L}{\xi} \sqrt{\frac{1-\nu}{3}} + 2 \arctan \sqrt{\frac{3\nu}{2-2\nu}}, \quad (5.15)$$

as a function of the flux ϕ . The free energy of the saddle state converges to that of the metastable state at the critical flux (4.11). Put differently, the free-energy barrier vanishes at the instability point, which differentiates a stochastic phase slip that occurs below the critical flux ϕ_c from a deterministic phase slip that occurs at ϕ_c (Figure 5.4).

If the radius $R \gg \xi$, then the parameter ν is approximately unity, and the barrier simplifies to

$$\Delta F \approx F_C \left[\frac{8\sqrt{2}}{3} \frac{\xi}{L} - \frac{2\xi^2}{R^2} (n - \phi)^2 \right]. \quad (5.16)$$

In the absence of an external magnetic field, the barrier takes the form

$$\begin{aligned} \Delta F &= \frac{8\sqrt{2}}{3} \frac{\xi}{L} F_C \\ &= \frac{8\sqrt{2}}{3} \frac{B_{\text{cth}}^2}{2\mu_0} w d \xi, \end{aligned} \quad (5.17)$$

as derived by the LAMH theory for a one-dimensional superconducting nanowire of length L . The product wd is the cross-sectional area, and B_{cth} is the thermodynamic critical field. The barrier is linearly proportional to the product of the cross-sectional area and the coherence length. This product denotes the volume over which the magnitude of the order parameter is suppressed to allow a phase discontinuity. Because their rate depends on the barrier height exponentially, quantum phase slips are observed in superconducting wires that are only a few nanometers in width [68, 84–86]. If the nanowire is to be replaced by a thick ring, one must compensate for the increase in the cross-sectional area to maintain the same barrier and the same phase-slip rate. In other words, to alleviate the stringent requirements on the dimensions of the superconductor, one must employ an additional barrier-reducing mechanism to compensate for the increased area and, in turn, to preserve the rate of quantum phase slips. In this chapter, I demonstrate that the bias voltage modulates the height of the energy barrier and amplifies the rate of quantum phase slips.

The rate of stochastic phase slips

In the original formulation of the LAMH theory, the energy required to surmount the free-energy barrier is provided by thermal activation. The rate of thermally activated phase slips follows the Arrhenius law

$$\Gamma_{\text{TAPS}} = \omega e^{-\Delta F/k_{\text{B}}T}, \quad (5.18)$$

where k_{B} is the Boltzmann constant, and the attempt frequency ω is given by

$$\omega = \frac{1}{\tau} \frac{L}{\xi} \sqrt{\frac{\Delta F}{k_{\text{B}}T}}. \quad (5.19)$$

with the relaxation time τ defined as

$$\tau \equiv \frac{\pi \hbar}{8k_{\text{B}}(T_{\text{c}} - T)}. \quad (5.20)$$

Because a phase slip extends over a length ξ , the ratio L/ξ represents the number of independent locations in the superconductor where a phase slip can occur [4]. Therefore, the longer the superconductor, the more frequent the attempts to escape the present metastable state.

Analogously, the rate of quantum phase slips is obtained by replacing the thermal energy $k_B T$ by \hbar/τ , leading to the expression [76]

$$\Gamma_{\text{QPS}} = B \omega e^{-a\Delta F\tau/\hbar}, \quad (5.21)$$

where a and B are numerical factors of order unity. The attempt frequency is also modified accordingly. This phenomenological model has been shown to accurately fit the resistance of ultra-thin wires [68, 79, 80]. Other models for calculating the rate of quantum phase slips can be found in [64, 76, 78].

5.2.2 Free-energy barrier in the presence of bias voltage

In Chapter 4, I have demonstrated that the bias voltage provides complete control over the critical flux for a deterministic phase slip, or equivalently over the free-energy barrier separating adjacent flux states. The height of the free-energy barrier, however, cannot be directly computed from the numerical solution of the time-dependent Ginzburg-Landau equations. Specifically, the energy of the saddle state cannot be determined because the temporal evolution of the order parameter does not traverse the saddle-state trajectory but advances till the instability point at which a deterministic transition occurs (Figure 5.5a). Several numerical techniques have been proposed to calculate the energy of the saddle state such as [171–173].

In this work, I estimate the height of the free-energy barrier by scrutinizing two key properties of the saddle state. First, the energy of the saddle state equals that of a metastable flux state at the critical flux ϕ_c (Figure 5.5a). Second, near the degeneracy points $\phi = n + 1/2$, the energy of the saddle is weakly dependent on flux, and its first derivative equals zero. Now, because the critical flux tends to the degeneracy points as a function of the bias voltage, the barrier between the two states n and $n + 1$ can be conservatively approximated by

$$\Delta F \approx F(\phi_c) - F(n + 1/2), \quad (5.22)$$

provided the voltage is high enough to reduce the instability point to the vicinity of $\phi = n + 1/2$. The barrier (5.22) can be extracted from the numerical solution of the time-dependent Ginzburg-Landau equations (Figure 5.5b). More important, it is in this validity regime—defined by $\phi_c \sim n + 1/2$ —that the barrier is low enough for a phase-slip rate in the gigahertz range.

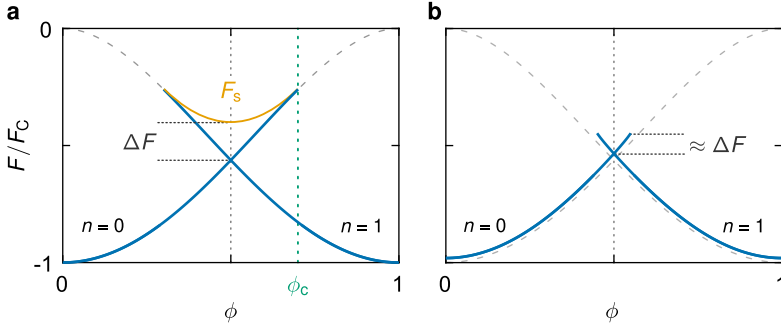


Figure 5.5 | Free-energy barrier ΔF for a voltage-biased superconducting ring. Free energy of a ring of radius $R = \xi$. **a** | The saddle-state energy F_s characterizes the trajectory spanned by the ring to escape from one minimum of the free energy to another. **b** | In the presence of a bias voltage high enough to reduce the critical flux ϕ_c to the vicinity of $\phi = 1/2$, a conservative estimate of the free-energy barrier can be extracted from the numerical solution of the TDGL equations in the form (5.22).

The attempt frequency (5.19) also must be modified. For an unbiased ring, the magnitude of the order parameter is uniform, and the free-energy barrier is identical along the circumference of the ring. The attempt frequency is therefore proportional to the ratio L/ξ , characterizing the number of independent locations where a phase slip can occur. Conversely, for a biased ring, the magnitude of the order parameter is nonuniform, and there is a preferential location for the minimum value of the saddle state and, hence, for the phase slip. As a consequence, the barrier is not uniformly suppressed, and there is a single location in the ring where attempts to escape the metastable flux state encounter a reduced barrier. For other locations, the barrier is effectively uninfluenced. To incorporate this nonuniformity, the ring is divided into two sections: a section of length ξ for which the barrier is reduced due to the presence of a bias voltage, and a section of length $L - \xi$ for which the barrier is unreduced. The rate of phase slips occurring in the latter is much lower than the former owing to the exponential dependence of the rate on the height of the barrier. Accordingly, in the presence of a bias voltage, I modify the attempt frequency to

$$\omega = \frac{1}{\tau} \sqrt{\frac{\Delta F \tau}{\hbar}}. \quad (5.23)$$

5.3 Suppression of energy barrier by bias voltage

To tune the transition frequency of a qubit based on the Josephson junction, the junction is exchanged by two in parallel to create a dc SQUID. The overall magnetic flux enclosed by the SQUID determines the effective Josephson energy and, in turn, the transition frequency of the qubit. The additional flux-bias loop, however, renders the qubit sensitive to flux noise, which limits its dephasing time [31–33]. This drawback motivates the need for creating electrically tunable weak links—for example, by placing a superconductor in a planar electric field that locally suppresses the Cooper-pair density [174, 175]. In this work, I suggest using a bias voltage to induce a weak link in a superconducting ring as a means to enhance the rate of quantum phase slips.

This section calculates the free-energy barrier for voltage-biased aluminum nanorings and the rate of quantum phase slips. The bias voltage enhances the phase-slip rate to the gigahertz range, thereby offering a route to realizing a phase-slip flux qubit with an electrically tunable transition frequency. The purpose of this section is not to contend the optimal material choice for a phase-slip qubit but to demonstrate the enhancement of the quantum-phase-slip rate in a prototypical superconductor such as aluminum and to assess the dependence of the rate on control parameters including the size of the ring, the coherence length of the superconductor, and the geometry of the bias electrodes. This analysis yields several insights into the operation of the proposed qubit and a roadmap for further improvement.

The parameters for aluminum are consistent with Chapter 4. Specifically, the critical temperature T_c equals 1.32 K. In this section, the operating temperature equals $T_c/2$ to ensure that thermally activated phase slips are suppressed and that quantum phase slips dominate. Although the Ginzburg-Landau equations are derived in the immediate vicinity of the critical temperature, they have been extensively employed in literature, and their predictions agree well with experiments even at temperatures that differ moderately from the critical temperature. The length scales of the superconductor—namely, the coherence length and the penetration depth—are calculated using the empirical temperature dependence in Section 2.2.2.

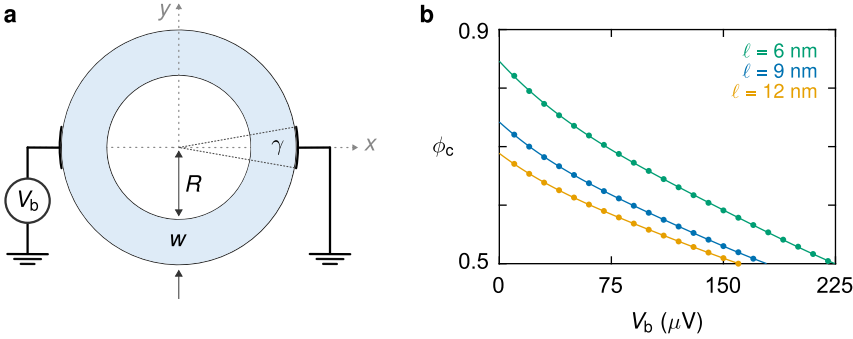


Figure 5.6 | Critical flux as a function of the mean free path ℓ . **a** | Schematic of a voltage-biased superconducting ring. **b** | The critical flux ϕ_c for a deterministic transition from the flux state $n = 0$ to $n = 1$ as a function of the bias voltage V_b , for three aluminum rings of different ℓ . The radii of the rings $R = 100$ nm, and their widths $w = 100$ nm. Dots represent the simulated data points using the time-dependent Ginzburg-Landau equations. The angle of the bias electrodes $\gamma = 18^\circ$.

The bias voltage is applied along the outer perimeter of the ring. The arc length of the bias electrode is characterized by the angle γ (Figure 5.6a). To symmetrically couple the two neighboring flux states $n = 0$ and $n = 1$, the flux bias is applied locally within the ring, and the angle between the bias electrodes is set to π (see Figures 4.5 and 4.6 for a comparison between a local and a uniform flux bias). For a ring of radius $R = 100$ nm and width $w = 100$ nm, I analyze the relation between the bias voltage and the free-energy barrier (5.22) as a function of the size of the ring, the arc length of the bias electrodes, and the parameters of the superconductor.

Motivated by the inevitable disorder in experimentally deposited samples, I vary the mean free path ℓ . For each mean free path, the resistivity of the normal state follows the well-known relation $\rho\ell = 4 \times 10^{-6} \mu\Omega \cdot \text{cm}^2$ for aluminum thin films [160]. In the dirty limit, the mean free path alters the coherence length and the penetration depth according to Equations (2.26) and (2.27), respectively. Using the time-dependent Ginzburg-Landau equations, I compute the critical flux ϕ_c for a deterministic transition from the flux state $n = 0$ to $n = 1$ as a function of the bias voltage for $\ell = 6, 9,$ and 12 nm (Figure 5.6b). The corresponding coherence lengths are $\xi(T) = 110, 135,$ and 150 nm. A longer

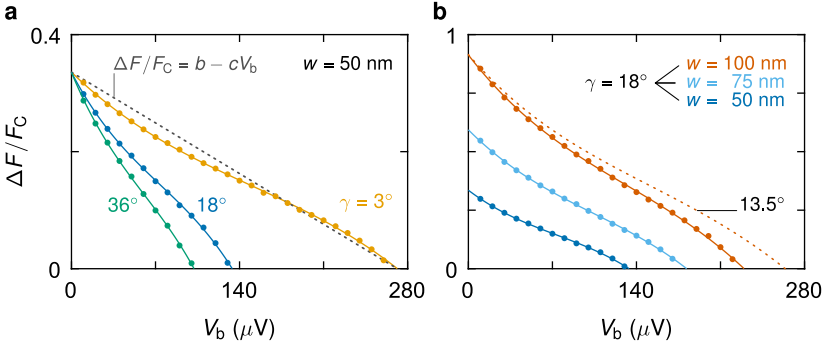


Figure 5.7 | Voltage-induced suppression of the free-energy barrier. **a** | Free-energy barrier ΔF , normalized by the condensation energy F_C , for a superconducting ring of radius $R = 100$ nm and width $w = 50$ nm for various bias-contact angles γ (see a model in Figure 5.6a). The dotted line represents the linear approximation (5.25). **b** | Free-energy barrier ΔF , normalized by the condensation energy of the ring of width 50 nm, for a bias-contact angle $\gamma = 18^\circ$. The dotted line corresponds to an angle $\gamma = 13.5^\circ$ and a width $w = 100$ nm for comparison with the curve of $(w, \gamma) = (50 \text{ nm}, 18^\circ)$ to preserve the $\gamma(R + w)$ product. Dots represent the simulated data points using the time-dependent GL equations. Parameters used: mean free path $\ell = 6$ nm and $\xi(T) = 110$ nm.

mean free path produces a longer coherence length. Therefore, the ratio of the width of the ring to the coherence length decreases, and the effective width tends to the one-dimensional limit defined by $w \ll \xi$. Thus, the zero-bias critical flux follows the instability criterion (4.11). Moreover, in agreement with Figure 4.4a, the critical flux increases as the ratio of the radius to the coherence length increases. As a function of the bias voltage, the critical flux decreases monotonically to the half-flux-quantum degeneracy point. To focus solely on the geometry of the biased ring, the subsequent analysis assumes a specific choice of the mean free path, namely $\ell = 6$ nm.

First, I vary the arc length of the bias electrodes in a ring of radius $R = 100$ nm and width $w = 50$ nm. Near the electrodes, the injected normal current converts into a supercurrent that flows along the two arms of the ring. The amount of the injected current scales with the arc length of the electrodes. Therefore, the angle γ determines the effectiveness of the bias voltage in modulating the free-energy barrier. Explicitly, the slope of the relation between the free-energy

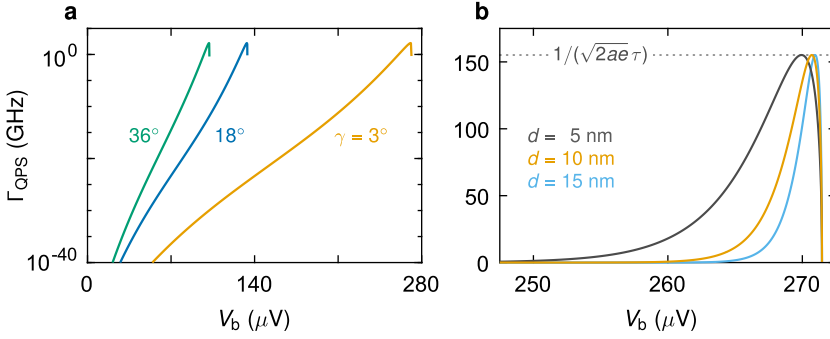


Figure 5.8 | Electronic control of quantum phase slips. **a** | The rate of quantum phase slips Γ_{QPS} as a function of the bias voltage V_b . The rate is calculated using equation (5.21) for $B = 1$, $a = 0.37$, and a thickness $d = 10$ nm based on the free-energy barriers in Figure 5.7a. **b** | Sensitivity of the highest rate for three ring thicknesses, namely $d = 5$, 10, and 15 nm. The dotted line denotes the maximum frequency (5.31). Parameters used: $\ell = 6$ nm, $R = 100$ nm, and $w = 50$ nm.

barrier and the bias voltage depends on the angle γ (Figure 5.7a). A smaller angle results in a steeper slope, implying a reduced sensitivity to bias voltage.

Second, I vary the width of the ring while keeping the angle of the bias electrodes unchanged. Because the condensation energy of the ring scales with its width, a larger width leads to a higher free-energy barrier at zero bias voltage, in line with the barrier expression (5.17). Therefore, a higher bias voltage is required to completely suppress the barrier (Figure 5.7b). To decouple the effect of enlarging the ring from the increased arc length of the bias electrodes, I include the dotted curve for $w = 100$ nm and $\gamma = 13.5^\circ$ to preserve the product $\gamma(R + w)$ compared to the blue curve for $w = 50$ nm and $\gamma = 18^\circ$. The comparison of these two curves reveals almost identical slopes of the free-energy barrier. Incidentally, for precise control of the barrier and the rate of quantum phase slips, the width of the ring must be comparable to its radius. This requirement ensures that the supercurrent induced by the bias voltage flows predominantly along the azimuthal direction. Otherwise, the radial component of the supercurrent dominates and strongly suppresses the Cooper-pair density near the electrodes, which changes the preferential location for nucleating phase slips (Figure 3.8).

Based on the height of the barrier, I evaluate the rate of quantum phase slips in the strong damping regime with $a = \pi/6\sqrt{2} \approx 0.37$ and $B = 1$ [75]. The rate increases exponentially as a function of the bias voltage, up to the gigahertz range (Figure 5.8). Moreover, increasing the thickness d of the superconductor decreases the rate since the overall condensation energy of the ring scales with its cross-sectional area, in agreement with the free-energy barrier (5.17).

At half a flux quantum ($\phi = 1/2$), the two states $n = 0$ and $n = 1$ are degenerate and can be coherently coupled via quantum phase slips, a phenomenon dubbed coherent quantum phase slips. Due to this coupling, the eigenstates of the ring are the symmetric and the antisymmetric superpositions of these two flux states, corresponding to a superposition of a clockwise and a counterclockwise supercurrents. The two relevant energy levels define a phase-slip flux qubit whose level spacing depends on the rate of quantum phase slips. The next section formally defines the two-level system for this qubit and analyzes its performance in the presence of magnetic flux noise and material defects.

5.4 Proposal for a phase-slip flux qubit

The lowest two energy levels of a voltage-biased superconducting ring that encloses half a flux quantum are described by the Hamiltonian

$$\hat{\mathcal{H}} = h\Gamma_{\text{QPS}}(V_b) \sigma_z, \quad (5.24)$$

up to a constant energy shift corresponding to the operating point $F(\phi = 1/2)$. The level splitting depends on the rate of quantum phase slips Γ_{QPS} . Because the subsequent flux states with $n \neq 0$ or 1 are much higher in energy, this isolated two-level system defines a strongly anharmonic flux qubit. This section scrutinizes the operation of this qubit, focusing on the electronic tunability of the transition frequency and on the qubit sensitivity to magnetic flux noise and defects that break the symmetry of the ring.

5.4.1 Electronic tunability of the transition frequency

The level splitting of the proposed flux qubit depends on the rate of quantum phase slips that coherently couple the two flux states $n = 0$ and $n = 1$ at a flux bias $\phi = 1/2$. Because of the exponential dependence of the rate on the bias voltage, variations in the voltage source can cause qubit dephasing. This section assesses the electronic tunability of the qubit as a function of the bias voltage and its sensitivity to charge fluctuations.

The sensitivity of the qubit hinges on the slope of the relation between the free-energy barrier and the bias voltage (Figure 5.7) and, thus, can be examined by approximating the free-energy barrier by the linear relation

$$\frac{\Delta F}{F_C} = b - cV_b, \quad (5.25)$$

where b is the normalized free-energy barrier at zero bias voltage, and c is the slope. Substituting with the linearized barrier expression into the quantum-phase-slip rate (5.21) leads to

$$\Gamma_{\text{QPS}} = \frac{1}{\tau} \sqrt{\frac{\epsilon}{a}} (b - cV_b)^{1/2} \exp[-\epsilon(b - cV_b)], \quad (5.26)$$

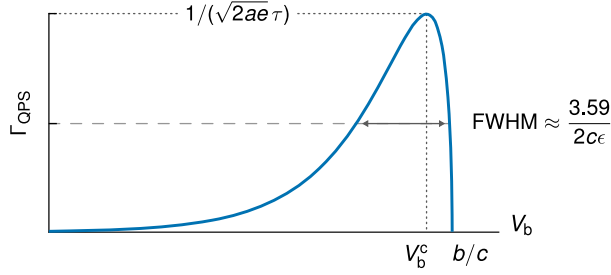


Figure 5.9 | Electronic tunability of a phase-slip qubit comprising a voltage-biased superconducting ring, enclosing half a flux quantum. The rate of quantum phase slips Γ_{QPS} in the form (5.26) is plotted as a function of the bias voltage V_b . The tunability is characterized by the full width of V_b at half maximum of the rate. The parameter c is the slope of the relation between the free-energy barrier and V_b , b denotes the zero-bias free-energy barrier, normalized by the condensation energy F_C , and $\epsilon \equiv a\tau\hbar/F_C$, where the relaxation time τ is defined in equation (5.20).

with the dimensionless constant ϵ is defined as

$$\epsilon \equiv a \frac{\tau F_C}{\hbar}. \quad (5.27)$$

The rate of quantum phase slips equals zero at a bias voltage $V_b = b/c$. To extend the range of the bias voltage, the zero-bias barrier b must be increased by employing a superconducting ring of larger width (Figure 5.7b).

Substituting with the dimensionless variable x defined as

$$x \equiv \epsilon(b - cV_b), \quad (5.28)$$

into the rate (5.26) produces the succinct expression

$$\Gamma_{\text{QPS}} = \frac{1}{\tau} \sqrt{\frac{x}{a}} e^{-x}. \quad (5.29)$$

Maximizing the rate (5.29) results in the critical bias voltage

$$V_b^c = \frac{b}{c} - \frac{1}{2c\epsilon}, \quad (5.30)$$

at which the highest quantum-phase-slip rate reads

$$\Gamma_{\text{max}} = \frac{1}{\sqrt{2ae}} \frac{1}{\tau}. \quad (5.31)$$

5. Stochastic Transitions between Flux States

For a fixed-frequency operation, it is optimal to operate at the sweet spot V_b^c where the rate is insensitive to charge fluctuations in the first order. The tunability of the transition frequency can be characterized by the full width of the bias voltage at half maximum of the quantum-phase-slip rate. To that end, substituting with $\Gamma_{\max}/2$ into the rate (5.29) leads to the equation

$$\frac{1}{2\sqrt{2e}} = \sqrt{x}e^{-x}, \quad (5.32)$$

with the two real solutions

$$V_b^+ = \frac{1}{2c\epsilon} \left[2b\epsilon + W\left(\frac{-1}{4e}\right) \right], \quad (5.33)$$

and

$$V_b^- = \frac{1}{2c\epsilon} \left[2b\epsilon + W_{-1}\left(\frac{-1}{4e}\right) \right], \quad (5.34)$$

where W is the Lambert function, defined as the inverse of $g(W) = W \exp(W)$. The full width at half maximum takes the form

$$V_b^+ - V_b^- = \frac{1}{2c\epsilon} \left[W\left(\frac{-1}{4e}\right) - W_{-1}\left(\frac{-1}{4e}\right) \right], \quad (5.35)$$

To reduce the sensitivity of the qubit to bias voltage, the arc length of the bias electrodes must be minimized, seeing that it is proportional to the slope c (Figure 5.7a). In addition, the parameter ϵ can be minimized by operating at a lower temperature to decrease the relaxation time τ , or by using a ring of smaller thickness d to reduce the condensation energy F_C (Figure 5.8b).

To sum up, the modulation of the quantum-phase-slip rate via bias voltage enables electronic tunability of the transition frequency of the proposed qubit. But it also renders the qubit prone to dephasing in the presence of charge noise or variations in the voltage source. For example, as captured by Figure 5.8b, owing to the exponential dependence of the rate on the barrier height, voltage fluctuations in the order of $1\mu V$ shift the rate by a few gigahertz.

5.4.2 Sensitivity to low-frequency flux noise

Over the past two decades, the coherence times of superconducting qubits have improved by a few orders of magnitude. This improvement is attributed to two key factors: the reduction of noise via progress in qubit materials and fabrication; and the reduction of the qubit noise sensitivity via design advances [35]. The transmon is a quintessential example of the latter [41]. Unlike the Cooper-pair box whose coherence time was in the nanosecond range, the transmon exhibits coherence times up to a hundred microseconds. This leap has been achieved by incorporating a large shunt capacitance, which reduces the qubit sensitivity to charge fluctuations, and by embedding the transmon into a microwave resonator—an architecture known as circuit quantum electrodynamics. Likewise, the coherence times of flux qubits have been improved, most recently by including a large shunt capacitance, giving rise to the C-shunt flux qubit [35]. Compared with conventional flux qubits, the C-shunt variant is less sensitive to low-frequency flux noise.

In general, low-frequency flux noise is a dominant source of decoherence in flux qubits, as well as other qubit implementations for which the Josephson junction is replaced by a dc SQUID to enable magnetic tunability of the transition frequency. The power spectral density of the flux noise scales with $1/f^u$ where f is the frequency and u is of order unity [176, 177]. Moreover, the flux noise is independent of the superconducting material and the geometry of the device [178]. Low-frequency flux noise is still a subject of active research and is likely caused by randomly oriented magnetic defects and surface spins [179]. Nevertheless, from a design perspective, the solution is to minimize the sensitivity of the qubit to variations in the magnetic flux.

This section qualitatively evaluates the sensitivity of the proposed qubit to variations in the flux bias, due to either fluctuations in the biasing circuit or flux noise [180]. The latter is expected to be considerably lower than Josephson-based qubits since the random reversal of electron spins at the interface between the superconductor and the insulating barrier is believed to be a likely source of low-frequency flux noise [181–183]. Accordingly, in a junction-less, uninterrupted superconducting ring, low-frequency flux noise is expected to be substantially reduced.

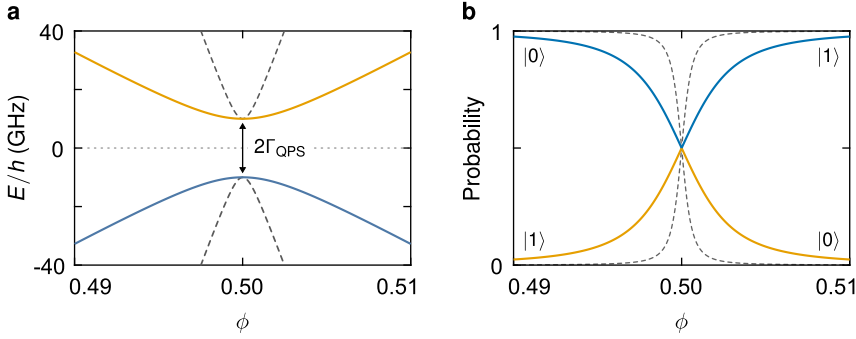


Figure 5.10 | Qubit sensitivity to flux noise. **a** | The ground and the first excited states of the proposed phase-slip flux qubit as a function of the normalized flux bias ϕ based on the two-level Hamiltonian (5.36). **b** | Probability of the first two eigenstates, or the two flux states $n = 0$ and $n = 1$. The quantum-phase-slip rate Γ_{QPS} is 10 GHz. The persistent current I equals $1 \mu\text{A}$ for the solid line and $5 \mu\text{A}$ for the dotted line.

For a voltage-biased superconducting ring whose flux states are coherently coupled by quantum phase slips, the two-level Hamiltonian takes the form

$$\hat{\mathcal{H}} = I\Phi_0(\phi - 1/2)\sigma_z + h\Gamma_{\text{QPS}}\sigma_x, \quad (5.36)$$

where ϕ denotes the normalized flux, and I is the persistent current. For a ring whose radius is in the order of hundreds of nanometers, the persistent current amounts to a few microamperes. The eigenvalues of this Hamiltonian are depicted in Figure 5.10 as a function of ϕ . At half a flux quantum ($\phi = 1/2$), the eigenstates are the symmetric and antisymmetric superpositions of the two flux states $n = 0$ and $n = 1$. Incidentally, the superposition of two macroscopic flux states was first measured in [184–186] for superconducting loops incorporating one or more Josephson junctions.

Diagonalizing the Hamiltonian (5.36) leads to the level splitting

$$h\nu_{01} = \left[(2h\Gamma_{\text{QPS}})^2 + \mathcal{E}^2 \right]^{1/2}, \quad (5.37)$$

where $\mathcal{E} \equiv 2I\Phi_0(\phi - 1/2)$. The sensitivity of the splitting to flux noise can be defined as [180]

$$D_\phi \equiv \frac{\partial \nu_{01}}{\partial \phi} = \frac{\mathcal{E}}{h} \left[(2h\Gamma_{\text{QPS}})^2 + \mathcal{E}^2 \right]^{-1/2} \frac{\partial \mathcal{E}}{\partial \phi}. \quad (5.38)$$

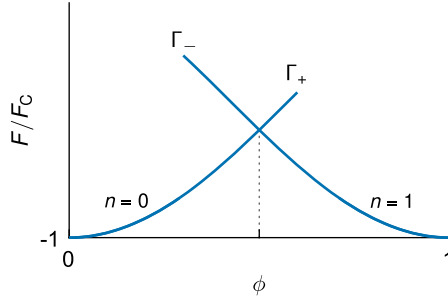


Figure 5.11 | Asymmetric free-energy barriers. Free energy of a superconducting ring that is asymmetric due to defects or unbalanced bias electrodes (Figure 4.5). The barrier for the transition from $n = 0$ to $n = 1$ is lower than that for the reverse transition. The corresponding quantum-phase-slip rates are asymmetric as well.

At the half-flux-quantum degeneracy point, the qubit is insensitive to flux fluctuations up to first order. Away from the degeneracy point and in the limit $\mathcal{E} \gg h\Gamma_{\text{QPS}}$, the sensitivity reduces to

$$D_\phi \approx \frac{2I\Phi_0}{h}, \quad (5.39)$$

implying that the qubit becomes less sensitive to flux noise as the persistent current decreases (Figure 5.10). In other words, for a higher persistent current, the degeneracy between the flux states $n = 0$ and $n = 1$ is rapidly lifted as the flux deviates from the degeneracy point, and the eigenstates consist predominately of one of the two flux states instead of an equal mixture (Figure 5.10b). Moreover, the higher the qubit transition frequency—encoded here by the rate of quantum phase slips—the lower the sensitivity to flux noise.

For a ring enclosing half a flux quantum, a larger radius leads to a lower persistent current and, hence, a reduced sensitivity to magnetic flux noise. This requirement, however, conflicts with the sensitivity of the quantum-phase-slip rate to charge fluctuations. Specifically, a larger radius exacerbates the decent rate of the free-energy barrier with respect to the bias voltage, which renders the qubit more sensitive to charge fluctuations as captured in Figure 5.9.

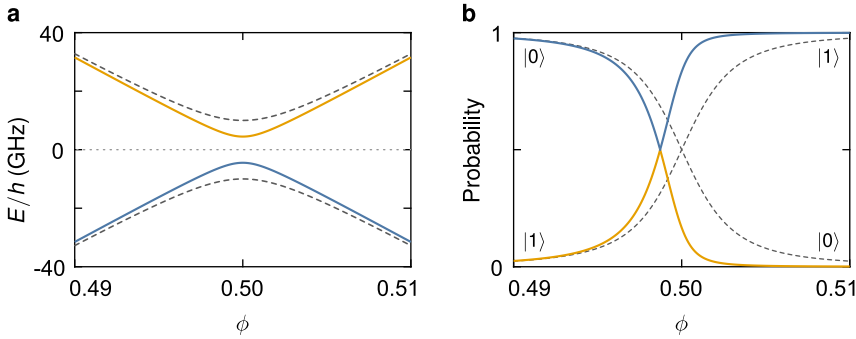


Figure 5.12 | Effect of asymmetry on qubit level spacing. **a** | The ground and the first excited states of the proposed phase-slip flux qubit as a function of the magnetic flux bias ϕ based on the two-level Hamiltonian (5.36) where the rate of quantum phase slip is expressed in the matrix form (5.40). **b** | Probability of the first two eigenstates, or the two flux states $n = 0$ and $n = 1$. The persistent current I equals $1 \mu\text{A}$. For the dotted line, the rate $\Gamma_+ = \Gamma_- = 10 \text{ GHz}$. For the solid line, $\Gamma_+ = 10 \text{ GHz}$ and $\Gamma_- = 2 \text{ GHz}$.

5.4.3 Tolerance to device asymmetry

The primary advantage of the phase-slip flux qubit is that the rate of quantum phase slips depends on macroscopic parameters—namely, the geometry of the ring and the coherence length of the superconductor. As a consequence, it is immune to defects occurring on a length much smaller than the coherence length, as evidenced by the fidelity of the superconducting memory presented in Chapter 4. In addition, because the bias voltage provides complete control over the free-energy barrier, it can compensate for small deviations of the superconductor parameters to ensure a well-defined transition frequency.

But the proposed qubit is sensitive to defects that break the symmetry of the ring on a scale comparable to the coherence length. Unlike nanowire-based qubits where all phase slips preferentially occur in the nanowire, in an uninterrupted ring the bias voltage induces two weak links. Based on the phase winding number, the preferential location alternates between the upper and lower arms of the ring. Put differently, transitions that increment the phase winding number—referred to hereafter as forward transitions—and those that decrement it—referred to hereafter as backward transitions—occur at two distinct locations in the ring. Accordingly, in the presence of defects that break

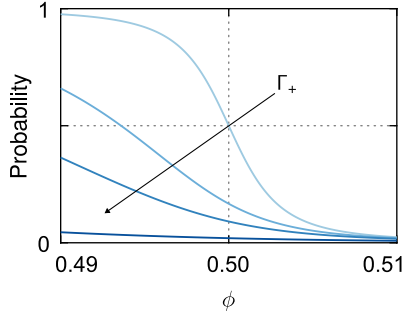


Figure 5.13 | Eigenstates for asymmetric quantum-phase-slip rates. Probability of the flux state $n = 0$ as a function of the normalized flux bias ϕ for forward quantum-phase-slip rates $\Gamma_+ = 10, 50, 100,$ and 500 GHz, where the arrow indicates the direction of increasing rate. The backward rate Γ_- is fixed at 10 GHz by increasing the bias voltage. The persistent current I equals $1 \mu\text{A}$.

the symmetry of the ring, the free-energy barriers encountered by forward and backward transitions are not identical (Figure 5.11). This asymmetry can be caused by defects that suppress the density of Cooper pairs at one side of the ring or by deviations of the angle between the bias electrodes (Figure 4.5).

The effect of asymmetry can be analyzed by replacing the phase-slip rate Γ_{QPS} in the two-level Hamiltonian (5.36) by the diagonal matrix

$$\Gamma_{\text{QPS}} = \begin{pmatrix} \Gamma_+ & 0 \\ 0 & \Gamma_- \end{pmatrix}, \quad (5.40)$$

where Γ_+ represents the rate of quantum phase slips that increments the phase winding, and Γ_- represents those that decrement the phase winding number. For unequal rates, the eigenstates of the qubit at the degeneracy point no longer consist of equal contributions of the flux states $n = 0$ and $n = 1$ (Figure 5.12).

Moreover, although the bias voltage spans the entire range of the free-energy barrier, it cannot compensate for the asymmetry originating from defects that are comparable in size to the coherence length of the superconductor. For instance, in Figure 5.12, if the bias voltage is increased to restore the backward rate Γ_- to its original value, the forward rate Γ_+ increases simultaneously, and the contribution of the state $n = 0$ decreases and tends to zero as the voltage

increases (Figure 5.13). A zero contribution of the state $n = 0$ corresponds to a deterministic phase slip that increments the winding number to $n = 1$. If the ring transitions to the subsequent flux state deterministically, then the two flux states are no longer coherently coupled.

In sum, proper operation of the qubit requires symmetry of the voltage-biased superconducting ring on the scale of the coherence length. As discussed in Chapter 3, the formation of two weak links using a bias voltage entails designing the dimensions of the ring to be comparable to the coherence length. As a consequence, potential defects in the ring are axiomatically smaller than the coherence length. These defects can be tolerated and do not disturb the operation of the proposed qubit.

5.4.4 Measuring the rate of quantum phase slips

To validate the proposal of the flux qubit, the rate of quantum phase slips must be measured as a function of the bias voltage. For a superconducting ring enclosing half a flux quantum, this rate corresponds to the energy difference between the ground and first excited states (Figure 5.10). This energy difference can be measured with microwave spectroscopy, in line with the experiments conducted on superconducting loops interrupted by Josephson junctions. This section delineates the measurement process according to [186].

The eigenstates of the two-level Hamiltonian (5.36) at a flux bias $\phi = 1/2$ are the symmetric and antisymmetric superpositions of the two macroscopic flux states $n = 0$ and $n = 1$. The persistent current is zero for both states (Figure 5.14b), and they are therefore indistinguishable at the degeneracy point $\phi = 1/2$. Consequently, the measurement relies on sweeping the flux bias nearby the degeneracy point—for example, from $\phi = 0.49$ to 0.51 —to break the symmetry and to distinguish the two states based on the flux induced by the circulating current. Specifically, the qubit—that is, the voltage-biased superconducting ring—is enclosed within a dc SQUID that detects the overall flux (i.e., the flux bias ϕ in addition to the flux induced by the circulating current in the ring). Changes in the persistent current as the flux bias is swept modulate the maximum supercurrent that can flow through the SQUID. For

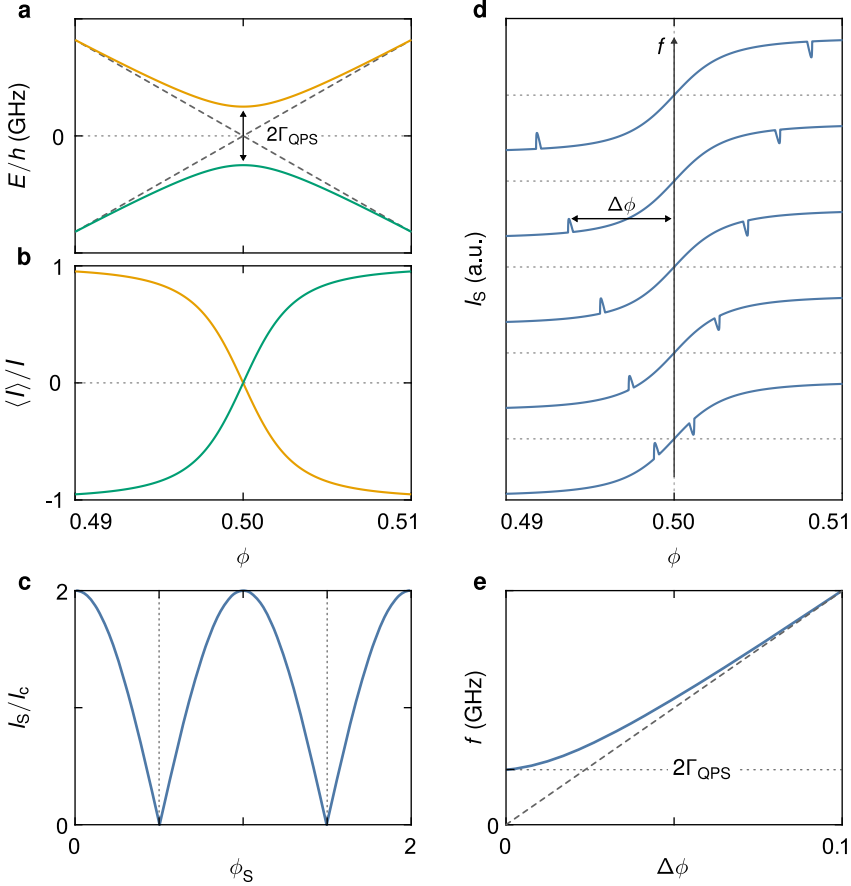


Figure 5.14 | Measuring the rate of quantum phase slips **a** | Energy levels based on the two-level Hamiltonian (5.36) as a function of the flux bias ϕ . **b** | The circulating current $\langle I \rangle = -\partial E / \partial \Phi$, where $\Phi = \phi \Phi_0$ and Φ_0 is the flux quantum. **c** | The maximum supercurrent I_S through a dc SQUID as a function of the normalized enclosed flux ϕ_S . The Josephson critical current is denoted by I_c . **d** | The SQUID current I_S as a function of the flux bias ϕ in the presence of a microwave radiation of frequency f . **e** | The flux difference $\Delta\phi$ between the two peaks for various microwave frequencies f .

an ideal SQUID with negligible self inductance, the maximum supercurrent is a periodic function of the enclosed flux and follows the relation [4]

$$I_S = 2I_c |\cos \pi \phi_S|, \quad (5.41)$$

5. Stochastic Transitions between Flux States

where I_c is the critical current of the Josephson junctions, and ϕ_S is the flux enclosed by the SQUID in units of the flux quantum.

In practice, the enclosed flux ϕ_S can be higher than the flux bias ϕ depending on the degree of localization of the magnetic field that generates the flux bias. Accordingly, the supercurrent I_S increases as ϕ is swept from 0.49 to 0.51 because the overall flux enclosed by the SQUID increases. The rate of this increase, however, depends on by the flux induced by the circulating current in the qubit ring. For instance, at $\phi = 1/2$, the persistent current changes direction and results in an inflection point in the SQUID current I_S as a function of ϕ .

This measurement is conducted in the presence of a microwave radiation that induces transitions from the ground to the first excited state. These transition yield two peaks at the flux values for which the energy-level splitting resonates with the radiation frequency. The location of the two peaks depends on the frequency f (Figure 5.14c). The avoided crossing at half a flux quantum is verified by mapping the relation between the level splitting and the flux bias ϕ . In particular, the energy difference is calculated by plotting the flux difference $\Delta\phi$ between the two peaks as a function of the frequency f of the impinging photons. If the relation is linear, then the rate of quantum phase slips is negligible, and no avoided crossing occurs. If, however, the relation is nonlinear, then there is an avoided crossing at half a flux quantum, which can be deduced by extrapolating the relation to $\Delta\phi = 0$. Evidently, this measurement can be repeated as a function of the bias voltage to reproduce Figure 5.8 and to determine the fitting parameter a in the rate (5.21).

6

Conclusions

The goal of this thesis is to present a novel electronically tunable weak link for superconducting quantum circuits. In general, a weak link describes a region of weakened superconductivity interrupting two strongly superconducting electrodes. In that region, superconductivity is suppressed either intrinsically due to a geometry or material change or extrinsically due to an applied electromagnetic field. Examples of weak links include a topological insulator, a two-dimensional electron gas, a van der Waals heterostructure, a nanowire, or simply a constriction in a contiguous superconductor. The most celebrated form of a weak link, however, is the Josephson junction, a thin insulator interrupting two superconducting electrodes. Superconducting quantum bits (qubits) hinge on the nonlinear inductance of a Josephson junction. This nonlinearity yields an anharmonic energy spectrum, a prerequisite to isolate a two-level quantum system—that is, a qubit. The transition frequency of the qubit is determined by the thickness of the insulating barrier and the parameters of the superconductor. To tune this frequency, the single Josephson junction is replaced by two parallel junctions, thus forming a dc SQUID. The overall magnetic flux enclosed by the SQUID determines the transition frequency of the qubit. Unfortunately, the magnetic tunability renders the qubit sensitive to low-frequency flux noise and, hence, limits its dephasing time. This constraint motivates the need for electronically tunable weak links. In this thesis, I propose using a bias voltage to induce tunable weak links in superconductors. The results of this work establish a route towards novel superconducting quantum devices.

Throughout this thesis, the effect of a bias voltage on the density of Cooper pairs in a superconductor is studied using the numerical solution of the time-dependent Ginzburg-Landau equations, introduced in Chapter 2. The model comprises a superconductor specimen, e.g., a strip, contacted at its two ends by normal-metal electrodes that specify the value of the scalar potential. The potential difference induces a supercurrent along the direction perpendicular to the bias electrodes. More specifically, normal electrons are injected into the superconductor at one end. These electrons convert into Cooper pairs that flow to the other end. Because the reverse conversion occurs at the other electrode, the supercurrent flattens halfway between the two electrodes. Correspondingly, the minimum of the Cooper-pair density is at the center of the strip. As detailed in Chapter 3, designing the length of the strip to be a few multiples of the coherence length of the superconductor, one may obtain a global minimum of the Cooper-pair density, constituting a phase-slip center—that is, a preferential location to nucleate phase slips.

Phase slips are topological variations of the superconducting order parameter, for which the magnitude of the Cooper-pair density is locally suppressed to permit a discontinuous jump in the phase. For a closed superconducting loop, created for instance by interconnecting two curved strips, phase slips increment or decrement the phase winding number, a quantity characterizing the flux state of the loop. In an external magnetic field, a superconducting loop transitions between flux states with different winding numbers via phase slips. These transitions alter the number of flux quanta threading the loop and are triggered deterministically at specific values of the magnetic flux, which depend on the size of the ring. In the presence of a bias voltage, these deterministic phase slips occur at lower flux values and nucleate at the preferential locations induced by the bias voltage. This reduction implies that the energy barrier separating two neighboring flux states can be electronically modulated. The practicality of the electronic control of the free-energy barrier is exemplified in Chapter 4 by a superconducting memory whose state is encoded by the absence or presence of a single flux quantum within the loop. The write operation occurs via a bias-voltage pulse that temporarily lowers the energy barrier to permit a single transition to the subsequent flux state, namely logic '1'. Reapplying the same pulse enforces the reverse transition, thereby writing '0'. A shorter pulse width executes a nondestructive readout. The write

and read pulses are in the order of tens of picoseconds. The fidelity of the memory as a function of defects and variations in the control parameters is examined thoroughly in Chapter 4. The memory can operate under asymmetric flux bias and it is insensitive to defects that are much smaller than the coherence length of the superconductor. Conversely, in the presence of defects that are on the scale of the coherence length, the memory-write fidelity decreases drastically. Nevertheless, the fidelity can be recovered by calibrating the pulse width of the write operation in the presence of defects.

The electronic control of the free-energy barrier can also be used to enhance the rate of quantum phase slips. Quantum phase slips refer to stochastic transitions between neighboring flux states via tunneling through the energy barrier. According to Langer-Ambegaokar-McCumber-Halperin (hereafter LAMH) theory, the barrier height depends on the cross-sectional area of the superconductor. Consequently, quantum phase-slip circuits often incorporate an ultra-thin superconducting nanowire into a larger superconducting loop to enhance the rate of quantum phase slips. For a loop enclosing half a flux quantum, quantum phase slips coherently couple the two flux states with zero and one flux quanta, a phenomenon dubbed coherent quantum phase slips. Analogous to the Josephson effect, coherent quantum phase slips have been harnessed to build a phase-slip flux qubit. The primary drawback of this flux-qubit variant is that its transition frequency is fixed by the dimensions of the wire and the parameters of the superconductor. More important, the exponential dependence of the quantum-phase-slip rate on the dimensions of the wire entails stringent fabrication requirements. As an alternative, I propose using a superconductor of a relatively larger cross-sectional area, while compensating for the increased barrier by a bias voltage. In Chapter 5, I evaluate the barrier height as a function of the bias voltage and calculate the corresponding rates of quantum phase slips. This design can serve as a phase-slip flux qubit whose transition frequency is electronically tunable in the gigahertz range. The sensitivity of the qubit to low-frequency flux noise is discussed in Chapter 5. Since the ring is uninterrupted by an insulating oxide, the flux noise is expected to be much less than Josephson-based qubits. Moreover, the qubit is immune to fluctuations and defects occurring on a scale much smaller than the coherence length.

6.1 Outlook

This section defines several directions for future research based on the work presented in this thesis. These recommendations aim to refine the description of the devices proposed in Chapters 4 and 5, and they also highlight other applications based on the electronic control of the free-energy barrier.

First, owing to the bias voltage, normal current is injected into the interior of the superconductor, which causes Joule heating near the bias electrodes. In addition, vortex motion—for example, during the write and readout of the memory proposed in Chapter 4—results in Joule heating. Consequently, to ensure proper functionality of the memory, one must examine the heat dissipation during a complete write and readout cycle. The effect of heat can be analyzed by coupling the time-dependent Ginzburg-Landau equation with the heat diffusion equation, as detailed in Section 4.3.2. This analysis would yield practical considerations regarding the choice of the substrate and the superconductor, and it would also identify the upper limit of the operating temperature and the frequency of the write operation of the proposed memory.

Second, in this work, the free-energy barrier was estimated using the numerical solution of the time-dependent Ginzburg-Landau (GL) equations. The LAMH theory, detailed in Chapter 5, defines the barrier as the difference between the energy of the initial metastable flux state and the energy of a saddle point in the free-energy landscape, known as the saddle state. The saddle state denotes the trajectory that the superconductor traverses to transition between two metastable flux states. The time evolution of the order parameter in the GL equations, however, does not pass through this trajectory. It rather advances to the critical flux at which a deterministic transition occurs. To refine the calculation of the barrier, the exact saddle-state energy must be computed. Several numerical techniques already exist [171–173], but they must be integrated with the numerical solution of the GL equations that captures the reduction of the Cooper-pair density owing to a bias voltage.

Third, the devices discussed in Chapters 4 and 5 assumed that the voltage-biased superconducting rings are made of aluminum. Aluminum is indeed one

of the most common superconductors and is typically considered the silicon of superconducting quantum circuits. Nonetheless, a possible research question relates to the optimal choice of the superconductor—for example, for the phase-slip flux qubit introduced in Chapter 5. To that end, various materials must be explored with the aim of minimizing the sensitivity of the quantum-phase-slip rate to the bias voltage. The reduced sensitivity extends the tunability range of the qubit transition frequency and inhibits dephasing due to charge fluctuations. Coherent quantum phase slips are typically observed in strongly disordered superconductors such as amorphous InO and TiN thin films in which electrons are localized [84]. As detailed in Chapter 1, the high normal-state resistance per unit length translates to a reduced energy barrier for phase slips. This requirement, however, conflicts with the working principle of the proposed phase-slip qubit. Specifically, to properly control the rate of quantum phase slips with the bias voltage, the size of the ring must be comparable to the coherence length of the superconductor. But, the higher the disorder in the superconductor, the shorter the coherence length (e.g., the coherence length is about 20 nm for InO [84]), which renders fabricating and biasing a ring of a comparable size challenging. Accordingly, for the devices discussed in Chapters 4 and 5, one must investigate materials whose coherence length is still within the limits of accessible lithographic techniques.

Finally, as previously emphasized, the electronic control of the free-energy barrier is a promising candidate for developing novel superconducting quantum devices, two of which were presented in Chapter 4 and Chapter 5. A third unexplored example is a dc flux-bias circuit. As evidenced by the hysteresis of the free-energy spectrum of a finite-width superconducting ring, not all metastable flux states are accessible. That is why an unbiased superconducting ring cannot store an arbitrary number of flux quanta. In the presence of a bias voltage, however, the hysteresis of the energy spectrum is reduced, which gives access to all minima of the free energy. In other words, the bias voltage acts as a gate that permits the desired number of flux quanta to be enclosed within the ring. Thus, a voltage-biased superconducting ring can serve as a dc flux control for a nearby quantum circuit containing a SQUID—for example, to magnetically tune the transition frequency of a Josephson-based qubit. A similar dc flux bias is employed in adiabatic quantum computers, such as D-Wave computers, using the single-flux-quantum (SFQ) logic. Their

6. Conclusions

main disadvantage is that the initialization time scales with the number of flux quanta. For instance, to store N flux quanta, N SFQ pulses must be generated. Conversely, for a voltage-biased ring, a single bias-voltage pulse applied with an external flux can deliver the desired number of flux quanta within the ring.

An additional aspect that goes beyond the scope of the Ginzburg-Landau equations used throughout this thesis is evaluating the coherence time of the proposed qubit. In general, the tolerance of a qubit to thermal and electromagnetic noise is characterized by two time scales: the relaxation time and the dephasing time. The relaxation time denotes the time it takes an excited qubit to decay to the ground state, while the dephasing time denotes the time it takes the phase difference between two eigenstates—for example, the symmetric and antisymmetric superpositions of the two flux states of the ring—to be randomized. The purpose of such investigation would be to evaluate the coherence time of the proposed qubit and to compare it with other phase-slip qubits. The analysis would entail examining whether the use of the bias voltage introduces any decoherence channels that shorten the lifetime of the qubit. In particular, one must answer the question: Is Joule heating around the bias leads detrimental to the coherence of the qubit or is it decoupled from the dynamics of the qubit, seeing that phase slips occur away from the leads?

A

Ginzburg-Landau Equations in Dimensionless Form

This appendix derives the dimensionless form of the Ginzburg-Landau equations, used throughout the thesis. We start with the time-dependent Ginzburg-Landau (TDGL) equation

$$\frac{\hbar^2}{2m^*\mathcal{D}}\left(\frac{\partial}{\partial t} + \frac{iq}{\hbar}V\right)\psi + \frac{1}{2m^*}(-i\hbar\nabla - q\mathbf{A})^2\psi - |\alpha|\psi + \beta|\psi|^2\psi = 0, \quad (\text{A.1})$$

where \mathcal{D} is the diffusion coefficient, V is the scalar potential, and \mathbf{A} is the vector potential. The charge of a Cooper pair q equals twice the electronic charge; its mass m^* equals twice the electronic mass. Dividing by the equilibrium value of the order parameter

$$|\psi_0| = \left(\frac{|\alpha|}{\beta}\right)^{1/2}, \quad (\text{A.2})$$

leads to

$$\frac{\hbar^2}{2m^*\mathcal{D}}\left(\frac{\partial}{\partial t} + \frac{iq}{\hbar}V\right)\tilde{\psi} + \frac{1}{2m^*}(-i\hbar\nabla - q\mathbf{A})^2\tilde{\psi} - |\alpha|\tilde{\psi} + |\alpha|\tilde{\psi}^2\tilde{\psi} = 0, \quad (\text{A.3})$$

where $\tilde{\psi} = \psi/|\psi_0|$ is the normalized order parameter. Substituting with the definition (2.18) of the coherence length results in

$$\frac{\xi^2}{\mathcal{D}}\left(\frac{\partial}{\partial t} + \frac{iq}{\hbar}V\right)\tilde{\psi} + \xi^2\left(-i\nabla - \frac{q}{\hbar}\mathbf{A}\right)^2\tilde{\psi} - \tilde{\psi} + |\tilde{\psi}|^2\tilde{\psi} = 0. \quad (\text{A.4})$$

Substituting with the dimensionless quantities

$$\tilde{t} \equiv \frac{\mathcal{D}}{\xi^2} t, \quad (\text{A.5})$$

$$\tilde{\mathbf{A}} \equiv \frac{q\xi}{\hbar} \mathbf{A}, \quad (\text{A.6})$$

and

$$\tilde{V} \equiv \frac{q\xi^2}{\hbar\mathcal{D}\kappa} V, \quad (\text{A.7})$$

produces the final form

$$\left(\frac{\partial}{\partial \tilde{t}} + i\kappa \tilde{V} \right) \tilde{\psi} + \left(\frac{i}{\kappa} \tilde{\nabla} + \tilde{\mathbf{A}} \right)^2 \tilde{\psi} - \tilde{\psi} + |\tilde{\psi}|^2 \tilde{\psi} = 0, \quad (\text{A.8})$$

where the spatial coordinate is in units of the penetration depth λ . For the second TDGL equation

$$\frac{1}{\mu_0} \nabla \times \nabla \times \mathbf{A} = \frac{q|\psi|^2}{m^*} (\hbar \nabla \chi - q\mathbf{A}) - \sigma_n \left(\nabla V + \frac{\partial \mathbf{A}}{\partial t} \right), \quad (\text{A.9})$$

we can rewrite the left-hand side as

$$\text{L.H.S} = \frac{1}{\mu_0} \nabla \times \nabla \times \mathbf{A} = \frac{\hbar}{q\xi} \frac{1}{\lambda^2} \frac{1}{\mu_0} \tilde{\nabla} \times \tilde{\nabla} \times \tilde{\mathbf{A}}, \quad (\text{A.10})$$

and the right-hand side as

$$\text{R.H.S} = \frac{q\hbar}{m^*} |\psi|^2 \left(\frac{1}{\lambda} \tilde{\nabla} \chi - \frac{1}{\xi} \tilde{\mathbf{A}} \right) - \sigma_n \left(\frac{1}{\lambda} \frac{\hbar\mathcal{D}\kappa}{q\xi^2} \tilde{\nabla} \tilde{V} + \frac{\hbar}{q\xi} \frac{\mathcal{D}}{\xi^2} \frac{\partial \tilde{\mathbf{A}}}{\partial \tilde{t}} \right). \quad (\text{A.11})$$

Multiplying both sides by $q\xi/\hbar$ leads to

$$\frac{1}{\lambda^2} \frac{1}{\mu_0} \tilde{\nabla} \times \tilde{\nabla} \times \tilde{\mathbf{A}} = \frac{q^2 |\tilde{\psi}|^2 |\alpha|}{m^* \beta} \left(\frac{1}{\kappa} \tilde{\nabla} \chi - \tilde{\mathbf{A}} \right) - \frac{\sigma_n \mathcal{D}}{\xi^2} \left(\tilde{\nabla} \tilde{V} + \frac{\partial \tilde{\mathbf{A}}}{\partial \tilde{t}} \right). \quad (\text{A.12})$$

Substituting with the definition (2.22) of the penetration depth λ results in

$$\frac{1}{\lambda^2} \tilde{\nabla} \times \tilde{\nabla} \times \tilde{\mathbf{A}} = \frac{1}{\lambda^2} \left(\frac{1}{\kappa} \tilde{\nabla} \chi - \tilde{\mathbf{A}} \right) |\tilde{\psi}|^2 - \frac{\mu_0 \sigma_n \mathcal{D}}{\xi^2} \left(\tilde{\nabla} \tilde{V} + \frac{\partial \tilde{\mathbf{A}}}{\partial \tilde{t}} \right). \quad (\text{A.13})$$

Finally, multiplying both sides by λ^2 leads to the final form

$$\tilde{\nabla} \times \tilde{\nabla} \times \tilde{\mathbf{A}} = \left(\frac{1}{\kappa} \tilde{\nabla} \chi - \tilde{\mathbf{A}} \right) |\tilde{\psi}|^2 - \tilde{\sigma} \left(\tilde{\nabla} \tilde{V} + \frac{\partial \tilde{\mathbf{A}}}{\partial \tilde{t}} \right), \quad (\text{A.14})$$

where the normalized conductivity $\tilde{\sigma}$ equals $\mu_0 \mathcal{D} \kappa^2 \sigma_n$.

B

London Equation for a Superconducting Ring

The central constituent of the model considered throughout this thesis is a superconducting ring. For a ring of finite width, the magnetic field can be either localized within the ring or uniform throughout the space. This appendix compares these two field profiles by solving the London equation for the vector potential \mathbf{A} and, in turn, the magnetic field \mathbf{B} .

Our starting point is the supercurrent density expression (2.15). In the London limit, i.e., assuming a constant magnitude of the complex order parameter, the supercurrent density \mathbf{J}_s reduces to

$$\mu_0 \mathbf{J}_s = \frac{1}{\lambda^2} \left(\frac{\hbar}{q} \nabla \chi - \mathbf{A} \right), \quad (\text{B.1})$$

where λ is the penetration depth and χ is the phase of the complex order parameter $\psi = |\psi| \exp(i\chi)$. Using Ampere's law and the definition of the vector potential $\nabla \times \mathbf{A} = \mathbf{B}$, we arrive at

$$\nabla \times \nabla \times \mathbf{A} = \frac{1}{\lambda^2} \left(\frac{\hbar}{q} \nabla \chi - \mathbf{A} \right). \quad (\text{B.2})$$

For the vector potential in equation (B.2) to have an analytical solution, I assume the ring is infinitely long in the z direction so that any circulating current induces a magnetic field parallel to the z axis. This assumption leads to translational symmetry in the z direction—that is, the model reduces to a

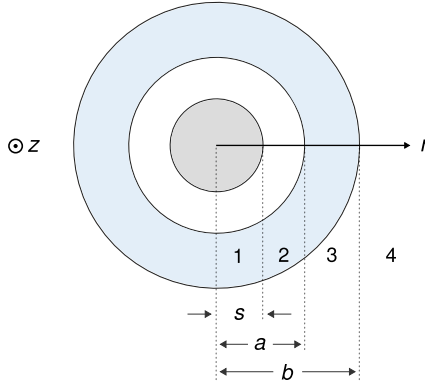


Figure B.1 | Schematic of a superconducting ring pierced by an ideal solenoid. The superconducting ring is of inner radius a and outer radius b . The radius of the solenoid is denoted by s . The numbers (1-4) correspond to the four regions along the radial direction where the Laplacian of the vector potential (B.5) is solved.

two-dimensional problem along r and θ . Moreover, if the applied magnetic field is cylindrically symmetric, then the phase χ only depends on θ and takes the form $\chi = n\theta$, where n is the phase winding number, or the flux state of the ring. Under these assumptions and using the identity [187]

$$\nabla \times \nabla \times \mathbf{A} = \nabla(\nabla \cdot \mathbf{A}) - \nabla^2 \mathbf{A}, \quad (\text{B.3})$$

the Laplacian of the vector potential in the Coulomb gauge takes the form

$$\nabla^2 \mathbf{A} = \frac{1}{\lambda^2} \left(\mathbf{A} - \frac{\hbar n}{qr} \hat{\theta} \right). \quad (\text{B.4})$$

Adopting the dimensionless notation detailed in Appendix A, I can write the Laplacian of the vector potential as

$$\nabla^2 \mathbf{A} = \mathbf{A} - \frac{n}{\kappa r} \hat{\theta}, \quad (\text{B.5})$$

where \mathbf{A} is in units of $\hbar/(q\xi)$, and the radial coordinate r is in units of the penetration depth λ .

I examine two distinct profiles of the applied magnetic field: localized and uniform. In both cases, the magnetic field is cylindrically symmetric, and the

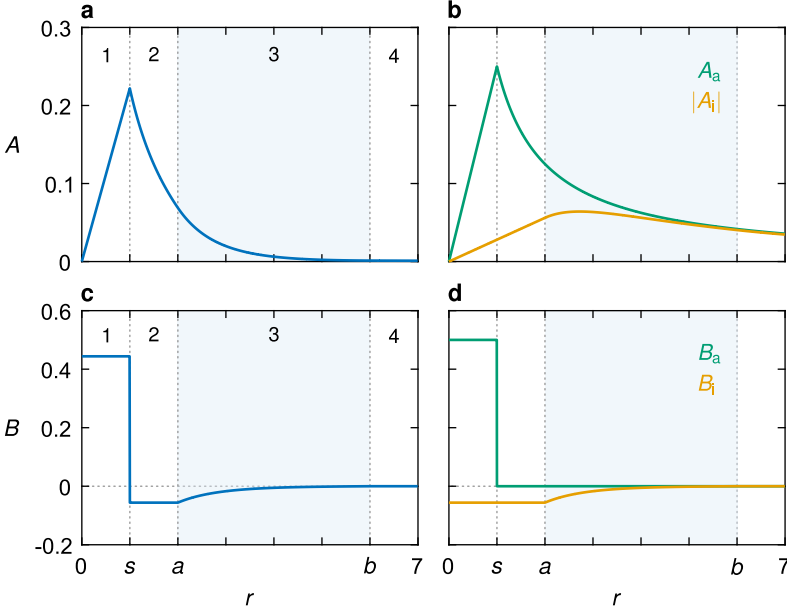


Figure B.2 | Magnetic field in a superconducting ring pierced by an ideal solenoid. The ring is of inner radius a and outer radius b , and the solenoid is of radius s . The applied magnetic flux equals $\phi_a = 1/4$. **a** | The azimuthal component of the total vector potential A as a function of the radial distance r . **b** | The applied vector potential A_a and the absolute value of the induced vector potential A_i as a function of r . **c, d** | The total B , the applied B_a , and the induced B_i magnetic fields as a function of r . The vector potential and the magnetic field are computed by solving the six equations (B.14) for a flux state $n = 0$. Variables are normalized according to Appendix A.

vector potential can be written as

$$\mathbf{A} = A(r) \hat{\theta}. \quad (\text{B.6})$$

First, for the localized magnetic field, I consider an Aharonov-Bohm-like setup where the ring is pierced by an ideal solenoid, to which the applied field is confined [188]. The applied field takes the form

$$\mathbf{B}_a = B_0 U(r-s) \hat{z}, \quad (\text{B.7})$$

where $U(r-s)$ is a unit-step function, and s is the radius of the solenoid. The space is divided into four regions (Figure B.1). Outside the ring—that is

B. London Equation for a Superconducting Ring

region 1, 2, and 4—there is no supercurrent, and the Laplacian of the vector potential (B.5) reduces to $\nabla^2 \mathbf{A} = 0$ with the general solution

$$A = c_1 r + \frac{c_2}{r}. \quad (\text{B.8})$$

Inside the ring (region 3), however, the Laplacian (B.5) takes the form

$$rA' + r^2 A'' - (1 + r^2)A = -\frac{nr}{\kappa}, \quad (\text{B.9})$$

where $A' \equiv dA/dr$, giving rise to a second-order inhomogeneous differential equation. Using the method of undetermined coefficients [189], the general solution is expressed as

$$A = y(r) + p(r), \quad (\text{B.10})$$

where the complementary solution $y(r)$ satisfies the homogeneous equation, and the particular solution $p(r)$ satisfies the inhomogeneous equation. The homogeneous part

$$rA' + r^2 A'' - (1 + r^2)A = 0, \quad (\text{B.11})$$

is known as the modified Bessel equation [190] and has the general solution

$$y(r) = c_1 I_1(r) + c_2 K_1(r), \quad (\text{B.12})$$

where I_1 and K_1 are the modified Bessel functions of the first and second kind, respectively. The general solution to the inhomogeneous equation reads

$$A(r) = c_1 I_1(r) + c_2 K_1(r) + \frac{n}{\kappa r}. \quad (\text{B.13})$$

This solution must satisfy the continuity of the vector potential and the magnetic field at all interfaces, except at the surface of the solenoid where the magnetic field is discontinuous by the solenoid field B_0 . These boundary conditions lead to six equations with six unknowns¹. In matrix form and for a ring of inner radius a and outer radius b , these equations are expressed as

$$\begin{pmatrix} s & -s & -s^{-1} & 0 & 0 & 0 \\ 2 & -2 & 0 & 0 & 0 & 0 \\ 0 & a & a^{-1} & -I_1(a) & -K_1(a) & 0 \\ 0 & -2 & 0 & \Sigma_I(a) & \Sigma_K(a) & 0 \\ 0 & 0 & 0 & -I_1(b) & -K_1(b) & b^{-1} \\ 0 & 0 & 0 & \Sigma_I(b) & \Sigma_K(b) & 0 \end{pmatrix} \begin{pmatrix} c_1 \\ c_2 \\ c_3 \\ c_4 \\ c_5 \\ c_6 \end{pmatrix} = \begin{pmatrix} 0 \\ B_0 \\ n/(\kappa a) \\ 0 \\ n/(\kappa b) \\ 0 \end{pmatrix}, \quad (\text{B.14})$$

¹The coefficient of $1/r$ in region 1 is zero so that the solution does not blow up at $r = 0$. Likewise, the coefficient of r in region 4 is zero so that the solution does not blow up at $r \rightarrow \infty$.

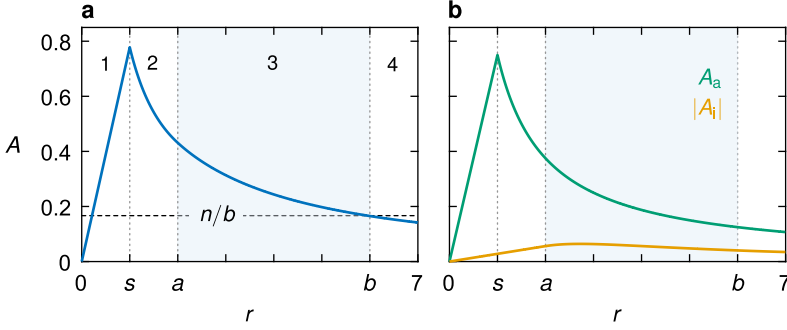


Figure B.3 | Vector potential A in a superconducting ring threaded by an ideal solenoid. The ring is of inner radius a and outer radius b , and the solenoid is of radius s . The applied magnetic flux equals $\phi_a = 3/4$. **a** | The azimuthal component of the total vector potential A as a function of the radial distance r . **b** | The applied A_a and the induced A_i vector potentials as a function of r . The vector potential is in units of $\hbar/(q\xi)$ and is computed by solving the six equations (B.14) for a flux state $n = 1$.

with

$$\Sigma_I(r) = \frac{I_1(r)}{r} + \frac{I_0(r)}{2} + \frac{I_2(r)}{2}, \quad (\text{B.15})$$

and

$$\Sigma_K(r) = \frac{K_1(r)}{r} - \frac{K_0(r)}{2} - \frac{K_2(r)}{2}. \quad (\text{B.16})$$

For a given flux state, specified by the phase winding number n , the six equations (B.14) are solved simultaneously for the induced vector potential. For instance, for a winding number $n = 0$ and an applied flux $\phi_a = 1/4$ through the solenoid, a counterclockwise supercurrent induces a magnetic field in the negative z direction (Figure B.2). The induced field opposes the applied one so that the total flux enclosed within the ring is quantized and is equal to zero. Conversely, for $n = 1$ and an applied flux $\phi_a = 3/4$, a clockwise supercurrent induces a magnetic field in the positive z direction (Figure B.3). The induced magnetic field augments the applied one so that the total flux enclosed within the ring equals one flux quantum, as evidenced by the value of the total vector potential at the outer rim of the ring [$A(b) = n/b$]. In both cases, the supercurrent circulates along the inner rim of the ring.

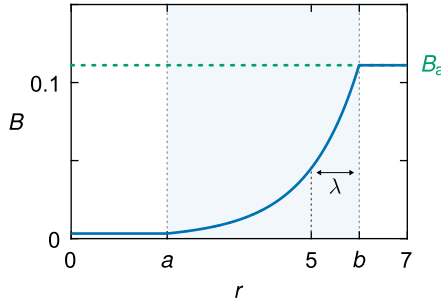


Figure B.4 | A superconducting ring placed in a uniform perpendicular magnetic field. The ring is of inner radius a . The magnetic field decays exponentially from the outer rim of the ring according to the penetration depth λ . The applied magnetic field corresponds to two flux quanta enclosed by the outer rim of the ring. Variables are written in a dimensionless form according to Appendix A.

Second, for the uniform magnetic field

$$\mathbf{B}_a = B_0 \hat{z}, \quad (\text{B.17})$$

the radial space is divided into three regions. In analogy to the solenoid setup, I solve the Laplacian $\nabla^2 \mathbf{A} = 0$ outside the ring, and the modified Bessel equation inside the ring. The external magnetic field decays exponentially from the surface of the ring according to the penetration depth λ (Figure B.4).

The key difference between the localized and the uniform field setups is the distribution of the supercurrent density. In the solenoid setup, there is no magnetic field directly impinging on the ring. Therefore, the Meissner effect is irrelevant and the magnetic field acts on the superconducting condensate only through its vector potential. Consequently, any induced supercurrent is solely due to the flux quantization requirement in superconducting loops. Put differently, the supercurrent circulates along the inner rim of the ring to ensure the enclosed flux is an integer multiple of the flux quantum. In contrast, for a magnetic field that is uniform throughout space, the superconductor must expel the magnetic field (Meissner effect). As a result, the supercurrent circulates at the outer rim of the ring so that the applied field decays exponentially inside the bulk of the ring.

C

Numerical Solution of the Ginzburg-Landau Equations

This appendix presents the numerical solution of the time-dependent GL equations, used extensively in Chapters 2, 3, 4, and 5. First, I introduce the finite-difference method for computing the spatial derivatives. Second, I discuss the two common gauge choices: the Coulomb gauge (Section C.2) and the zero-scalar-potential gauge (Section C.3).

C.1 Finite-difference method

As discussed in Chapter 2, for a superconducting ring whose thickness is much smaller than the coherence length, the order parameter varies negligibly along the thickness of the ring. As a consequence, the model of the ring reduces to a two-dimensional superconductor.

For a ring of radius R and width w , I use a discrete polar grid (Figure C.1). Along the radial direction, the grid is characterized by $\{r_k\}$ with a spacing Δ_r and the integer $k \in [1, K]$. If the grid covers only the bulk of the ring, then $k = 1$ corresponds to $r = R$ and $k = K$ to $r = R + w$. Along the azimuthal direction, the grid is characterized by $\{\theta_p\}$ with a spacing Δ_θ and the integer $p \in [1, P]$. The integer $p = 1$ corresponds to $\theta = 0$ and $p = P$ to $\theta = 2\pi - \Delta_\theta$.

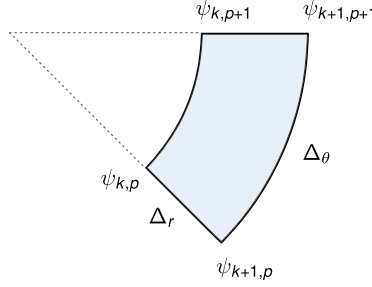


Figure C.1 | Numerical grid in polar coordinates. Along the radial direction, the grid is characterized by $\{r_k\}$ with a spacing Δ_r . Along the azimuthal direction, the grid is characterized by $\{\theta_p\}$ with a spacing Δ_θ .

To compute the spatial derivatives in the TDGL equations (2.54) and (2.55), I use the central-difference method with a five-point stencil [191]. For instance, in polar coordinates, the Laplacian is expressed as

$$\nabla^2 \equiv \frac{\partial^2}{\partial r^2} + \frac{1}{r} \frac{\partial}{\partial r} + \frac{1}{r^2} \frac{\partial^2}{\partial \phi^2}. \quad (\text{C.1})$$

On the discrete grid (Figure C.1), it takes the form

$$\begin{aligned} \nabla^2 \psi_{k,p} = & \frac{1}{\Delta_r^2} (\psi_{k+1,p} - 2\psi_{k,p} + \psi_{k-1,p}) \\ & + \frac{1}{2r_k \Delta_r} (\psi_{k+1,p} - \psi_{k-1,p}) \\ & + \frac{1}{r_k^2 \Delta_\theta^2} (\psi_{k,p+1} - 2\psi_{k,p} + \psi_{k,p-1}), \end{aligned} \quad (\text{C.2})$$

where the radial distance r_k is defined as $r_k = R + (k - 1)\Delta_r$.

To impose a Neumann boundary condition at the edges of the ring, the first derivative of the order parameter must be set to zero. In the discretized form, at the outer boundary of the ring, the Neumann condition translates to

$$\frac{1}{2\Delta_r} (\psi_{k+1,p} - \psi_{k-1,p}) \Big|_{k=K} = 0, \quad (\text{C.3})$$

where $k = K$ corresponds to $r = R + w$. The condition (C.3) specifies the value of the order parameter at the fictitious point $k = K + 1$ outside the grid as follows

$$\psi_{K+1,p} = \psi_{K-1,p}. \quad (\text{C.4})$$

Substituting with equation (C.4) in the second derivative at the outer boundary of the ring leads to

$$\left. \frac{\partial^2 \psi}{\partial r^2} \right|_{r=R+w} = \frac{2}{\Delta_r^2} (\psi_{K-1,p} - \psi_{K,p}). \quad (\text{C.5})$$

The same conditions are also imposed at the inner boundary of the ring.

C.2 GL equations in the Coulomb gauge

In the Coulomb gauge $\nabla \cdot \mathbf{A} = 0$, I solve the time-dependent GL equation

$$\frac{\partial \psi}{\partial t} = -i\kappa V \psi - \left(\frac{i}{\kappa} \nabla + \mathbf{A} \right)^2 \psi + (1 - |\psi|^2) \psi, \quad (\text{C.6})$$

with the continuity equation

$$\sigma \nabla^2 V = \nabla \cdot \mathbf{J}_s = \nabla \cdot \left[\frac{1}{2i\kappa} (\psi^* \nabla \psi - \psi \nabla \psi^*) - |\psi|^2 \mathbf{A} \right], \quad (\text{C.7})$$

self-consistently for the order parameter $\psi(\mathbf{r}, t)$ and the scalar potential $V(\mathbf{r}, t)$.

As an illustrative example, and in line with Section 2.3.1, I assume the width of the ring is much smaller than the characteristic length scales (i.e., $w \ll \xi$). Consequently, the order parameter does not vary along the radial direction, and all the vector quantities only have an azimuthal component. In this limit, the two TDGL equations (C.6) and (C.7) reduce to

$$\frac{\partial \psi}{\partial t} = -i\kappa V \psi - \left(\frac{i}{\kappa R} \frac{\partial}{\partial \theta} + A \right)^2 \psi + (1 - |\psi|^2) \psi, \quad (\text{C.8})$$

and

$$\frac{\sigma}{R^2} \frac{\partial^2 V}{\partial \theta^2} = \frac{1}{R} \frac{\partial J_s}{\partial \theta}. \quad (\text{C.9})$$

First, I solve the Laplacian (C.7) as a system of linear equations

$$\frac{\sigma}{R^2 \Delta_\theta^2} (V_{p+1} - 2V_p + V_{p-1}) = \frac{1}{2R \Delta_\theta} (J_s^{p+1} - J_s^{p-1}). \quad (\text{C.10})$$

To bias the superconducting ring, as in Chapter 3, the potential V is specified by the bias electrodes along the outer perimeter of the ring. For instance, in the example discussed in Section 3.2.1, the bias voltage specifies the electrostatic potential to $V(\theta = 0) = 0$ and $V(\theta = \pi) = V_b$. In the discrete form, this condition translates to $V_{p=1} = 0$ and $V_{p=P/2+1} = V_b$.

Second, for the time-evolution equation, I use the fourth-order Runge-Kutta method. To that end, I rewrite the first TDGL equation (C.8) in the form

$$\frac{\partial \psi}{\partial t} = \mathcal{F}(\psi, A, V) = -i\kappa V \psi - \left(\frac{i}{\kappa R} \frac{\partial}{\partial \theta} + A \right)^2 \psi + (1 - |\psi|^2) \psi. \quad (\text{C.11})$$

For a time grid defined by $\{n\}$ with a spacing Δ_t , the time stepping proceeds according to the relation

$$\psi^{n+1} = \psi^n + \frac{\Delta_t}{6}(f_1 + 2f_2 + 2f_3 + f_4). \quad (\text{C.12})$$

with

$$\begin{aligned} f_1 &= \mathcal{F}(\psi^n, V^n, \mathbf{A}^n), \\ f_2 &= \mathcal{F}(\psi^n + \Delta_t f_1/2, V^{n+1/2}, A^{n+1/2}), \\ f_3 &= \mathcal{F}(\psi^n + \Delta_t f_2/2, V^{n+1/2}, A^{n+1/2}), \\ f_4 &= \mathcal{F}(\psi^n + \Delta_t f_3, V^{n+1}, A^{n+1}). \end{aligned} \quad (\text{C.13})$$

The overall algorithm of the solution is summed up in the pseudo code

```

% initial condition
 $\psi(t = 0, \theta) = 1$ 
% time stepper
loop
   $f_1 = \mathcal{F}(\psi^n, A^n, V^n)$ 
   $V_2 \leftarrow$  solve Eq. (C.10) with  $\psi^n + \Delta_t f_1/2, A^{n+1/2}, V_b^{n+1/2}$ 
   $f_2 = \mathcal{F}(\psi^n + \Delta_t f_1/2, A^{n+1/2}, V_2)$ 
   $V_3 \leftarrow$  solve Eq. (C.10) with  $\psi^n + \Delta_t f_2/2, A^{n+1/2}, V_b^{n+1/2}$ 
   $f_3 = \mathcal{F}(\psi^n + \Delta_t f_2/2, A^{n+1/2}, V_3)$ 
   $V_4 \leftarrow$  solve Eq. (C.10) with  $\psi^n + \Delta_t f_3, A^{n+1}, V_b^{n+1}$ 
   $f_4 = \mathcal{F}(\psi^n + \Delta_t f_3, A^{n+1}, V_4)$ 
   $\psi^{n+1} = \psi^n + (\Delta_t/6)(f_1 + 2f_2 + 2f_3 + f_4)$ 
   $V^{n+1} \leftarrow$  solve Eq. (C.10) with  $\psi^{n+1}, A^{n+1}, V_b^{n+1}$ 
end loop

```

C.3 GL equations in a zero-scalar-potential gauge

In the zero-scalar-potential gauge $V = 0$, I solve the two equations

$$\frac{\partial \psi}{\partial t} = -\left(\frac{i}{\kappa} \nabla + \mathbf{A}\right)^2 \psi + (1 - |\psi|^2) \psi, \quad (\text{C.14})$$

and

$$\sigma \frac{\partial \mathbf{A}}{\partial t} = \frac{1}{2i\kappa} (\psi^* \nabla \psi - \psi \nabla \psi^*) - |\psi|^2 \mathbf{A} - \nabla \times \nabla \times \mathbf{A}, \quad (\text{C.15})$$

self-consistently for the complex order parameter $\psi(\mathbf{r}, t)$ and the vector potential $\mathbf{A}(\mathbf{r}, t)$. Similar to Section C.2, I define a discrete time grid indexed by $\{n\}$ with a spacing Δ_t . Next, I cast the two TDGL equations as

$$\frac{\partial \psi}{\partial t} = \mathcal{F}(\psi, A), \quad (\text{C.16})$$

and

$$\frac{\partial A}{\partial t} = \mathcal{G}(\psi, A). \quad (\text{C.17})$$

The time stepping of these two simultaneous equations proceeds according to

$$\psi^{n+1} = \psi^n + \frac{\Delta_t}{6} (f_1 + 2f_2 + 2f_3 + f_4), \quad (\text{C.18})$$

and

$$A^{n+1} = A^n + \frac{\Delta_t}{6} (g_1 + 2g_2 + 2g_3 + g_4), \quad (\text{C.19})$$

where the coefficients are evaluated, in that order, by

$$\begin{aligned} f_1 &= \mathcal{F}(\psi^n, A^n), \\ g_1 &= \mathcal{G}(\psi^n, A^n), \\ f_2 &= \mathcal{F}(\psi^n + (\Delta_t/2)k_1, A^n + (\Delta_t/2)g_1), \\ g_2 &= \mathcal{G}(\psi^n + (\Delta_t/2)k_1, A^n + (\Delta_t/2)g_1), \\ f_3 &= \mathcal{F}(\psi^n + (\Delta_t/2)k_2, A^n + (\Delta_t/2)g_2), \\ g_3 &= \mathcal{G}(\psi^n + (\Delta_t/2)k_2, A^n + (\Delta_t/2)g_2), \\ f_4 &= \mathcal{F}(\psi^n + \Delta_t k_3, A^n + \Delta_t g_3), \\ g_4 &= \mathcal{G}(\psi^n + \Delta_t k_3, A^n + \Delta_t g_3). \end{aligned} \quad (\text{C.20})$$

C.3.1 Example of a ring pierced by an ideal solenoid

This section presents an example of the solution of the TDGL using the gauge $V = 0$. I assume translational symmetry along the z direction such that currents circulating in the ring induce a magnetic field parallel to the z axis. For the applied field, I consider an Aharonov-Bohm-like setup where the superconducting ring is pierced by an ideal solenoid to which the field is confined [188]. The applied field, then, takes the form

$$\mathbf{B}_a = B_0 U(r-s) \hat{z}, \quad (\text{C.21})$$

where $U(r-s)$ is a unit-step function, and s is the radius of the solenoid. Due to the cylindrical symmetry of the ring and of the applied field, the vector potential only has an azimuthal component. In the scalar form, the second TDGL equation (C.15) reduces to

$$\sigma \frac{\partial A}{\partial t} = \frac{1}{2i\kappa r} \left(\psi^* \frac{\partial \psi}{\partial \theta} - \psi \frac{\partial \psi^*}{\partial \theta} \right) - |\psi|^2 A + \frac{1}{r} \frac{\partial A}{\partial r} + \frac{\partial^2 A}{\partial r^2} - \frac{A}{r^2}. \quad (\text{C.22})$$

In this example, I account for the self-inductance of the ring. Thus, the vector potential is divided into two components: applied and induced ($\mathbf{A} = \mathbf{A}_a + \mathbf{A}_i$). Therefore, the time evolution of the induced vector potential reads

$$\sigma \frac{\partial A_i}{\partial t} = -\frac{\partial A_a}{\partial t} + \frac{1}{2i\kappa r} \left(\psi^* \frac{\partial \psi}{\partial \theta} - \psi \frac{\partial \psi^*}{\partial \theta} \right) - |\psi|^2 A + \frac{1}{r} \frac{\partial A_i}{\partial r} + \frac{\partial^2 A_i}{\partial r^2} - \frac{A_i}{r^2}, \quad (\text{C.23})$$

where $\nabla \times \mathbf{A}_a = 0$ inside the ring as the applied field is confined to the solenoid.

The time-evolution equation (C.23) is only defined inside the ring—that is, where a supercurrent flows. Outside the ring, however, I solve Ampere's law in free space ($\nabla \times \nabla \times \mathbf{A} = 0$) to impose proper boundary conditions on the vector potential. The general solution outside the ring is

$$A(r) = c_1 r + \frac{c_2}{r}. \quad (\text{C.24})$$

In the region $0 \leq r \leq R$, the vector potential must vanish at $r = 0$, and the solution reduces to $c_1 r$. Similarly, in the region $R + w \leq r \leq \infty$, the solution reduces to c_2/r . Invoking the discrete grid $\{r_k\}$, at $r = R$, I can write

$$A_1^{k-1} = c_1 (R - \Delta_r) = \frac{R - \Delta_r}{R} A_1^k. \quad (\text{C.25})$$

Likewise, at $r = R + w$, I can write

$$A_i^{k+1} = \frac{c_2}{R + w + \Delta_r} = \frac{R + w}{R + w + \Delta_r} A_i^k. \quad (\text{C.26})$$

The two conditions (C.25) and (C.26) modify the finite-difference derivatives at the ring boundaries. Accordingly, at $r = R$, the first derivative becomes

$$\begin{aligned} \left. \frac{\partial A_i}{\partial r} \right|_{r=R} &= \frac{1}{2\Delta_r} (A_i^{k+1} - A_i^{k-1}) \\ &= \frac{1}{2\Delta_r} \left[A_i^{k+1} - \left(\frac{R - \Delta_r}{R} \right) A_i^k \right]. \end{aligned} \quad (\text{C.27})$$

And, at $r = R + w$, it becomes

$$\begin{aligned} \left. \frac{\partial A_i}{\partial r} \right|_{r=R+w} &= \frac{1}{2\Delta_r} (A_i^{k+1} - A_i^{k-1}) \\ &= \frac{1}{2\Delta_r} \left[\left(\frac{R + w}{R + w + \Delta_r} \right) A_i^k - A_i^{k-1} \right]. \end{aligned} \quad (\text{C.28})$$

The second derivatives are computed at the sample boundaries in a similar manner. Using these boundary conditions, it is sufficient to solve the time-evolution equation (C.23) within the ring to obtain the correct radial dependence of the induced vector potential.

As an example, I consider a ring of radius $R = \xi$ and width $w = 4\xi$. The solenoid field is increased up to a steady-state value that corresponds to four flux quanta. To ensure that the enclosed magnetic flux is quantized, a supercurrent flows along the inner boundary of the ring (Figure C.2). Because the ring starts with a phase winding number $n = 0$, it must screen all the external flux so that the overall enclosed flux equals zero.

In the absence of fluctuations that break the cylindrical symmetry of the ring, the first TDGL equation (C.14) always results in an order parameter that is cylindrically symmetric since the applied vector potential does not vary along the azimuthal direction. In turn, the time evolution of the induced vector potential (C.23) also maintains the symmetry. Consequently, a phase slip for which the order parameter is suppressed locally never occurs—that is, transitions between flux states are forbidden. The steady state in the absence of fluctuations corresponds to a phase winding number $n = 0$ (Figure C.2a).

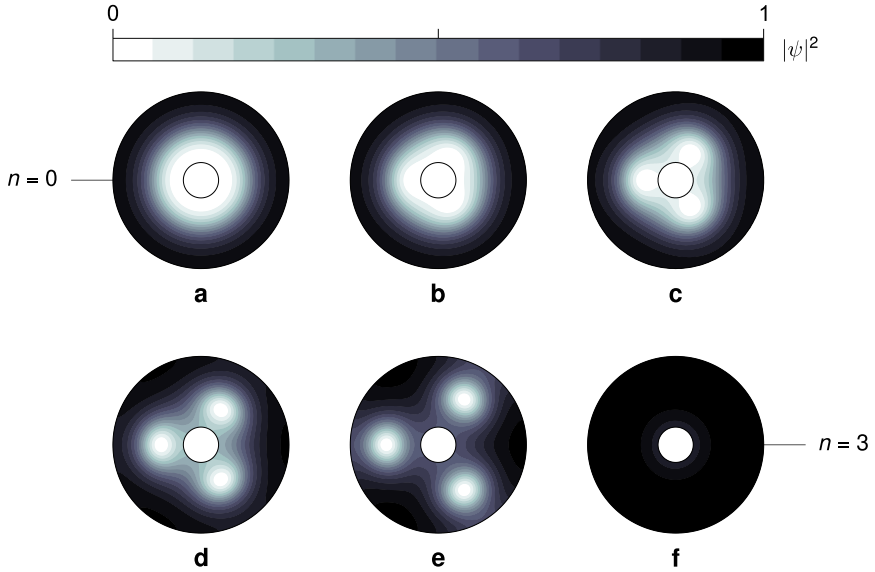


Figure C.2 | Time evolution of Cooper-pair density in a superconducting ring. The letters (a-f) denote the sequential evolution of the Cooper-pair density, normalized by its equilibrium value $|\psi_0|$, as the ring transitions from a flux state $n = 0$ to $n = 3$, in response to four flux quanta applied through an ideal solenoid piercing the ring (Figure B.1). Parameters used: $R = 1$, $w = 4$, $\kappa = 1$, and $\sigma = 1$.

In contrast, in the presence of fluctuations, phase slips can nucleate, and the ring lowers its energy by transitioning to adjacent flux states. Numerically, fluctuations are included by adding a noise term to the right-hand side of the TDGL equation (C.14) in the order of 10^{-5} [118]. The steady state in the presence of fluctuations corresponds to a winding number $n = 3$ (Figure C.2f).

D

Derivation of the Eckhaus Instability

In a uniform magnetic field, the solution to the time-independent Ginzburg-Landau (GL) equation for a one-dimensional superconducting ring takes the plane-wave form

$$\psi_n = \left[1 - \frac{1}{\kappa^2 R^2} (n - \phi)^2 \right]^{1/2} e^{in\theta}, \quad (\text{D.1})$$

where ϕ is the normalized flux, and θ is the azimuthal angle. The phase winding number n represents the flux state of the ring. As the magnetic field increases, the ring transitions between these metastable flux states via deterministic or stochastic phase slips. This appendix defines the condition for a deterministic transition, known as the Eckhaus instability [132–134].

In the presence of small fluctuations δ , we can write the complex order parameter around a metastable state ψ_n up to first order in δ as

$$\psi = \psi_n + \delta(\theta, t). \quad (\text{D.2})$$

Substituting with the expansion (D.2) into the first TDGL equation

$$\frac{\partial \psi}{\partial t} = -\frac{1}{\kappa^2 R^2} \left(i \frac{\partial}{\partial \theta} + \phi \right)^2 \psi + (1 - |\psi|^2) \psi, \quad (\text{D.3})$$

D. Derivation of the Eckhaus Instability

leads to

$$\begin{aligned} \frac{\partial \psi_n}{\partial t} + \frac{\partial \delta}{\partial t} = \frac{1}{\kappa^2 R^2} \left[\frac{\partial^2 \psi_n}{\partial \theta^2} + \frac{\partial^2 \delta}{\partial \theta^2} - 2i\phi \left(\frac{\partial \psi_n}{\partial \theta} + \frac{\partial \delta}{\partial \theta} \right) - \phi^2 (\psi_n + \delta) \right] \\ + (\psi_n + \delta) - |(\psi_n^* + \delta^*)(\psi_n + \delta)|^2 (\psi_n + \delta). \end{aligned} \quad (\text{D.4})$$

Because the state ψ_n is stationary—that is, it satisfies the time-independent GL equation—the expression simplifies to

$$\frac{\partial \delta}{\partial t} = \frac{1}{\kappa^2 R^2} \left(\frac{\partial^2 \delta}{\partial \theta^2} - 2i\phi \frac{\partial \delta}{\partial \theta} - \phi^2 \delta \right) + \delta - 2|\psi_n|^2 \delta - \psi_n^2 \delta^*, \quad (\text{D.5})$$

where the nonlinear terms in δ are dropped. Following the standard recipe of the linear stability analysis, fluctuations can be written in the form

$$\delta(\theta, t) = a(\theta) e^{\epsilon t}, \quad (\text{D.6})$$

Because of the periodicity of the ring, we can expand the amplitude a as a Fourier series

$$a(\theta) = \sum_p c_p e^{i(n+p)\theta}, \quad (\text{D.7})$$

and δ takes the form

$$\delta(\theta, t) = e^{\epsilon t} \sum_{p \geq 0} (c_p e^{i(n+p)\theta} + c_{-p} e^{i(n-p)\theta}). \quad (\text{D.8})$$

Substituting with the series expansion of δ into the time evolution (D.5) gives

$$\begin{aligned} \epsilon (c_p e^{i(n+p)\theta} + c_{-p} e^{i(n-p)\theta}) = c_p e^{i(n+p)\theta} + c_{-p} e^{i(n-p)\theta} \\ - (2 - 2v_s^2) (c_p e^{i(n+p)\theta} + c_{-p} e^{i(n-p)\theta}) \\ - (1 - v_s^2) (c_p e^{i(n-p)\theta} + c_{-p} e^{i(n+p)\theta}) \\ - \left(v_s + \frac{p}{\kappa R} \right)^2 c_p e^{i(n+p)\theta} - \left(v_s - \frac{p}{\kappa R} \right)^2 c_{-p} e^{i(n-p)\theta}, \end{aligned} \quad (\text{D.9})$$

where the superfluid velocity is defined as

$$v_s \equiv \frac{1}{\kappa R} (n - \phi). \quad (\text{D.10})$$

In matrix form, equation (D.9) reads

$$\epsilon \begin{pmatrix} c_p \\ c_{-p} \end{pmatrix} = \begin{pmatrix} B_{11} & B_{12} \\ B_{21} & B_{22} \end{pmatrix} \begin{pmatrix} c_p \\ c_{-p} \end{pmatrix}, \quad (\text{D.11})$$

where

$$B_{11} = 1 - \frac{(\kappa R v_s + p)^2}{\kappa^2 R^2} - 2(1 - v_s^2), \quad (\text{D.12})$$

$$B_{12} = -(1 - v_s^2), \quad (\text{D.13})$$

$$B_{21} = -(1 - v_s^2), \quad (\text{D.14})$$

and

$$B_{22} = 1 - \frac{(\kappa R v_s - p)^2}{\kappa^2 R^2} - 2(1 - v_s^2). \quad (\text{D.15})$$

Solving the determinant

$$\begin{vmatrix} B_{11} - \epsilon & B_{12} \\ B_{21} & B_{22} - \epsilon \end{vmatrix} = 0, \quad (\text{D.16})$$

results in the eigenvalues

$$\epsilon_{\pm p} = -1 - \frac{p^2}{\kappa^2 R^2} + v_s^2 \pm \sqrt{(1 - v_s^2)^2 + \frac{4v_s^2 p^2}{\kappa^2 R^2}}, \quad (\text{D.17})$$

where the eigenvalues ϵ_{-p} are negative definite and can be dropped. The index p refers to the periodicity of fluctuations. For instance, an index $p = 1$ refers to fluctuations that repeat once—that is, fluctuations that wind up the phase once, namely single phase-slip events. Similarly, an index $p = 2$ refers to double phase-slip events, and so on. Accordingly, the critical point for a single phase slip is governed by the eigenvalue

$$\epsilon_1 = -1 - \frac{1}{\kappa^2 R^2} + v_s^2 + \sqrt{(1 - v_s^2)^2 + \frac{4v_s^2}{\kappa^2 R^2}}. \quad (\text{D.18})$$

Because fluctuations are only allowed to grow for a positive eigenvalue, the critical point corresponds to an eigenvalue

$$\epsilon_1 = 0 = -1 - \frac{1}{\kappa^2 R^2} + v_s^2 + \sqrt{(1 - v_s^2)^2 + \frac{4v_s^2}{\kappa^2 R^2}}, \quad (\text{D.19})$$

Squaring both sides leads to

$$\frac{1}{\kappa^4 R^4} + \frac{2}{\kappa^2 R^2} - \frac{2v_s^2}{\kappa^2 R^2} = \frac{4v_s^2}{\kappa^2 R^2}. \quad (\text{D.20})$$

Rearranging the expression results in

$$3v_s^2 = 1 + \frac{1}{2\kappa^2 R^2}. \quad (\text{D.21})$$

D. Derivation of the Eckhaus Instability

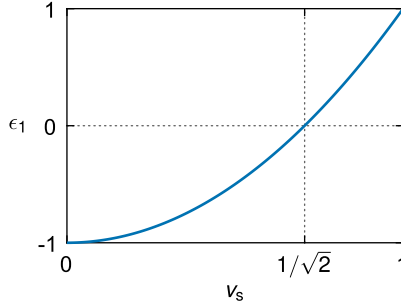


Figure D.1 | Eigenvalue ϵ_1 for a single phase slip as a function of the normalized superfluid velocity v_s for $R = \lambda = \xi$. For $\epsilon_1 < 0$, fluctuations of the order parameter decay to zero. In contrast, for $\epsilon_1 > 0$, fluctuations grow to nucleate a single phase-slip event. The instability point is at $\epsilon_1 = 0$.

Thus, the critical superfluid velocity takes the form

$$v_s^c = \frac{1}{\sqrt{3}} \sqrt{1 + \frac{1}{2\kappa^2 R^2}}, \quad (\text{D.22})$$

as shown in Figure D.1 for $R = 1$ and $\kappa = 1$. For $R = \infty$, the critical superfluid velocity reduces to that of an infinite one-dimensional superconductor, namely $v_s^c = 1/\sqrt{3}$. In terms of the magnetic flux, the instability criterion for a deterministic transition from the flux state $n = 0$ to $n = 1$ is expressed as

$$\phi_c = \frac{\kappa R}{\sqrt{3}} \sqrt{1 + \frac{1}{2\kappa^2 R^2}}. \quad (\text{D.23})$$

E

Derivation of the Saddle-State Energy

For a superconducting ring to transition between the local minima of the free energy, it must surmount a finite energy barrier. This barrier is characterized by the trajectory the ring traverses from one metastable minimum to the next, passing through a saddle point in the free-energy landscape, known as the saddle state. This appendix derives the energy of the saddle state and the free-energy barrier according to the Langer–Ambegaokar–McCumber–Halperin (hereafter LAMH) theory [62, 166–170].

E.1 Saddle states

As discussed in Chapter 5, the metastable states of a one-dimensional superconducting ring correspond to circular orbits of a particle with a radial coordinate f and time x , where f is the magnitude of the order parameter, and x is the spatial coordinate defined by $x \equiv R\theta$. To switch between two circular orbits, the particle temporarily occupies an elliptical orbit—that is, an orbit whose radial coordinate f is not constant. This elliptical orbit satisfies the stationarity condition

$$\frac{dE_s}{dx} = 0, \tag{E.1}$$

where E_s is the mechanical energy of the particle. Equivalently, the saddle state satisfies the time-independent Ginzburg-Landau equation. The elliptical

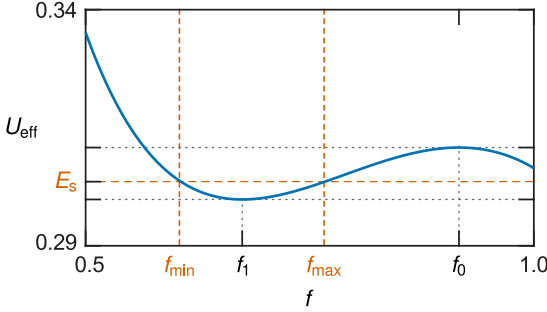


Figure E.1 | Saddle and metastable states. The effective potential U_{eff} , in the form (5.9), as a function of the magnitude f of the order parameter of a ring enclosing a magnetic flux $\phi = 2/5$. The metastable flux states are analogous to the circular orbits of a particle in an effective potential. The radii f_0 and f_1 represent circular orbits denoting the states $n = 0$ and $n = 1$, respectively. The saddle state is analogous to an elliptical orbit and is characterized by the two turning points f_{min} and f_{max} .

orbit is characterized by two turning points for which the mechanical energy of the particle equals the effective potential (5.9), as depicted in Figure E.1.

To derive an expression for the saddle state, we impose the stationarity condition (5.11), which leads to the differential equation

$$\sqrt{2}\kappa\sqrt{E_s - U_{\text{eff}}} = \frac{df}{dx}. \quad (\text{E.2})$$

Using separation of variables results in

$$x = \int_{f_{\text{min}}}^f \frac{df}{\sqrt{2}\kappa\sqrt{E_s - U_{\text{eff}}}}, \quad (\text{E.3})$$

where, owing to the cylindrical symmetry of the ring, the location of f_{min} can be set to any point in the ring (e.g., $x = 0$). Substituting with the effective potential (5.9) leads to

$$x = \frac{1}{\sqrt{2}\kappa} \int_b^u du \left(4E_s u - 2u^2 - 2J_s^2 + u^3 \right)^{-1/2}, \quad (\text{E.4})$$

where $u \equiv f^2$. Because the mechanical energy equals the effective potential at the turning points, the denominator equals zero. In terms of its poles, the

denominator reads

$$x = \frac{1}{\sqrt{2}\kappa} \int_b^u \frac{du}{\sqrt{(u-b)(u-a)(u-c)}}, \quad (\text{E.5})$$

where

$$b + a + c = 2, \quad (\text{E.6})$$

$$ba + bc + ac = 4E_s, \quad (\text{E.7})$$

and

$$bac = 2J_s^2. \quad (\text{E.8})$$

The integral (E.5) evaluates to

$$x = \frac{1}{\kappa} \sqrt{\frac{2}{c-b}} F(g, q), \quad (\text{E.9})$$

where $F(g, q)$ is the incomplete elliptic integral of the first kind with

$$g \equiv \arcsin \sqrt{\frac{u-b}{a-b}}, \quad (\text{E.10})$$

and

$$q \equiv \sqrt{\frac{a-b}{c-b}}. \quad (\text{E.11})$$

In terms of Jacobi functions, the elliptic integral (E.9) takes the form

$$u(x) = b + (a-b) \text{Sn}^2 \left(\kappa \sqrt{\frac{c-b}{2}} x, q \right). \quad (\text{E.12})$$

The magnitude $u(x)$ is determined by the three parameters b , a , and c . These three parameters are not independent and can be expressed in terms of the two parameters

$$v \equiv c - b, \quad (\text{E.13})$$

and

$$y \equiv \frac{a-b}{v}. \quad (\text{E.14})$$

Consequently, two additional equations are required to determine $u(x)$. First, since we assumed the lowest density in the ring, namely b , occurs at $x = 0$, the

E. Derivation of the Saddle-State Energy

density at the furthest point must be a ($u = a$ at $x = \pi R$). Substituting with v and y into equation (E.9) leads to

$$\begin{aligned}\pi R &= \frac{1}{\kappa} \sqrt{\frac{2}{v}} F(\pi/2, \sqrt{y}) \\ &= \frac{1}{\kappa} \sqrt{\frac{2}{v}} K(\sqrt{y}),\end{aligned}\tag{E.15}$$

where $K(\sqrt{y})$ is the complete elliptic integral of the first kind. Second, due to the single-valuedness of the order parameter, the phase accumulated along a closed cycle is an integer multiple of 2π . Using the supercurrent density (5.5), the accumulated phase takes the form

$$2\pi n = 2\pi R \kappa A + \int_0^{2\pi R} \frac{\kappa J_s}{u} dx.\tag{E.16}$$

Because the saddle state is stationary, the supercurrent density is uniform and can be taken out of the integral, leading to

$$2\pi n = 2\pi\phi + 2\kappa J_s \int_0^{\pi R} \frac{1}{u} dx.\tag{E.17}$$

The integral (E.17) evaluates to

$$2\pi n = 2\pi\phi + \frac{2J_s}{b} \sqrt{\frac{2}{v}} \Pi\left(-\frac{yv}{b}, \sqrt{y}\right),\tag{E.18}$$

where Π is the complete elliptic integral of the third kind.

If the ring's circumference is much longer than the coherence length ($L \gg \xi$), then $\sqrt{y} \approx 1$, and the elliptic integral in the condition (E.15) reduces to [190]

$$\lim_{\sqrt{y} \rightarrow 1} 2K(\sqrt{y}) = \ln \frac{16}{1 - \sqrt{y}}.\tag{E.19}$$

Therefore, the condition (E.15) takes the form

$$\sqrt{y} = 1 - 16 \exp\left(-\frac{L}{\xi} \sqrt{\frac{v}{2}}\right).\tag{E.20}$$

For $L \geq \xi$, $\sqrt{y} \approx 1$, and the approximation is consistent. Moreover, in that limit, the integral (E.17) reduces to the transcendental equation

$$2\pi n = 2\pi\phi + \frac{L}{\xi} \sqrt{\frac{1-v}{3}} + 2 \arctan \sqrt{\frac{3v}{2-2v}},\tag{E.21}$$

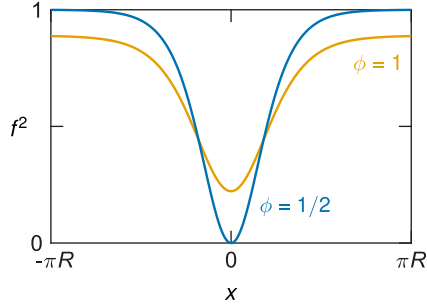


Figure E.2 | Saddle state. The magnitude of the complex order parameter of a saddle state along the circumference of a superconducting ring of radius $R = 2\xi$ and $\kappa = 1$. The flux ϕ is normalized by the flux quantum.

for the parameter ν as a function of the magnetic flux ϕ enclosed by the ring. The density of the saddle state (E.12), then, simplifies to

$$u = \frac{2-2\nu}{3} + \nu \tanh^2 \left(\sqrt{\frac{\nu}{2}} \kappa x \right), \quad (\text{E.22})$$

where the identity $\text{Sn}(z, 1) = \tanh z$ was used. For a flux bias $\phi = 1/2$, the parameter $\nu = 1$, and the density reads

$$u = \tanh^2 \left(\frac{\kappa x}{\sqrt{2}} \right). \quad (\text{E.23})$$

The further the flux bias from the degeneracy point $\phi = n + 1/2$, the lower the parameter ν . But, for the approximation (E.20) to hold, the exponent must be sufficiently large. Consequently, the expression (E.22) is only valid in the vicinity of the degeneracy point.

E.2 Free-energy barrier

In general, the free-energy density can be expressed as

$$\tilde{F} = \left| \left(i \frac{\nabla}{\kappa} + \mathbf{A} \right) \psi \right|^2 - |\psi|^2 + \frac{1}{2} |\psi|^4. \quad (\text{E.24})$$

Substituting with the polar form of the complex order parameter leads to the free-energy density

$$\tilde{F} = \frac{J_s^2}{f^2} + \left(\frac{f'}{\kappa} \right)^2 - f^2 + \frac{f^4}{2}. \quad (\text{E.25})$$

Casting the equation into the form

$$\tilde{F} = f \left(\frac{J_s^2}{f^3} + -f + f^3 \right) - \frac{f^4}{2} + \left(\frac{f'}{\kappa} \right)^2, \quad (\text{E.26})$$

and substituting with the stationarity condition (5.7) results in

$$\tilde{F} = \frac{f f''}{\kappa^2} - \frac{f^4}{2} + \left(\frac{f'}{\kappa} \right)^2. \quad (\text{E.27})$$

Integrating over the volume of the ring leads to the free energy

$$F = -\frac{wd}{2} \int f^4 dx + \frac{wd}{\kappa^2} \left[\int f f'' dx + \int f' f' dx \right], \quad (\text{E.28})$$

where w and d denote the width and the thickness of the ring, respectively. Integrating the last term by parts leads to

$$\begin{aligned} F &= -\frac{wd}{2} \int f^4 dx + \frac{wd}{\kappa^2} \left[\int f f'' dx - \int f f'' dx \right] \\ &= -\frac{wd}{2} \int f^4 dx. \end{aligned} \quad (\text{E.29})$$

Thus, the free energy of a stationary state in Joules can be written as

$$F = -\frac{F_C}{\pi R} \int_0^{\pi R} u^2 dx, \quad (\text{E.30})$$

where $u \equiv f^2$. The recipe to obtain the free energy of the saddle state is as follows. First, for each flux bias ϕ , the two conditions (E.15) and (E.18) are

solved self-consistency for ν and γ . Second, the magnitude of the saddle-state order parameter (E.12) is inserted into the free energy (E.30). In the limit $\sqrt{\gamma} \rightarrow 1$, the free energy of the saddle state reads

$$F_s = -F_C \left[\frac{(2 + \nu)^2}{9} - \frac{8}{3} \frac{\xi}{L} \sqrt{2\nu} \right]. \quad (\text{E.31})$$

The free-energy barrier is defined as

$$\Delta F = F_s - F_n, \quad (\text{E.32})$$

where F_n is the energy of the initial metastable flux state labeled by the phase winding number n .

Bibliography

1. Blundell, S. J. *Superconductivity: A Very Short Introduction* (Oxford University Press, 2009).
2. Dahl, P. F. *Superconductivity: Its Historical Roots and Development from Mercury to the Ceramic Oxides* (AIP-Press, 1992).
3. Onnes, H. K. Further experiments with liquid helium. *Comm. Leiden.*, 120b (1911).
4. Tinkham, M. *Introduction to Superconductivity* (Dover Publications, 2004).
5. Meissner, W. & Ochsenfeld, R. Ein neuer Effekt bei Eintritt der Supraleitfähigkeit. *Naturwissenschaften* **21**, 787 (1933).
6. London, F. & London, H. The electromagnetic equations of the superconductor. *Proc. R. Soc.* **149**, 71 (1935).
7. Bardeen, J., Cooper, L. N. & Schrieffer, J. R. Theory of superconductivity. *Phys. Rev.* **108**, 1175 (1957).
8. Bardeen, J., Cooper, L. N. & Schrieffer, J. R. Microscopic theory of superconductivity. *Phys. Rev.* **106**, 162 (1957).

Bibliography

9. Yntema, G. B. Superconducting winding for electromagnet. *Phys. Rev.* **98**, 1197 (1955).
10. Clarke, J. & Braginski, A. I. *The SQUID Handbook: Fundamentals and Technology of SQUIDs and SQUID Systems* (Wiley-VCH, 2004).
11. Likharev, K. K. & Semenov, V. K. RSFQ logic/memory family: a new Josephson-junction technology for sub-terahertz-clock-frequency digital systems. *IEEE Trans. Appl. Supercond.* **1**, 3 (1991).
12. Josephson, B. Possible new effects in superconductive tunnelling. *Phys. Lett.* **1**, 251 (1962).
13. Josephson, B. Supercurrents through barriers. *Adv. Phys.* **14**, 419 (1965).
14. Feynman, R., Leighton, R. & Sands, M. *The Feynman Lectures on Physics (Vol. 3)* (Basic Books, 2011).
15. Girvin, S. M. in *Quantum Machines: Measurement and Control of Engineered Quantum Systems* (Oxford University Press, 2014).
16. Martinis, J. M., Devoret, M. H. & Clarke, J. Energy-level quantization in the zero-voltage state of a current-biased Josephson junction. *Phys. Rev. Lett.* **55**, 1543 (1985).
17. Martinis, J. M., Devoret, M. H. & Clarke, J. Experimental tests for the quantum behavior of a macroscopic degree of freedom: the phase difference across a Josephson junction. *Phys. Rev. B* **35**, 4682 (1987).
18. Clarke, J. & Wilhelm, F. K. Superconducting quantum bits. *Nature* **453**, 1031 (2008).
19. Schoelkopf, R. J. & Girvin, S. M. Wiring up quantum systems. *Nature* **451**, 664 (2008).
20. Girvin, S. M., Devoret, M. H. & Schoelkopf, R. J. Circuit QED and engineering charge-based superconducting qubits. *Phys. Scr.* **T137**, 014012 (2009).

21. Devoret, M. H. & Schoelkopf, R. J. Superconducting circuits for quantum information: an outlook. *Science* **339**, 1169 (2013).
22. Wendin, G. Quantum information processing with superconducting circuits: a review. *Rep. Prog. Phys.* **80**, 106001 (2017).
23. Krantz, P. *et al.* A quantum engineer's guide to superconducting qubits. *Appl. Phys. Rev.* **6**, 021318 (2019).
24. Kjaergaard, M. *et al.* Superconducting qubits: current state of play. *Annu. Rev. Condens. Matter Phys.* **11**, 369 (2020).
25. Castellanos-Beltran, M. A., Irwin, K. D., Hilton, G. C., Vale, L. R. & Lehnert, K. W. Amplification and squeezing of quantum noise with a tunable Josephson metamaterial. *Nat. Phys.* **4**, 929 (2008).
26. Bergeal, N. *et al.* Phase-preserving amplification near the quantum limit with a Josephson ring modulator. *Nature* **465**, 64 (2010).
27. Bouchiat, V., Vion, D., Joyez, P., Esteve, D. & Devoret, M. H. Quantum coherence with a single Cooper pair. *Phys. Scr.* **T76**, 165 (1998).
28. Nakamura, Y., Pashkin, Y. A. & Tsai, J. S. Coherent control of macroscopic quantum states in a single-Cooper-pair box. *Nature* **398**, 786 (1999).
29. Martinis, J. M., Nam, S., Aumentado, J. & Urbina, C. Rabi oscillations in a large Josephson-junction qubit. *Phys. Rev. Lett.* **89**, 117901 (2002).
30. Mooij, J. E. *et al.* Josephson persistent-current qubit. *Science* **285**, 1036 (1999).
31. Chiorescu, I., Nakamura, Y., Harmans, C. J. P. M. & Mooij, J. E. Coherent quantum dynamics of a superconducting flux qubit. *Science* **299**, 1869 (2003).
32. Chiorescu, I. *et al.* Coherent dynamics of a flux qubit coupled to a harmonic oscillator. *Nature* **431**, 159 (2004).

Bibliography

33. You, J. Q., Hu, X., Ashhab, S. & Nori, F. Low-decoherence flux qubit. *Phys. Rev. B* **75**, 140515 (2007).
34. Steffen, M. *et al.* High-coherence hybrid superconducting qubit. *Phys. Rev. Lett.* **105**, 100502 (2010).
35. Yan, F. *et al.* The flux qubit revisited to enhance coherence and reproducibility. *Nat. Comm.* **7**, 12964 (2016).
36. Manucharyan, V. E., Koch, J., Glazman, L. I. & Devoret, M. H. Fluxonium: single Cooper-pair circuit free of charge offsets. *Science* **326**, 113 (2009).
37. Earnest, N. *et al.* Realization of a system with metastable states of a capacitively shunted fluxonium. *Phys. Rev. Lett.* **120**, 150504 (2018).
38. Vion, D. *et al.* Manipulating the quantum state of an electrical circuit. *Science* **296**, 886 (2002).
39. Barends, R. *et al.* Coherent Josephson qubit suitable for scalable quantum integrated circuits. *Phys. Rev. Lett.* **111**, 080502 (2013).
40. Barends, R. *et al.* Superconducting quantum circuits at the surface code threshold for fault tolerance. *Nature* **508**, 500 (2014).
41. Koch, J. *et al.* Charge-insensitive qubit design derived from the Cooper pair box. *Phys. Rev. A* **76**, 042319 (2007).
42. Houck, A. A. *et al.* Controlling the spontaneous emission of a superconducting transmon qubit. *Phys. Rev. Lett.* **101**, 080502 (2008).
43. Arute, F. *et al.* Quantum supremacy using a programmable superconducting processor. *Nature* **574**, 505 (2019).
44. Blais, A., Girvin, S. M. & Oliver, W. D. Quantum information processing and quantum optics with circuit quantum electrodynamics. *Nat. Phys.* **16**, 247 (2020).

45. Blais, A., Huang, R., Wallraff, A., Girvin, S. M. & Schoelkopf, R. J. Cavity quantum electrodynamics for superconducting electrical circuits: an architecture for quantum computation. *Phys. Rev. A* **69**, 062320 (2004).
46. Majer, J. *et al.* Coupling superconducting qubits via a cavity bus. *Nature* **449**, 443 (2007).
47. Blais, A. *et al.* Quantum-information processing with circuit quantum electrodynamics. *Phys. Rev. A* **75**, 032329 (2007).
48. Haroche, S., Brune, M. & Raimond, J. M. From cavity to circuit quantum electrodynamics. *Nat. Phys.* **16**, 243 (2020).
49. Yoshihara, F., Harrabi, K., Niskanen, A. O., Nakamura, Y. & Tsai, J. S. Decoherence of flux qubits due to $1/f$ flux noise. *Phys. Rev. Lett.* **97**, 167001 (2006).
50. Kakuyanagi, K. *et al.* Dephasing of a superconducting flux qubit. *Phys. Rev. Lett.* **98**, 047004 (2007).
51. Ambegaokar, V. & Baratoff, A. Tunneling between superconductors. *Phys. Rev. Lett.* **10**, 486 (1963).
52. Annett, J. F. *Superconductivity, Superfluids and Condensates* (Oxford University Press, 2004).
53. Veldhorst, M. *et al.* Josephson supercurrent through a topological insulator surface state. *Nat. Mat.* **11**, 417 (2012).
54. Wang, J. I. *et al.* Coherent control of a hybrid superconducting circuit made with graphene-based van der Waals heterostructures. *Nat. Nanotechnol.* **14**, 120 (2019).
55. Casparis, L. *et al.* Superconducting gatemon qubit based on a proximitized two-dimensional electron gas. *Nat. Nanotechnol.* **13**, 915 (2018).
56. Larsen, T. W. *et al.* Semiconductor-nanowire-based superconducting qubit. *Phys. Rev. Lett.* **115**, 127001 (2015).

Bibliography

57. Luthi, F. *et al.* Evolution of nanowire transmon qubits and their coherence in a magnetic field. *Phys. Rev. Lett.* **120**, 100502 (2018).
58. Mermin, N. D. & Wagner, H. Absence of ferromagnetism or antiferromagnetism in one- or two-dimensional isotropic Heisenberg models. *Phys. Rev. Lett.* **17**, 1133 (1966).
59. Lukens, J. E., Warburton, R. J. & Webb, W. W. Onset of quantized thermal fluctuations in one-dimensional superconductors. *Phys. Rev. Lett.* **25**, 1180 (1970).
60. Newbower, R. S., Beasley, M. R. & Tinkham, M. Fluctuation effects on the superconducting transition of tin whisker crystals. *Phys. Rev. B* **5**, 864 (1972).
61. Skocpol, W. J. & Tinkham, M. Fluctuations near superconducting phase transitions. *Rept. Prog. Phys.* **38**, 1049 (1975).
62. Langer, J. S. & Ambegaokar, V. Intrinsic resistive transition in narrow superconducting channels. *Phys. Rev.* **164**, 498 (1967).
63. McCumber, D. E. & Halperin, B. I. Time scale of intrinsic resistive fluctuations in thin superconducting wires. *Phys. Rev. B* **1**, 1054 (1970).
64. Arutyunov, K., Golubev, D. & Zaikin, A. Superconductivity in one dimension. *Phys. Rep.* **464**, 1 (2008).
65. Little, W. A. Decay of persistent currents in small superconductors. *Phys. Rev.* **156**, 396 (1967).
66. Bezryadin, A., Lau, C. N. & Tinkham, M. Quantum suppression of superconductivity in ultrathin nanowires. *Nature* **404**, 971 (2000).
67. Romijn, J. *Metallic structures with reduced dimensions*. PhD thesis (Delft University of Technology, 1991).

-
68. Lau, C. N., Markovic, N., Bockrath, M., Bezryadin, A. & Tinkham, M. Quantum phase slips in superconducting nanowires. *Phys. Rev. Lett.* **87**, 217003 (2001).
 69. Matveev, K. A., Larkin, A. I. & Glazman, L. I. Persistent current in superconducting nanorings. *Phys. Rev. Lett.* **89**, 096802 (2002).
 70. Li, P. *et al.* Switching currents limited by single phase slips in one-dimensional superconducting Al nanowires. *Phys. Rev. Lett.* **107**, 137004 (2011).
 71. Hriscu, A. M. & Nazarov, Y. V. Coulomb blockade due to quantum phase slips illustrated with devices. *Phys. Rev. B* **83**, 174511 (2011).
 72. Vanevic, M. & Nazarov, Y. V. Quantum phase slips in superconducting wires with weak inhomogeneities. *Phys. Rev. Lett.* **108**, 187002 (2012).
 73. Belkin, A., Belkin, M., Vakaryuk, V., Khlebnikov, S. & Bezryadin, A. Formation of quantum phase slip pairs in superconducting nanowires. *Phys. Rev. X* **5**, 021023 (2015).
 74. Saito, S. & Murayama, Y. Effect of dissipation on macroscopic quantum tunneling in thin superconducting wires. *Phys. Lett. A* **139**, 85 (1989).
 75. Giordano, N. Dissipation in a one-dimensional superconductor: evidence for macroscopic quantum tunneling. *Phys. Rev. B* **41**, 6350 (1990).
 76. Giordano, N. Superconducting fluctuations in one dimension. *Physica B* **203**, 460 (1994).
 77. Zaikin, A. D., Golubev, D. S., van Otterlo, A. & Zimányi, G. T. Quantum phase slips and transport in ultrathin superconducting wires. *Phys. Rev. Lett.* **78**, 1552 (1997).
 78. Golubev, D. S. & Zaikin, A. D. Quantum tunneling of the order parameter in superconducting nanowires. *Phys. Rev. B* **64**, 014504 (2001).

Bibliography

79. Altomare, F., Chang, A. M., Melloch, M. R., Hong, Y. & Tu, C. W. Evidence for macroscopic quantum tunneling of phase slips in long one-dimensional superconducting Al wires. *Phys. Rev. Lett.* **97**, 017001 (2006).
80. Baumans, X. D. A. *et al.* Thermal and quantum depletion of superconductivity in narrow junctions created by controlled electromigration. *Nat. Commun.* **7**, 10560 (2016).
81. Mooij, J. E. & Harmans, C. J. P. M. Phase-slip flux qubits. *New J. Phys.* **7**, 219 (2005).
82. Mooij, J. E. & Nazarov, Y. V. Superconducting nanowires as quantum phase-slip junctions. *Nat. Phys.* **2**, 169 (2006).
83. Chow, J. M. *et al.* Optimized driving of superconducting artificial atoms for improved single-qubit gates. *Phys. Rev. A* **82**, 040305 (2010).
84. Astafiev, O. V. *et al.* Coherent quantum phase slip. *Nature* **484**, 355 (2012).
85. Peltonen, J. T. *et al.* Coherent flux tunneling through NbN nanowires. *Phys. Rev. B* **88**, 220506 (2013).
86. Peltonen, J. T. *et al.* Coherent dynamics and decoherence in a superconducting weak link. *Phys. Rev. B* **94**, 180508 (2016).
87. De Graaf, S. E., Shaikhaidarov, R., Lindström, T., Tzalenchuk, A. Y. & Astafiev, O. V. Charge control of blockade of Cooper pair tunneling in highly disordered TiN nanowires in an inductive environment. *Phys. Rev. B* **99**, 205115 (2019).
88. Peltonen, J. T. *et al.* Hybrid rf SQUID qubit based on high kinetic inductance. *Sci. Rep.* **8**, 10033 (2018).
89. Hu, Z., Tie-Fu, L., Jian-She, L. & Wei, C. Charge-related SQUID and tunable phase-slip flux qubit. *Chin. Phys. Lett.* **31**, 030303 (2014).

-
90. De Graaf, S. E. *et al.* Charge quantum interference device. *Nat. Phys.* **14**, 590 (2018).
 91. Hongisto, T. T. & Zorin, A. B. Single-charge transistor based on the charge-phase duality of a superconducting nanowire circuit. *Phys. Rev. Lett.* **108**, 097001 (2012).
 92. Kafanov, S. & Chtchelkatchev, N. M. Single flux transistor: the controllable interplay of coherent quantum phase slip and flux quantization. *J. Appl. Phys.* **114**, 073907 (2013).
 93. Cheng, R., Goteti, U. S. & Hamilton, M. C. Superconducting neuromorphic computing using quantum phase-slip junctions. *IEEE Trans. Appl. Supercond.* **29**, 1 (2019).
 94. Landau, L. D. On the theory of phase transitions (I). *Phys. Z. Sowjet.* **11**, 26 (1937).
 95. Landau, L. D. On the theory of phase transitions (II). *Phys. Z. Sowjet.* **11**, 545 (1937).
 96. Spaldin, N. A. *Magnetic Materials: Fundamentals and Applications* (Cambridge University Press, 2010).
 97. Landau, L. D. & Ginzburg, V. L. On the theory of superconductivity. *Zh. Eksp. Teor. Fiz.* **20**, 1064 (1950).
 98. Gor'kov, L. P. Microscopic derivation of the Ginzburg-Landau equations in the theory of superconductivity. *Sov. Phys. JETP* **9**, 1364 (1959).
 99. Bennett, D. A. *et al.* Decoherence in rf-SQUID qubits. *Quantum Inf. Process.* **8**, 217 (2009).
 100. Abrikosov, A. A. On the magnetic properties of superconductors of the second group. *Sov. Phys. JETP* **5**, 1174 (1957).

Bibliography

101. Stenuit, G, Michotte, S, Govaerts, J & Piraux, L. Temperature dependence of penetration and coherence lengths in lead nanowires. *Supercond. Sci. Technol.* **18**, 174 (2004).
102. Lombardo, J. *et al.* In situ tailoring of superconducting junctions via electro-annealing. *Nanoscale* **10**, 1987 (2018).
103. Doll, R. & Näbauer, M. Experimental proof of magnetic flux quantization in a superconducting ring. *Phys. Rev. Lett.* **7**, 51 (1961).
104. Deaver, B. S. & Fairbank, W. M. Experimental evidence for quantized flux in superconducting cylinders. *Phys. Rev. Lett.* **7**, 43 (1961).
105. Larkin, A. & Varlamov, A. *Theory of Fluctuations in Superconductors* (Clarendon Press, 2005).
106. Wu, M. K. *et al.* Superconductivity at 93 K in a new mixed-phase Y-Ba-Cu-O compound system at ambient pressure. *Phys. Rev. Lett.* **58**, 908 (1987).
107. Bednorz, J. G. & Müller, K. A. Possible high T_c superconductivity in the Ba-La-Cu-O system. *Z. Phys. B. Condens. Matter* **64**, 189 (1986).
108. Schmid, A. A time dependent Ginzburg-Landau equation and its application to the problem of resistivity in the mixed state. *Phys. Mat. Cond.* **5**, 302 (1966).
109. Gor'kov, L. P. & Éliashberg, G. M. Generalization of Ginzburg-Landau equations for non-stationary problems in the case of alloys with paramagnetic impurities. *Sov. Phys. JETP* **27**, 338 (1968).
110. Kramer, L. & Watts-Tobin, R. J. Theory of dissipative current-carrying states in superconducting filaments. *Phys. Rev. Lett.* **40**, 1041 (1978).
111. Watts-Tobin, R. J., Krähenbühl, Y. & Kramer, L. Nonequilibrium theory of dirty, current-carrying superconductors: phase-slip oscillators in narrow filaments near T_c . *J. Low Temp. Phys.* **42**, 459 (1981).

-
112. Aranson, I. S. & Kramer, L. The world of the complex Ginzburg-Landau equation. *Rev. Mod. Phys.* **74**, 99 (2002).
 113. Dobrovolskiy, O. V. *et al.* Moving flux quanta cool superconductors by a microwave breath. *Commun. Phys.* **3**, 64 (2020).
 114. Oripov, B. & Anlage, S. M. Time-dependent Ginzburg-Landau treatment of rf magnetic vortices in superconductors: vortex semiloops in a spatially nonuniform magnetic field. *Phys. Rev. E* **101**, 033306 (2020).
 115. Gropp, W. D. *et al.* Numerical simulation of vortex dynamics in type-II superconductors. *J. Comput. Phys.* **123**, 254 (1996).
 116. Vodolazov, D. Y. & Peeters, F. M. Dynamic transitions between metastable states in a superconducting ring. *Phys. Rev. B* **66**, 054537 (2002).
 117. Vodolazov, D. Y., Peeters, F. M., Dubonos, S. V. & Geim, A. K. Multiple flux jumps and irreversible behavior of thin Al superconducting rings. *Phys. Rev. B* **67**, 054506 (2003).
 118. Lu-Dac, M. & Kabanov, V. V. Multiple phase slips phenomena in mesoscopic superconducting rings. *Phys. Rev. B* **79**, 184521 (2009).
 119. Lu-Dac, M. & Kabanov, V. V. Phase slip phenomena in superconductors: from ordered to chaotic dynamics. *Phys. Rev. Lett.* **105**, 157005 (2010).
 120. Alstrøm, T. S., Sørensen, M. P., Pedersen, N. F. & Madsen, S. Magnetic flux lines in complex geometry type-II superconductors studied by the time dependent Ginzburg-Landau equation. *Acta Appl. Math.* **115**, 63 (2011).
 121. Grimaldi, G. *et al.* Speed limit to the Abrikosov lattice in mesoscopic superconductors. *Phys. Rev. B* **92**, 024513 (2015).
 122. Kwok, W. *et al.* Vortices in high-performance high-temperature superconductors. *Rep. Prog. Phys.* **79**, 116501 (2016).

Bibliography

123. Koshelev, A. E., Sadovskyy, I. A., Phillips, C. L. & Glatz, A. Optimization of vortex pinning by nanoparticles using simulations of the time-dependent Ginzburg-Landau model. *Phys. Rev. B* **93**, 060508 (2016).
124. Cyrot, M. Ginzburg-Landau theory for superconductors. *Rep. Prog. Phys.* **36**, 103 (1973).
125. Milošević, M. & Geurts, R. The Ginzburg–Landau theory in application. *Physica C* **470**, 791 (2010).
126. Silhanek, A. V. *et al.* Formation of stripelike flux patterns obtained by freezing kinematic vortices in a superconducting Pb film. *Phys. Rev. Lett.* **104**, 017001 (2010).
127. Adami, O. *et al.* Onset, evolution, and magnetic braking of vortex lattice instabilities in nanostructured superconducting films. *Phys. Rev. B* **92**, 134506 (2015).
128. Schmidt, V. V. *The Physics of Superconductors: Introduction to Fundamentals and Applications* (Springer, 1997).
129. Michotte, S., Mátéfi-Tempfli, S., Piraux, L., Vodolazov, D. Y. & Peeters, F. M. Condition for the occurrence of phase slip centers in superconducting nanowires under applied current or voltage. *Phys. Rev. B* **69**, 094512 (2004).
130. Vodolazov, D. Y., Peeters, F. M., Piraux, L., Mátéfi-Tempfli, S. & Michotte, S. Current-Voltage Characteristics of Quasi-One-Dimensional Superconductors: An S-Shaped Curve in the Constant Voltage Regime. *Phys. Rev. Lett.* **91**, 157001 (2003).
131. Malomed, B. A. & Weber, A. Dynamics of a superconductive filament in the constant-voltage regime. *Phys. Rev. B* **44**, 875 (2 1991).
132. Tuckerman, L. S. & Barkley, D. Bifurcation analysis of the Eckhaus instability. *Physica D* **46**, 57 (1990).

133. Tarlie, M. B. & Elder, K. R. Metastable state selection in one-dimensional systems with a time-ramped control parameter. *Phys. Rev. Lett.* **81**, 18 (1998).
134. Karttunen, M., Elder, K. R., Tarlie, M. B. & Grant, M. Instabilities and resistance fluctuations in thin accelerated superconducting rings. *Phys. Rev. E* **66**, 026115 (2002).
135. Kogan, V. G., Clem, J. R. & Mints, R. G. Properties of mesoscopic superconducting thin-film rings: London approach. *Phys. Rev. B* **69**, 064516 (2004).
136. Kerner, C. *et al.* Control and readout of current-induced magnetic flux quantization in a superconducting transformer. *Supercond. Sci. Technol.* **22**, 025001 (2009).
137. Polonsky, S. V., Kirichenko, A. F., Semenov, V. K. & Likharev, K. K. Rapid single flux quantum random access memory. *IEEE Trans. Appl. Supercond.* **5**, 3000 (1995).
138. Nagasawa, S., Numata, H., Hashimoto, Y. & Tahara, S. High-frequency clock operation of Josephson 256-word/spl times/16-bit RAMs. *IEEE Trans. Appl. Supercond.* **9**, 3708 (1999).
139. Kirichenko, A. F., Sarwana, S., Brock, D. K. & Radpavar, M. Pipelined DC-powered SFQ RAM. *IEEE Trans. Appl. Supercond.* **11**, 537 (2001).
140. Bunyk, P., Likharev, K. & Zinoviev, D. RSFQ technology: physics and devices. *Int. J. High Speed Electron. Syst.* **11**, 257 (2001).
141. Tolpygo, S. K. Superconductor digital electronics: scalability and energy efficiency issues. *Low Temp. Phys.* **42**, 361 (2016).
142. Chen, L. *et al.* Miniaturization of the superconducting memory cell via a three-dimensional Nb nano-superconducting quantum interference device. *ACS Nano* **14**, 11002 (2020).

Bibliography

143. Liu, E. *et al.* Top-pinned STT-MRAM devices with high thermal stability hybrid free layers for high-density memory applications. *IEEE Trans. Magn.* **54**, 1 (2018).
144. Ling, X. S. *et al.* Superheating and supercooling of vortex matter in a Nb single crystal: direct evidence for a phase transition at the peak effect from neutron diffraction. *Phys. Rev. Lett.* **86**, 712 (2001).
145. Deang, J., Du, Q. & Gunzburger, M. D. Modeling and computation of random thermal fluctuations and material defects in the Ginzburg–Landau model for superconductivity. *J. Comput. Phys.* **181**, 45 (2002).
146. Ge, J. *et al.* Nanoscale assembly of superconducting vortices with scanning tunnelling microscope tip. *Nat. Comm.* **7**, 13880 (2016).
147. Veshchunov, I. S. *et al.* Optical manipulation of single flux quanta. *Nat. Comm.* **7**, 12801 (2016).
148. Shklovskij, V. A., Nazipova, A. P. & Dobrovolskiy, O. V. Pinning effects on self-heating and flux-flow instability in superconducting films near T_c . *Phys. Rev. B* **95**, 184517 (2017).
149. Duarte, E., Sardella, E., Ortiz, W. & Zadorosny, R. Dynamics and heat diffusion of Abrikosov’s vortex-antivortex pairs during an annihilation process. *J. Phys. Condens. Matter* **29**, 405605 (2017).
150. Duarte, E. *et al.* Use of thermal gradients for control of vortex matter in mesoscopic superconductors. *J. Phys. Condens. Matter* **31** (2019).
151. Doron, A., Levinson, T., Gorniaczyk, F., Tamir, I. & Shahar, D. The critical current of disordered superconductors near 0 K. *Nat. Comm.* **11**, 2667 (2020).
152. Adam, S., Piraux, L., Michotte, S., D., L. & Mailly, D. Discontinuous hotspot growth related to the thermal healing length in superconducting NbN microstrips. *J. Phys. Conf. Ser.* **234**, 022001 (2010).

153. Zotova, A. N. & Vodolazov, D. Y. Photon detection by current-carrying superconducting film: a time-dependent Ginzburg-Landau approach. *Phys. Rev. B* **85**, 024509 (2012).
154. Zotova, A. & Vodolazov, D. Intrinsic detection efficiency of superconducting nanowire single photon detector in the modified hot spot model. *Supercond. Sci. Technol.* **27**, 125001 (2014).
155. Zhang, L. *et al.* Hotspot relaxation time of NbN superconducting nanowire single-photon detectors on various substrates. *Sci. Rep.* **8**, 1486 (2018).
156. Gurevich, A. V. & Mints, R. G. Self-heating in normal metals and superconductors. *Rev. Mod. Phys.* **59**, 941 (1987).
157. Vodolazov, D. Y., Peeters, F. M., Morelle, M. & Moshchalkov, V. V. Masking effect of heat dissipation on the current-voltage characteristics of a mesoscopic superconducting sample with leads. *Phys. Rev. B* **71**, 184502 (2005).
158. Jelić, Ž. L., Milošević, M. V. & Silhanek, A. V. Velocimetry of superconducting vortices based on stroboscopic resonances. *Sci. Rep.* **6**, 35687 (2016).
159. Dobrovolskiy, O. V. *et al.* Ultra-fast vortex motion in a direct-write Nb-C superconductor. *Nat. Comm.* **11**, 3291 (2020).
160. Romijn, J., Klapwijk, T. M., Renne, M. J. & Mooij, J. E. Critical pair-breaking current in superconducting aluminum strips far below T_c . *Phys. Rev. B* **26**, 3648 (1982).
161. Soloviev, I. I. *et al.* Beyond Moore's technologies: operation principles of a superconductor alternative. *Beilstein J. Nanotechnol.* **8**, 2689 (2017).
162. Petkovic, I., Lollo, A., Glazman, L. I. & Harris, J. G. E. Deterministic phase slips in mesoscopic superconducting rings. *Nat. Commun.* **7**, 13551 (2016).

Bibliography

163. Giordano, N. Evidence for macroscopic quantum tunneling in one-dimensional superconductors. *Phys. Rev. Lett.* **61**, 2137 (1988).
164. Arutyunov, K. Y., Hongisto, T. T., Lehtinen, J. S., Leino, L. I. & Vasiliev, A. L. Quantum phase slip phenomenon in ultra-narrow superconducting nanorings. *Sci. Rep.* **2**, 293 (2012).
165. Petkovic, I., Lollo, A. & Harris, J. G. E. Phase-slip statistics of a single isolated flux-biased superconducting ring. *Phys. Rev. Lett.* **125**, 067002 (2020).
166. Tarlie, M. B., Shimshoni, E. & Goldbart, P. M. Intrinsic dissipative fluctuation rate in mesoscopic superconducting rings. *Phys. Rev. B* **49**, 494 (1994).
167. Zhang, X. & Price, J. C. Susceptibility of a mesoscopic superconducting ring. *Phys. Rev. B* **55**, 3128 (1997).
168. Qiu, C., Qian, T. & Ren, W. Phase slips in superconducting wires with nonuniform cross section: a numerical evaluation using the string method. *Phys. Rev. B* **77**, 104516 (2008).
169. Bert, J. A., Koshnick, N. C., Bluhm, H. & Moler, K. A. Fluxoid fluctuations in mesoscopic superconducting rings. *Phys. Rev. B* **84**, 134523 (2011).
170. Polshyn, H., Naibert, T. R. & Budakian, R. Imaging phase slip dynamics in micron-size superconducting rings. *Phys. Rev. B* **97**, 184501 (2018).
171. Schweigert, V. A. & Peeters, F. M. Flux penetration and expulsion in thin superconducting disks. *Phys. Rev. Lett.* **83**, 2409 (1999).
172. Baelus, B. J., Peeters, F. M. & Schweigert, V. A. Saddle-point states and energy barriers for vortex entrance and exit in superconducting disks and rings. *Phys. Rev. B* **63**, 144517 (2001).
173. Qian, T., Ren, W. & Sheng, P. Current dissipation in thin superconducting wires: a numerical evaluation using the string method. *Phys. Rev. B* **72**, 014512 (2005).

174. De Simoni, G., Paolucci, F., Solinas, P., Strambini, E. & Giazotto, F. Metallic supercurrent field-effect transistor. *Nat. Nanotechnol.* **13**, 802 (2018).
175. Paolucci, F. *et al.* Magnetotransport experiments on fully metallic superconducting Dayem-bridge field-effect transistors. *Phys. Rev. Applied* **11**, 024061 (2019).
176. Sendelbach, S. *et al.* Magnetism in SQUIDs at millikelvin temperatures. *Phys. Rev. Lett.* **100**, 227006 (2008).
177. Drung, D., Beyer, J., Storm, J., Peters, M. & Schurig, T. Investigation of low-frequency excess flux noise in dc SQUIDs at mK temperatures. *IEEE Trans. Appl. Supercond.* **21**, 340 (2011).
178. Wellstood, F. C., Urbina, C. & Clarke, J. Low-frequency noise in dc superconducting quantum interference devices below 1 K. *Appl. Phys. Lett.* **50**, 772 (1987).
179. Wang, H. *et al.* Candidate source of flux noise in SQUIDs: adsorbed oxygen molecules. *Phys. Rev. Lett.* **115**, 077002 (2015).
180. Anton, S. M. *et al.* Pure dephasing in flux qubits due to flux noise with spectral density scaling as $1/f^\alpha$. *Phys. Rev. B* **85**, 224505 (2012).
181. Koch, R. H., DiVincenzo, D. P. & Clarke, J. Model for $1/f$ flux noise in SQUIDs and qubits. *Phys. Rev. Lett.* **98**, 267003 (2007).
182. Faoro, L. & Ioffe, L. B. Microscopic origin of low-frequency flux noise in Josephson circuits. *Phys. Rev. Lett.* **100**, 227005 (2008).
183. Choi, S., Lee, D.-H., L., S. G. & Clarke, J. Localization of metal-induced gap states at the metal-insulator interface: origin of flux noise in SQUIDs and superconducting qubits. *Phys. Rev. Lett.* **103**, 197001 (2009).
184. Friedman, J. R., Patel, V., Chen, W., Tolpygo, S. K. & Lukens, J. E. Quantum superposition of distinct macroscopic states. *Nature* **406**, 43 (2000).

Bibliography

185. Clarke, J. *et al.* Quiet readout of superconducting flux states. *Phys. Scr.* **T102**, 173 (2002).
186. Van der Wal, C. H. *et al.* Quantum superposition of macroscopic persistent-current states. *Science* **290**, 773 (2000).
187. Griffiths, D. J. *Introduction to Electrodynamics* (Cambridge University Press, 2017).
188. Aharonov, Y. & Bohm, D. Significance of electromagnetic potentials in the quantum theory. *Phys. Rev.* **115**, 485 (1959).
189. Riley, K., Hobson, M. & Bence, S. *Mathematical Methods for Physics and Engineering* (Cambridge University Press, 2009).
190. Abramowitz, M. & Stegun, I. *Handbook of Mathematical Functions: with Formulas, Graphs, and Mathematical Tables* (Dover Publications, 1965).
191. Thomas, J. *Numerical Partial Differential Equations: Finite Difference Methods* (Springer New York, 1998).

List of Publications

- **Kenawy, A.** et al. Electronically tunable quantum phase slips in voltage-biased superconducting rings as a base for phase-slip flux qubits. *Supercond. Sci. Technol.* **33**, 125002 (2020).
- **Kenawy, A.** et al. Voltage-controlled coupling of flux states in superconducting rings. *Supercond. Sci. Technol.* **33**, 025002 (2019).
- **Kenawy, A.** et al. Voltage-controlled superconducting magnetic memory. *AIP Adv.* **9**, 125223 (2019).
- **Kenawy, A.** et al. Vibration-induced modulation of magnetic anisotropy in a magnetic molecule. *Phys. Rev. B* **97**, 235441 (2018).
- **Kenawy, A.** et al. Flux quantization and Aharonov-Bohm effect in superconducting rings. *J. Supercond. Nov. Magn.* **31**, 1351 (2017).
- **Kenawy, A.** et al. Tunnel magnetoresistance of magnetic molecules with spin-vibron coupling. *AIP Adv.* **7**, 055708 (2017).

List of Conferences

- 2021 **American Physical Society March Meeting, USA**
Talk: *Electronically-tunable quantum phase slips in voltage-biased superconducting rings*
- 2020 **American Physical Society March Meeting, USA**
Talk: *Electrically-tunable phase-slip qubits (cancelled)*
- 2019 **Annual Conference on Magnetism and Magnetic Materials, USA**
Talk: *Voltage-controlled superconducting magnetic memory*
- 2019 **American Physical Society March Meeting, USA**
Talk: *Phase slips in voltage-biased superconducting rings*
- 2019 **Vortex Conference, Belgium**
Poster: *Phase slips in voltage-biased superconducting rings*

FACULTY OF SCIENCE
DEPARTMENT OF PHYSICS AND ASTRONOMY
INSTITUTE FOR THEORETICAL PHYSICS
Celestijnenlaan 200D
B-3001 Leuven

